POSITRON ANNIHILATION IN NORMAL HYDROCARBONS AND IN SOLID MAGNETIC MATERIALS

A Thesis

Submitted to the

Faculty of Graduate Studies

University of Manitoba

in partial fulfillment of the

requirements of the degree of

Doctor of Philosophy

by

Shu-yuan Chuang

Winnipeg, Canada

March, 1968

To My Parents

TABLE OF CONTENTS

LIST OF FIGURES

ACKNOWLEDGEMENTS

The author wishes to express his sincere thanks to Prof. B. G. Hogg for his valuable advice and for his patient guidance and constant encouragement throughout this research.

Thanks are also due Dr. W. H. Holt for his valuable advice and assistance during the performance of the low temperature experiments and to Mr. A. M. Cooper for his assistance with the electronics and for many helpful discussions. Thanks are also due Dr. D. P. Kerr for his valuable guidance in the beginning of this research.

The author is also indebted to Prof. A. H. Morrish for arranging with Dr. J. W. Nielson of Airtron Company for the growing of the $(La_{.7}Pb_{.3})MnO_3$ crystals.

The finacial support of the National Research Council of Canada and the American Chemical Society Petroleum Research Fund is greatfully acknowledged.

ABSTRACT

The Angular correlation of the two-photon annihilation of positrons in a number of condensed hydrocarbons and two solid magnetic materials have been studied using a standard parallel-slit apparatus.

Three different theoretical approaches have been employed to obtain the momentum distributions in the hydrocarbons. The first approach is to assume that the positron wave function is constant. The momentum distributions are then calculated for electrons in the C-C and C-H bonds, using analytic SCF functions for atomic carbon orbitals and Heitler-London-type functions for the two paired electrons in the C-C and C-H bonds. The calculated results of this low momentum plane wave approach for the positron fits well with the experimental data except at the tail of the distributions. The second approach is to assume that the positron wave function is of the form $\psi_+(r) = 1 - e^{-m_i r}$ where m_i is a parameter corresponding to the i^{th} atom. In the third method, $\psi_+(r)$ is obtained by numerical integration from the ground state radial Schrödinger equation. The results obtained from the last two methods are in good agreement with the experimental data. This suggests that the effect of the positron wave function can not be ignored in the detailed analysis of the observed momentum distribution in the hydrocarbons.

The interpretation of the angular distribution for Alnico is based on the contributions from the 4s and 3d bands of this alloy.

A study of angular distribution obtained with the perovskite crystals $(La_{.7}Pb_{.3})MnO_3$ suggests that the positrons annihilate exclusively with the 2s and 2p electrons of the negative oxygen ions.

Chapter 1

Introduction

1.1 The Discovery of The Positron

The positron was first discovered by C. D. Anderson in his experiments on particles produced by cosmic rays.[1] Anderson while taking Wilson cloud-chamber photographs of cosmic ray trajectories when a magnetic field was applied across the chamber, found pairs of tracks with the same ionization density. Each track described a separate circle in the magnetic field such that one path could be ascribed to an electron and the other to a particle of electronic mass but of positive electronic charge. Anderson called these particles "positrons". Before the discovery of positrons, Dirac had predicted the existence of positrons (actually he originally theorized that these were positive protons) in his "hole theory".[2] According to the Dirac theory, the energy of the electron has both positive and negative energy solutions, i.e., $E=\pm\sqrt{p^2c^2+m^2c^4}$. It was assumed that all negative energy states ($-mc^2$ to $-\infty$) are normally occupied by electrons. A positron appears as "hole" in these states when an electron makes a transition to a positive energy level.

About a year after the discovery of the positrons by Anderson, sources of positrons became plentiful and easily obtainable as a result of the discovery by the Curie-Joliots of the phenomenon of artificial or induced radioactivity.

1.2 The Annihilation of Slow Positrons

It is well known that the positron is the anti-particle of the electron, and that these two particles can be annihilated as a pair with the emission of gamma photons. It has been shown[3] that the probability of a positron annihilating in flight is less than 2% for initial positron energies of $\sim \frac{1}{2}$ Mev. Therefore we shall discuss here only the annihilation of slow positrons.

When a positron enters a condensed medium, it may annihilate directly with an electron (so called "direct annihilation") or it may capture an electron to form positronium. Some evidence for the formation of positron compounds as well as positronium compounds has also been found.[17]

By the principle of conservation of momentum, at least two photons must be involved in the annihilation process of a slow positron-electron pair. Annihilation by single photon emission requires the presence of an external field. The probability for one-photon and three or more photon annihilation is very small compared with that for two-photon annihilation. Ore and Powell[4] have shown that the ratio of the three- to two-photon annihilation cross section is 1/372.

Now consider the S-state positron-electron pair which can exist in one of two substates, namely, the singlet state, $^1S_0$, with spin zero, or the triplet state, $^3S_1$, with spin one. The higher orbital angular momentum states are not of interest since in these states the positron and electron wave functions

do no overlap sufficiently for appreciable annihilation to occur.

According to Yang,[6] the annihilation of a positron-electron pair into two photons is only possible for an annihilating pair in its singlet state. For it is well known that the relative intrinsic parity is negative for the positron-electron pair, i.e., $P_I = (-1)$. The charge conjugation for the S-state positron-electron system is therefore $P_C = P_I P_S = (-1)(-1)^{S+1} = (-1)^S$, where P_S is the spin parity. The charge conjugation is positive for the singlet state $(S = 0)$, and negative for the triplet state $(S = 1)$. Since the charge conjugation of the photon is assigned to be negative, the singlet state should annihilate into an even number of photons, and the triplet state into an odd number of photons, by means of charge conjugation invariance.

Recently, Berko et al[5] have designed an experiment to search for charge nonconservation in positron-electron annihilation by measuring the three-photon decay of the singlet state $(^1S_0)$. Their ratio of $(^1S_0 \rightarrow 3\gamma)/(^1S_0 \rightarrow 2\gamma)$ is less than 10^{-6}.

1.3 The Formation and the Basic Properties of Positronium

The possible existence of a bound state between a positron and an electron was first postulated by Mohorovicic in 1934.[7] Ruark gave this bound system the name "positronium".[8]

The first experimental demonstration of the existence of positronium was performed by Deutsch.[9,10]

To first order, positronium can be treated as a hydrogen atom, with the exception that the reduced mass is now one half the electron mass. One thus obtains a "Bohr radius" of a positronium atom $a_p = \hbar^2/\mu e^2 = 2\hbar^2/me^2 = 2a_o = 1.06\text{Å}$, with a ground state energy $E = e^2/2a_p = e^2/4a_o = 6.77\text{ev}$.

There are two ground states of positronium: the triplet state (ortho-positronium) with electron-positron spins parallel, and the singlet state (para-positronium) with electron-positron spins anti-parallel. Since the triplet state has three substates ($m = 1,0,-1$) the statistical weight of the triplet state is three times that of the singlet state, i.e., ortho-positronium and para-positronium atoms are formed in 3/4 and 1/4 of the cases respectively. According to the same argument in the last section, ortho-positronium undergoes 3-photon annihilation, and para-positronium decays via 2-photon emission.

The life times of para- and ortho-positronium have been calculated as 1.25×10^{-10} seconds and 1.4×10^{-7} seconds respectively.[4]

Ore postulated[11] the following approximate relationship for the probability (W) of positronium formation:

$$\frac{V_1-(V_i-V_p)}{V_1} \leqslant W \leqslant \frac{V_p}{V_i},$$

where V_1 is the first excitation energy of the surrounding molecules, V_i is the ionization energy of the molecules, and V_p is the binding energy of positronium ($\simeq 6.77$ ev in free space; it may be slightly less in a solid).

The above equation can be understood as follows. If the initial energy of the positron is E, positronium formation is possible, provided $E > V_i - V_p$. As long as E is greater than the ionization energy (V_i) of the molecules however, simple ionization through inelastic collision is more likely than the formation of positronium. (If positronium is formed, the fast moving positronium atoms are very probably destroyed in the subsequent collisions.) If we assume that the positron after the last ionization collision has energy E between 0 and V_i, then the fraction V_p/V_i of these positrons can form positronium. This is the upper limit of probability for positronium formation. Since a part of these positrons have energies above the lowest electronic excitation energy of the molecules, this excitation, along with inelastic scattering of the positrons, will compete with positronium formation. If $V_1 > V_i - V_p$ then there exists a small energy region $V_1 - (V_i - V_p)$, the so-called "Ore gap" where the formation of positronium is likely. The fraction $[V_1 - (V_i - V_p)]/V_1$ becomes the lower bound for the probability of positronium formation.

1.4 The Quenching of Positronium

Following Green and Bell,[12] "quenching" of positronium will mean all possible processes introduced to shorten the lifetime of the ortho-positronium, i.e., reduction of 3γ annihilation.

The possible positronium quenching processes are as follows:

(1) The "pickoff" process: Due to the continual scattering of positronium by the surrounding molecules, the positron in ortho-positronium may annihilate with an electron from a molecule whose spin relative to the positron in the positronium is anti-parallel. This process of "pickoff" annihilation is now recognized generally to account for the long-lived component with a charateristic lifetime of about 10^{-9} seconds.

(2) Quenching by an external magnetic field: The states of positronium are influenced by an external magnetic field. The ground state of ortho-positronium ($^3S_1$) is about 8.4×10^{-4} ev. above the ground state of para-positronium ($^1S_0$). If positronium presents itself in a constant magnetic field, then the $^1S_0$ and $^3S_1$ levels are further split. This Zeeman effect produces a quadratic upward energy shift in $m = 0$ level of ortho-positronium ($^3S_{1,0}$). The two levels $m = \pm 1$ of the triplet ($^3S_{1,\pm 1}$) are unaffected by a magnetic field since there exist no $^1S_0$-components of the same m value, with which they could combine.[13] On the other hand, in a magnetic field

the m = 0 triplet state gets a small admixture of m = 0 singlet state which is equivalent to an increased probability for an ortho-para conversion.

(3) Paramagnetic quenching: The quenching of ortho-positronium might occur not only from the action of an external field, but also from the field of paramagnetic admixtures in the experimental sample. However, Ore[14] has shown that even for as paramagnetic a gas as oxygen, the spin flip through magnetic interaction would take $\sim 10^{-5}$ seconds, which is two orders of magnitude less than the rate of spontaneous 3-photon decay. Ferrell[15] suggested that the result of paramagnetic quenching of positronium is most likely due to "electron exchange" collisions of positronium with paramagnetic ions or any molecules with unpaired electrons.

(4) Chemical quenching: This quenching process involves various chemical reactions of positronium, such as the reaction of oxidation, addition, and substitution. For ortho-positronium all the processes indicated above reduce the lifetime to $\sim 10^{-10}$ seconds.[12,18]

1.5 Experimental Methods of Studying Positron Annihilation

There are in general three methods which are widely used in this field. We shall discuss first the measurement of the triplet annihilation rate by a triple coincidence experiment. Though this method is used less frequently than the others because of its experimental complexity, it is the easiest

to interpret. The measurement of the triple coincidence rate between the annihilation gamma photons tells us the number of positron-electron pairs annihilating from the triplet state. Whenever this rate is larger than 1/372 of the double photon rate which is predicted by the theory for a random orientation of the spins which has been mentioned previously, we assume that there is formation of positronium.

The second method is the measurement of the mean lifetime of positrons. The first lifetime determinations were made in gases by Deutsch[9] and this was followed by studies in solids by DeBenedetti et al.[15] The discovery of two lifetimes τ_1 and τ_2 was made by Bell and Graham.[16] It was assumed that the short lifetime τ_1 corresponded to the direct annihilation and/or to annihilation of singlet positronium, and that the longer meanlife τ_2 revealed the presence of triplet positronium. The intensity of the τ_2 component, I_2, can be measured, thus giving directly the percentage of triplet positronium formed, if all triplet is quenched and annihilates with mean life τ_2. From statistical considerations, triplet positronium should be formed three times as frequently as singlet positronium and hence the percentage of singlet positronium formed is equal to $I_2/3$.

The third method is the measurement of the angular correlation of the two-photon annihilation radiation. When a positron-electron pair at rest annihilates with the formation of two-photon emission, an energy of $2mc^2$ is released where m is the rest mass of electron and c is the velocity of light.

To conserve momentum, these two photons, each having a momentum mc, are emitted at 180-degree to each other in the center of mass system. If the annihilating pair has some momentum at the time of annihilation, then the photon pair will be emitted at angle differing from 180-degree by an amount of the order v/c, where v is the velocity of the center of mass of the annihilation pair. For low velocities this departure of the angle between the direction of the photons from 180 degrees is proportional to the component of momentum of the annihilating pair which is parallel to the bisector of the propagation direction. Thus, one may measure the angular distribution of annihilation photons and convert this to a momentum distribution of annihilation positron-electron pairs.[45] The detailed discussion with regard to this will be made in chapter 2.

1.6 Positronium and Chemistry

At present, the application of positron annihilation techniques covers two important fields, namely, chemistry and solid state physics.

Observations of the formation and annihilation of positronium in different media are of particular interest for chemical physicists. The formation of positronium is strongly related to the properties of the sample under investigation, such as the ionization and electronic excitation potentials, the elastic scattering cross-section, and the

excitation of vibrational and rotational molecular levels. Therefore the study of the probabilities of positronium formation under different conditions provides a new method of studying many elementary processes in chemistry.

Since positronium is the lightest hydrogen-like atom and an elementary free radical, the study of triplet positronium may shed light on the study of triplet states of complex molecules, and the study of positronium compounds may yield information on molecular energy levels and electron transfer mechanisms. Because of the short lifetime of positronium, it could provide a useful standard for investigations of rapid chemical reactions.

Unfortunately, the work of positronium chemistry has yet to yield significant results since there are only a few groups of chemists currently involved in the positronium research. However, as more chemists become familiar with positron analysis as a tool one would hope more meaningful experiments will be carried out.

Also of interest to the physicist is the experiment on the angular correlation of the two-photon annihilation radiation. The angular distribution of the photons yields important information about the momentum distributions of electrons involved in the chemical binding of molecular systems. Therefore, one may be able to use these data to check the calculated atomic and molecular orbital wave functions, in hope that it may help to improve the molecular orbital theory. On this basis, half of this work is concerned

with the detailed investigation of the momentum distributions of hydrocarbon molecular systems. It will be shown that the calculated momentum distribution functions are strongly dependent on the choice of space wave functions and that the use of accurate wave functions provides good agreement between calculated and experimental momentum distributions.

1.7 Positron Annihilation and Solid State Physics

The study of positron annihilation in metallic solids is probably the most fundamental application of positrons in solid state physics. The results of the studies of the angular distribution of annihilation radiation in metals has yielded data consistent with the assumption of a Fermi energy distribution for conduction electrons.[17,18] But since there are several other experimental methods[19] which can determine the Fermi surface, we can not say that these positron results represent any great progress in our knowledge of metals. But if one examines the methods currently being used to determine the Fermi surface carefully, one will find that in most of the methods, such as the de Haas-van Alphen effect, the magneto-acoustic effect, cyclotron resonance effect, and the galvanomagnetic effect, etc., a magnetic field is applied, producing a quantization of the electron energy levels (Landau levels). The effects under consideration are due to this quantization. In virtue of Heisenberg's uncertainty principle, the product of an electron lifetime

in a given state by the energy uncertainty is of the order of Planck's constant. The energy uncertainty must be kept sufficiently below the separation between the Landau levels, or otherwise these levels would be blurred and no longer defined, and the lifetime or relaxation time must therefore be as long as possible. Methods based on the quantization of Landau levels are thus only applicable to elements of sufficient purity, well-ordered alloys or intermetallic compounds and require the use of very low temperatures. In the methods, such as the anomalous skin effect, the sample must also be a very pure and perfect single crystal, in order to achieve a large electron mean free path. In contrast, the positron annihilation method does not require specimens of high purity or long electron mean free path, and thus can apply to any disordered lattice, such as a randon solid solution. This advantage may make it become one of the useful techniques for examining Fermi surface and electron structure of solids. Several alloys and liquid metals have been examined by this technique.[18] In this work, a ferromagnetic alloy, Alnico, has been studied by positron angular correlation technique; a Fermi energy for this alloy is determined. A detailed discussion of the result of this experiment will be made in chapter 6.

The investigations of positron annihilation in a complete series of rare earth elements indicated the number of valence electrons per atom for each element.[20,21] In the studies of positron annihilation in magnetized media, it was

proved[22] that in beta decay positrons are longitudinally polarized due to nonconservation of parity. By measuring the two-gamma angular correlation of polarized positron annihilation in ferromagnetic solids, one is able to obtain the momentum distribution of spin aligned electrons in solids studied, thus yielding important information of the study of ferromagnetism. The results in magnetized iron show[23,24,18] that the 3d electrons of magnetized iron are polarized, in agreement with the measurements from neutron diffraction,[25] and also show that electrons in the conduction band have an antiparallel polarization.

In addition to the study of metallic solids, a great variety of nonmetallic samples have also been investigated with both angular correlation and lifetime measurements. Among the nonmetallic elements which have been studied, the single crystal graphite sample showed a most interesting result in the angular distribution of the annihilation radiation which depended considerablly on the direction of orientation of the crystal and was accounted for in terms of electron orbital in the plane of the graphite and along the axis perpendicular to the plane.[26] In the studies of alkali halides, it is found that the angular distribution of the annihilation radiation of these salts depends almost exclusively on the nonmetallic ion (negative ion). This is understandable since the positrons are attracted by negative charges. In this work, an ionic crystal of perovskite

$(La_{.7}Pb_{.3})MnO_3$ has also been investigated, and the result shows that most of the positrons are concentrated at the site of the negative oxygen ions and annihilate with the 2s- and 2p-like electrons of the O^{--} ions.

Chapter 2

Experimental

2.1 General Description of Apparatus

A standard parallel slit angular correlation apparatus has been used to measure the angular distribution of annihilation photons. This apparatus has been described in detail previously[27] and therefore only the general description and modifications of the apparatus will be discussed here.

A. Mechanical

A diagram of the mechanical parts of the angular correlation apparatus is shown in Figure 2.1. The basic mechanical features are the source and sample housing, two gamma ray detectors, and the associated collimating slits. All of these components were mounted on two parallel aluminium "I" beams which were approximately 20 feet long and placed one foot apart and bolted with several cross bars.

The two gamma ray detectors were mounted on either end of the "I" beam structure. One detector was fixed and the other was movable. Both detectors were heavily shielded by lead, as shown in Figure 2.2b, to cut down the accidental background rate from scattered gamma rays and from other sources in the laboratory.

The source and the sample were shielded in a lead castle, as shown in Figure 2.2a, being placed on the middle of the "I"

FIGURE 2.1

The Angular Correlation Apparatus

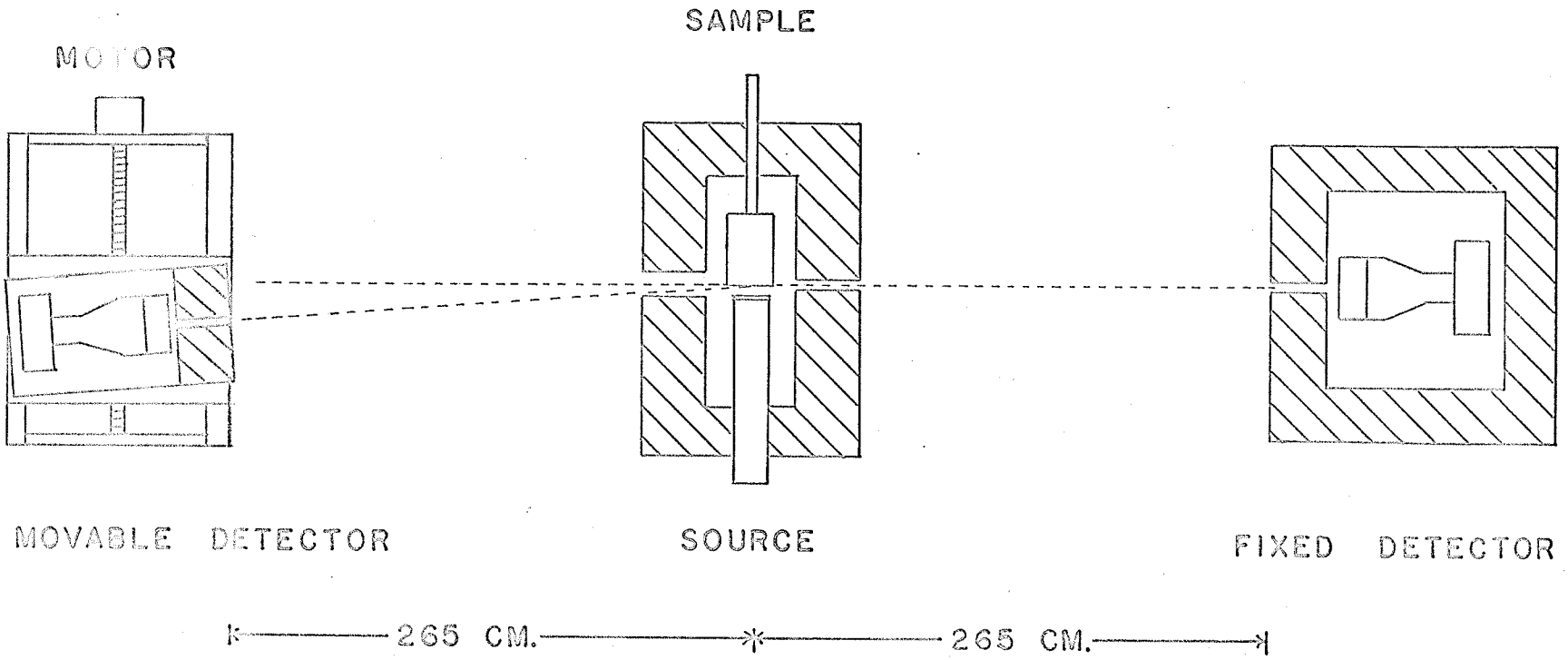
SAMPLE
MOTOR
MOVABLE DETECTOR
SOURCE
FIXED DETECTOR
265 CM.
265 CM.

Fig. 2.1

FIGURE 2.2

The Sample Housing (a) and the Movable Detector (b)

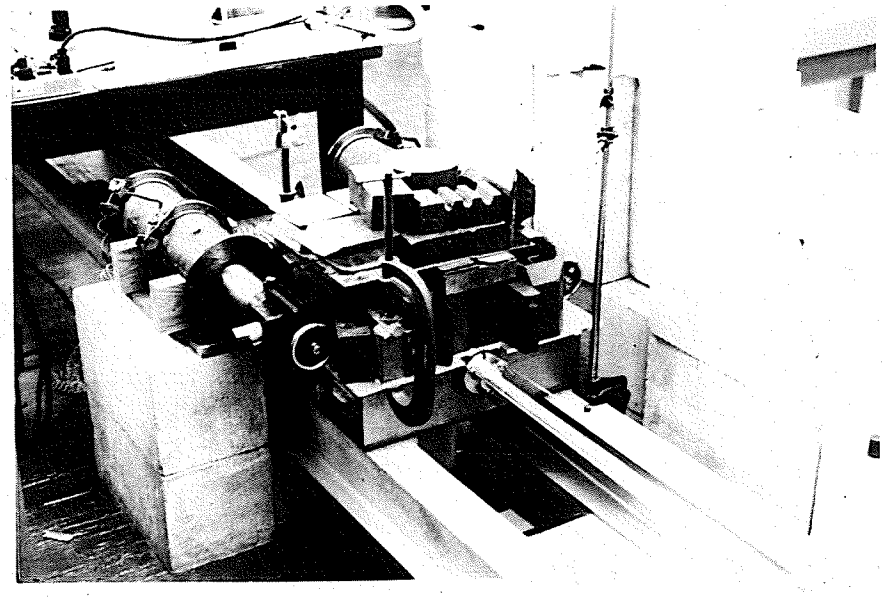

(a)

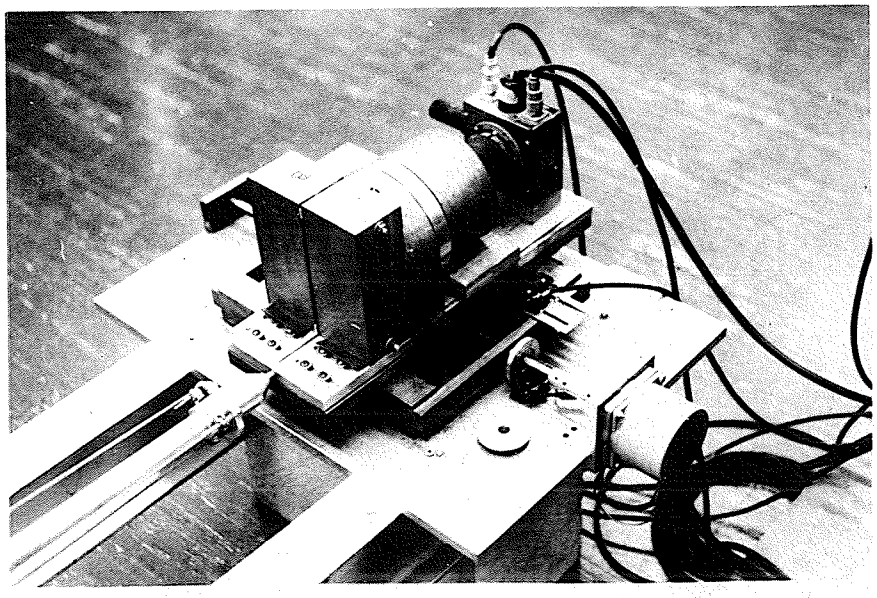

(b)

FIGURE 2.3

The Sample Cell (a) and the Sample Housing (b)

For the Low Temperature Experiment

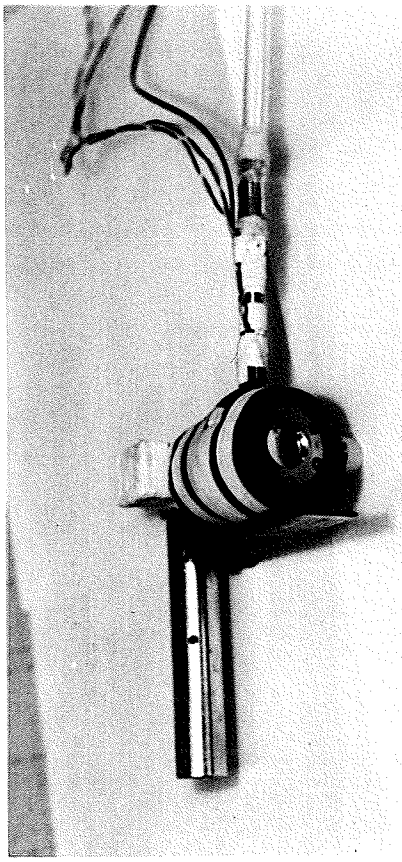

(a)

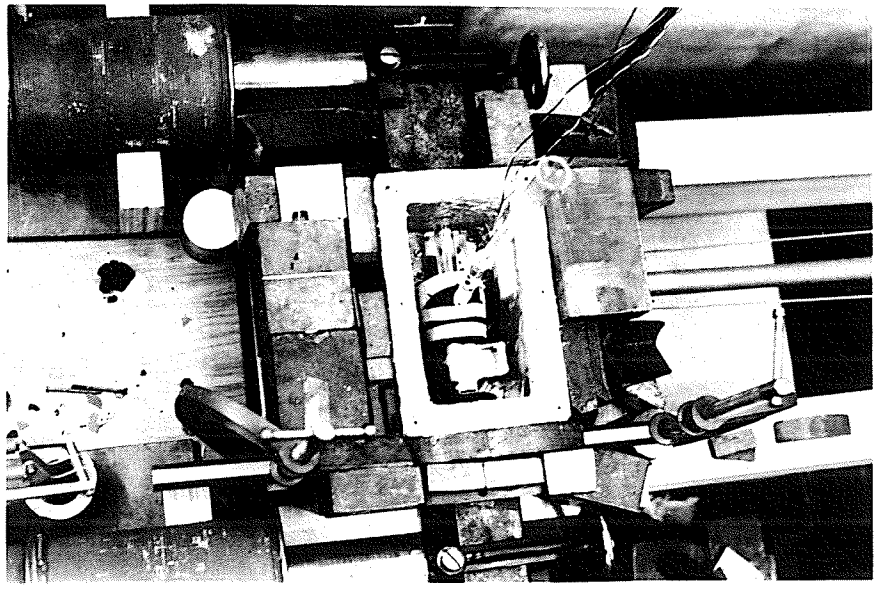

(b)

beams, with collimating slits of widths 0.16 cm and 1.5 cm, respectively, facing the fixed detector and the movable detector. The purpose of these collimating slits was to reduce the amount of scattered radiation reaching the detectors as well as to shield the detectors from the source. Also, the width of the fine slit, facing the fixed detector, can be used as an effective width of the sample to calculate the geometrical angular resolution of the apparatus. The detailed calculation of the angular resolution of this apparatus will be made in Appendix A.

To keep the collimating slits of the detectors aligned towards the sample as the movable detector progressed to different positions, an aluminium beam, as shown in Figure 2.2, which was reinforced by a set of three steel cables to both ends of the beam, was extended from the front of the rotatable steel plate to a pivot point directly under the sample. To allow for the slight increase in the distance from the detector to pivot point as the detector was moved off the center position, the end of the aluminium beam was permitted to slide freely in a hole in the pivot shaft.

B. Electronics

A block diagram of electronics is shown in Figure 2.4. The detectors were Integral Assembly model 16MB4/A-X and consisted of 4" diameter, 1" thick NaI(Tl) crystals mounted on 5018 HB photomultipliers with mu-metal shields. A positive

FIGURE 2.4

Block Diagram of the Apparatus

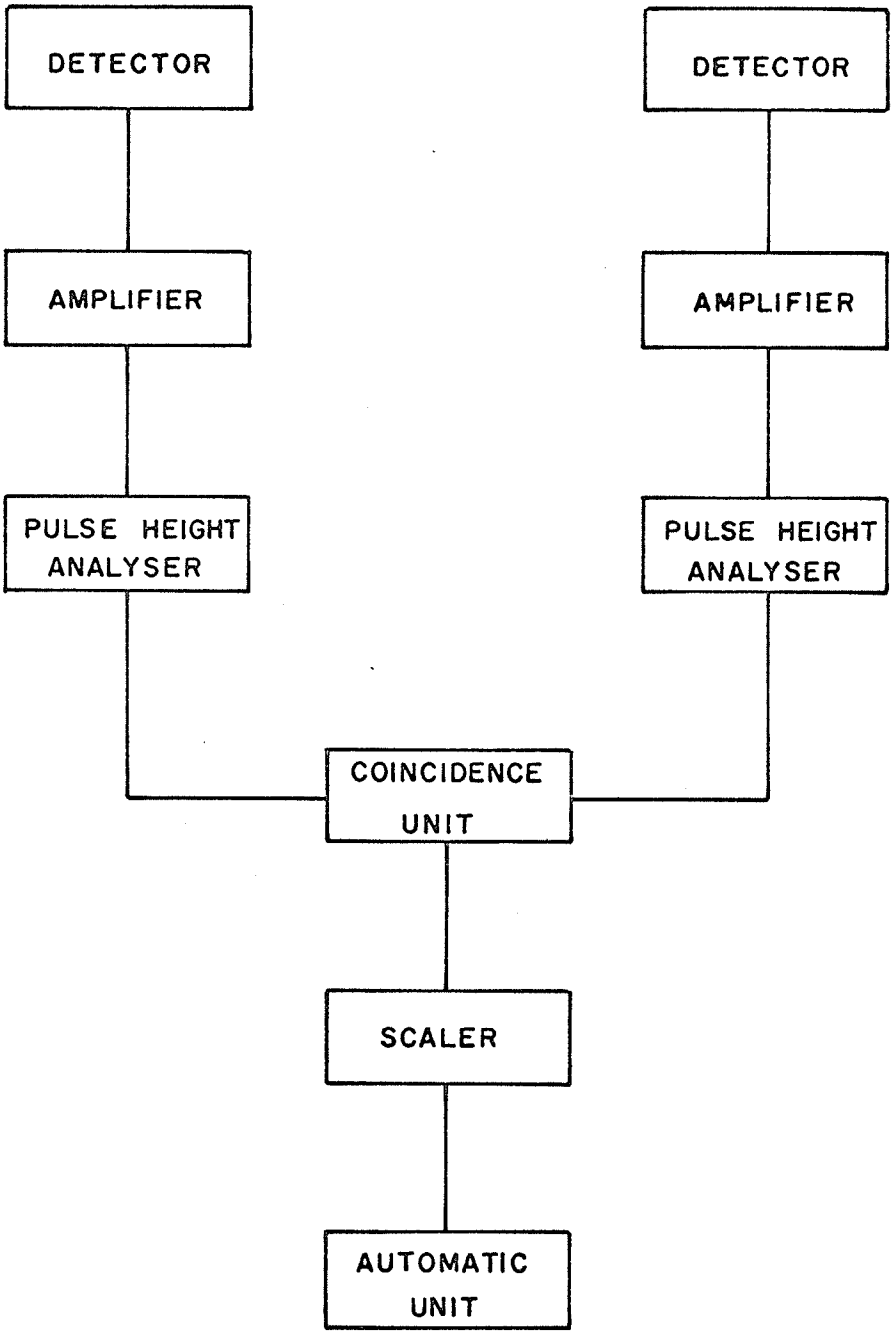
DETECTOR
DETECTOR
AMPLIFIER
AMPLIFIER
PULSE HEIGHT ANALYSER
PULSE HEIGHT ANALYSER
COINCIDENCE UNIT
SCALER
AUTOMATIC UNIT

high voltage (1100 volts) was provided for photomultipliers by a Hamner N401 high voltage supply. Negative pulses, which are of the order of one volt in amplitude, were fed from the cathode followers in the detector heads to amplifiers, and were amplified about five times and shortened to approximately one microsecond.

Pulses from the amplifiers were fed to transistorized single channel pulse height analysers set to select gamma rays in the energy range between 0.1 and 0.5 Mev. The fast rising narrow pulses were sent to a coincidence unit which has a resolving time of about 150 nanoseconds. The resolution time of the coincidence unit was determined by providing a random source of gamma rays for each detector, and measuring the chance coincidence counting rate and single counting rates, N_A and N_B, for the two detectors. The resolution time, T, was then calculated using the formula:

$$\text{Chance coincidence counting rate} = 2TN_AN_B.$$

A Technical Measurement Corporation Model SG-3A scaler was used to record the number of coincidences.

When 1000 counts have been accumlated on the scaler, through the "automatic unit" which has been described previously,[27] the track motor is started and moves the movable detector to its next position, simultaneously, the scaler stops counting as the motor is running, and the scaler starts counting again as soon as the motor stops while the detector has been driven

to its new position. When the detector moves to the predetermined end of its run in either direction (eg. 16 milliradians on each side), it will reverse the direction automatically by reversing switches in the automatic unit system. A Simplex Interval Timer Type ET-100 was used to print out the time interval during each 1000 counts of coincidences.

All the electronic instruments were powered by a model 2000 S Sorensen A.C. voltage regulator.

2.2 Positron Sources

Most of the experimental work was done with two Na^{22} positron sources. Cu^{64} was used occasionally when it was available.

The first Na^{22} source was 10 millicuries in the form of NaCl solution obtained from the Radiochemical Center, Amersham, England. The source had a high specific activity, 3 mc/mg, and was dissolved originally in 6 ml. of water. The source was evaporated from solution, drop by drop, on a $\frac{1}{2}$" diameter plastic button (which was prepared by machining shallow, concentric circular grooves on it) mounted on the end of a 10" long plastic rod, and then covered with a thin piece of mica (2 mg/cm^2) sealed around the sides of the button with epoxy resin glue. It was estimated that about 80% of the source was actually deposited on the plastic button as the evaporation process was finished. The remainder was left in the original source container, in the syringe, and

FIGURE 2.5

Positron Source (Na^{22})

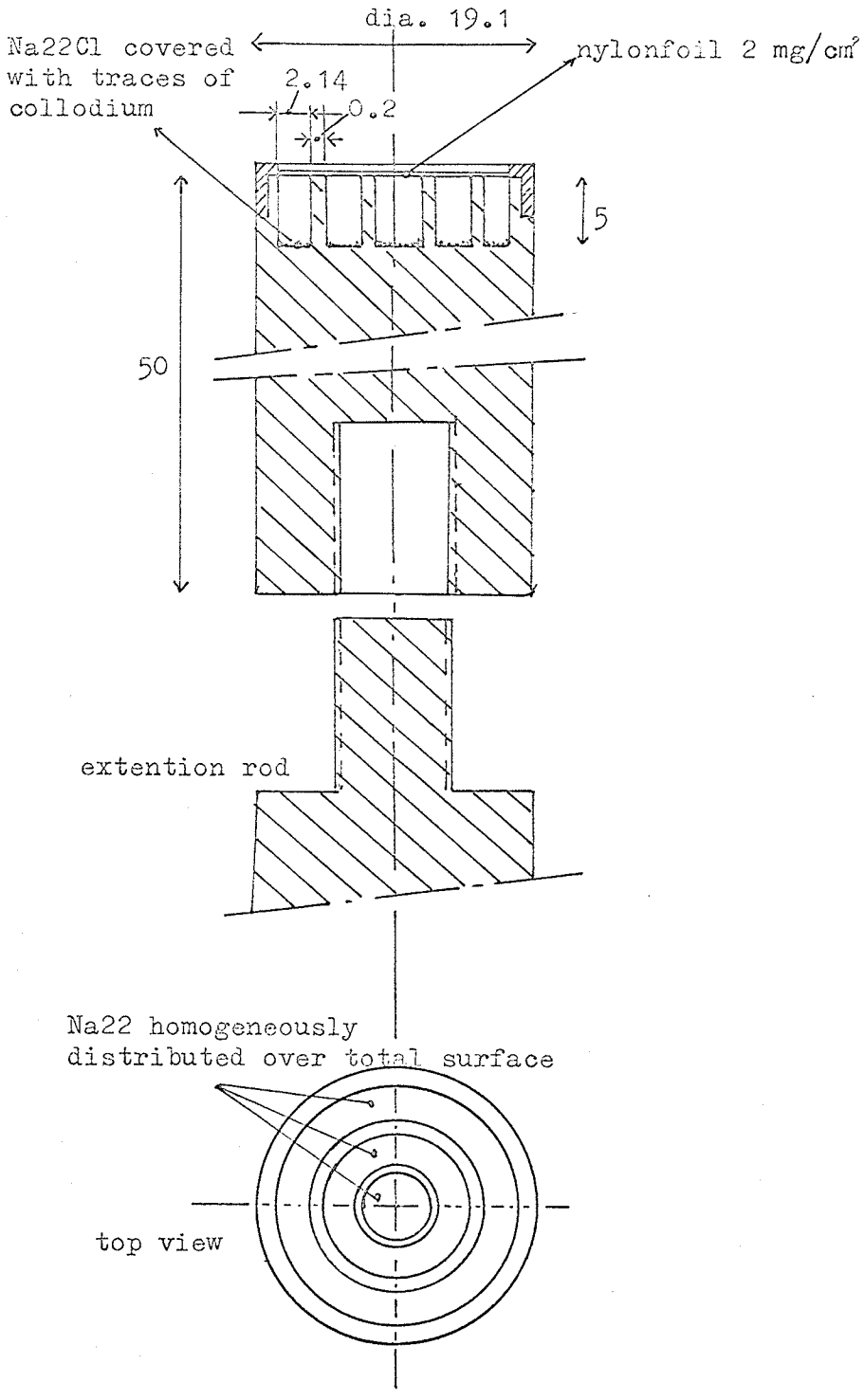

Measures in mm.

in the hypodermic needle.

For the above reason as well as for the reason of safety, the second Na^{22} source we used was already mounted on a perspex rod, as shown in Figure 2.5, in the Isotopes Laboratory, N.V. Philips-Duphar, Amsterdam, Nederland.

Ordinary Cu foils measuring 3/4 x 1/2 x 0.005 inches were prepared and sent to Pinawa, Atomic Energy of Canada Ltd. for pile irradiation. Since Cu^{64} has a half-life of 12.9 hours, some haste was necessary in making use of a foil after irradiation. The activity when used in the experiment was greater than 250 millicuries.

2.3 Sample Mounting

Ordinary liquid samples, e.g., hexane and decane, were contained in a small brass tank with a 3/4" vertical face covered with a thin mica window (1.5 mg/cm^2) so that more than 95% of the incident positrons could penetrate through the mica window and annihilate in the liquid sample.

The methane sample was contained in an aluminum cell, as shown in Figure 2.3a. The thickness of the aluminum window was approximately 4 mg/cm^2. The reason why one could not use a thinner window was that it had to be strong enough to withstand evacuation of the cell to a pressure $\sim$1 micron of Hg.

During the experiment the position of the sample cell was adjusted so that the fixed detector could only see a portion of the sample which was just inside the window and defined by

the narrow collimating slit of the sample housing. Therefore, no window correction was needed.

The solid samples, e.g., Alnico and $(Pb_{.7}La_{.3})MnO_3$, were mounted on the end of a 3/4" brass rod using a special mounting wax.

2.4 Distillation Apparatus and Methane Sample Preparation

A vacuum distillation apparatus was used for the preparation of methane samples. A diagram of the apparatus was shown in Figure 2.6. A glass tube connected the distillation apparatus to the sample cell.

Great care was taken to prevent contamination of the pure sample. High-vacuum stopcocks and ground glass joints were used with a minimum amount of high grade stopcock grease.

As shown in Figure 2.6, a mercury manometer safety valve was connected to the condensing tube and the sample cell. A thin layer of vacuum pump oil was introduced above the mercury column to prevent the diffusion of mercury vapor into the rest of the appratus.

Research grade of methane gas was obtained from Matheson of Canada, Ltd., Whithy, Ontario. This grade of methane is of the highest purity that is available. It had a minimum purity of 99.99 mole %.

After the whole system was evacuated to a pressure of 1 micron of Hg, the stopcocks between the sample cell and the cold trap were closed, and methane gas was then condensed in

FIGURE 2.6

Distillation Apparatus

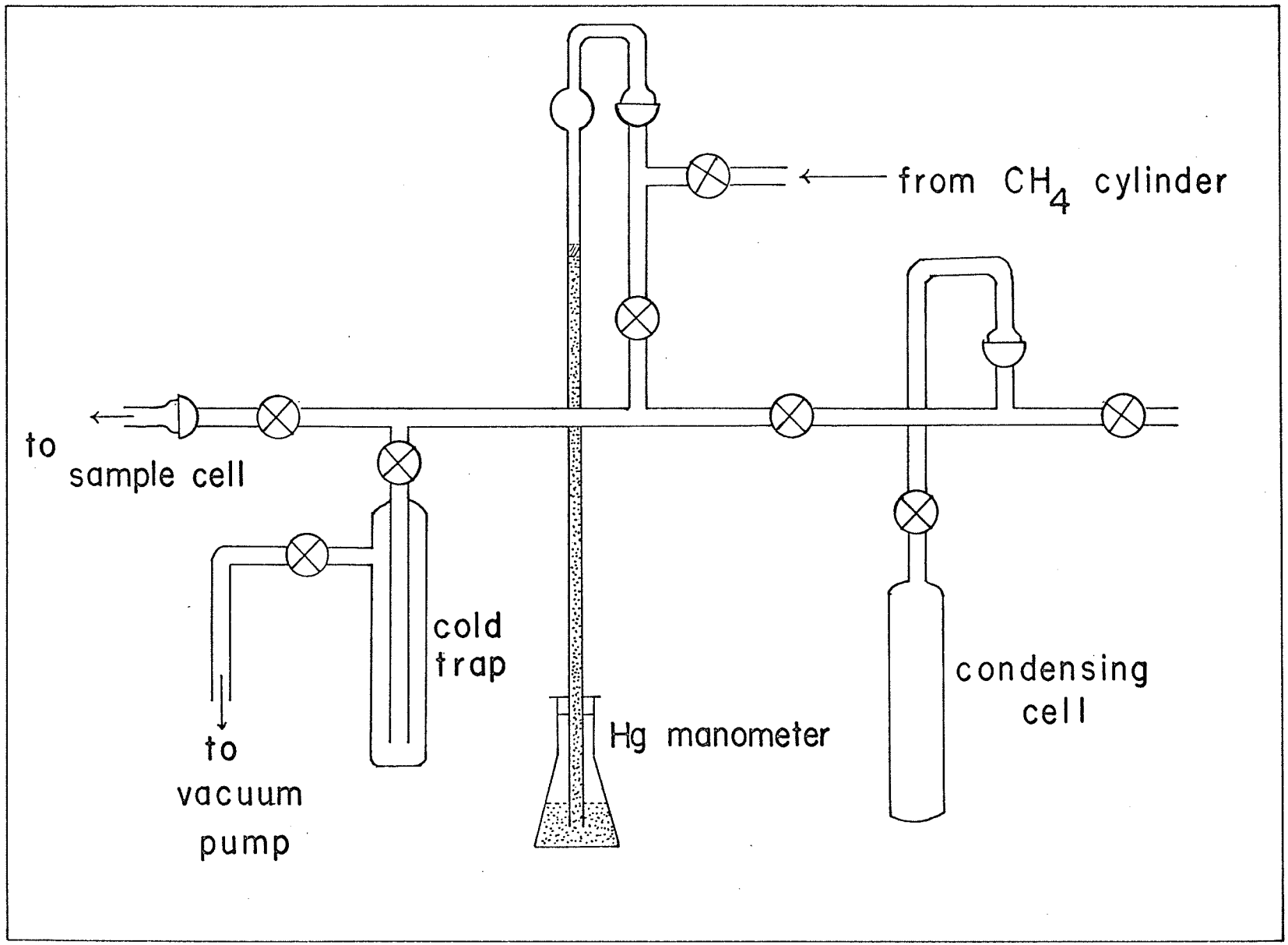
from CH_4 cylinder
to
sample cell
cold
trap
to
vacuum
pump
Hg manometer
condensing
cell

the condensing tube. A dewar of liquid nitrogen was used to cool the condensing tube. After a sufficient quantity ($\sim 7 cm^3$) of CH_4 was condensed, the valve of the gas cylinder and the stopcock between the cylinder and the condensing system were closed. When the sample cell in the sample housing was cooled down to the temperature of -177^oC, the stopcock between the sample cell and the condensing tube was opened, and the dewar of liquid nitrogen around the condensing tube was lowered down until the liquid nitrogen level just merely touched the bottom of the condensing tube. After the transfer was completed, the condensing tube was closed, and the sample cell then only connected to the mercury manometer safety valve. During the sample preparation procedure, a dewar of liquid nitrogen was kept around the cold trap.

2.5 Temperature Regulation for Methane Sample

Liquid nitrogen was used to cool the CH_4 sample. The aluminum sample cell (Figure 2.3a) was attached to an aluminum rod which extended downward into a reservoir dewar of liquid nitrogen. Liquid nitrogen was transferred from a 25-liter storage dewar through a well-insulated stainless steel tube to a small container attached to one side of the sample cell. The liquid nitrogen then passed through a small tube to the other side of the cell and then into the reservoir dewar.

A nitrogen level controller maintained the nitrogen level in the reservoir dewar. A circuit diagram for the controller is shown in Figure 2.7.

The operation of the level controller will outlined. A Keystone Type RL10X04-10K-315-S5 thermistor was used as the nitrogen level sensor. When the nitrogen level was below the sensor, the resistance of the thermistor, R_T(~20KΩ), was much smaller than R_1. The relay circuit was then open, the solenoid valve was closed, and the electric air pump pumped dry air into the liquid nitrogen storage dewar to build up the pressure for transferring liquid nitrogen into the reservoir dewar. As soon as the nitrogen level in the reservoir dewar was up to the thermistor, its resistance, R_T, increased rapidly to ~200KΩ. This caused the transistors Q_1 and Q_2 to turn on and activate a relay opening switch S_3 and closing S_2. The opening of S_3 stopped the air pump and the closing of S_2 opened the solenoid valve to vent the storage dewar; the transfer of liquid nitrogen then ceased. The liquid nitrogen in the reservoir dewar boiled-off slowly. As soon as its level was lower than the thermistor, R_T was reduced to its original value, and the relay circuit opened. Switches S_2 and S_3 then returned to their original positions. The transfer of the liquid nitrogen started again. The average time needed for one transfer cycle was $1\frac{1}{2}$ minutes. The system used about one liter of liquid nitrogen per hour.

FIGURE 2.7

The N_2 Level Controller

R_T ---- Thermistor

R_1 ---- 150 K

R_2 ---- 6.8K

R_3 ---- 15 K

C_1 ---- 50 μf

C_2 ---- 0.01 μf

Q_1 ---- 2N705

Q_2 ---- 2N964

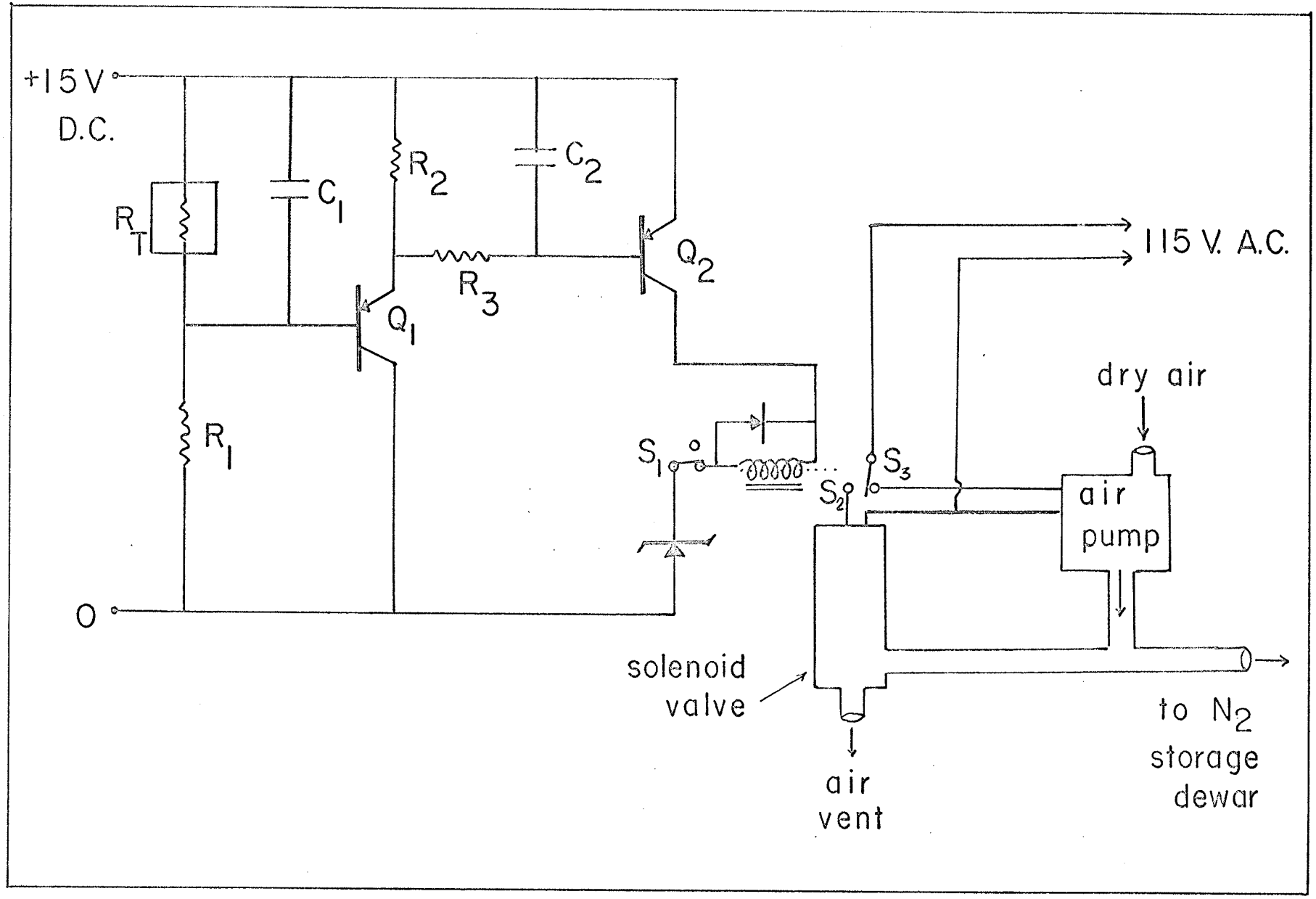
+15 V
D.C.
R_T
C_1
R_2
C_2
Q_2
R_3
Q_1
R_1
0
S_1
S_2
S_3
115 V. A.C.
dry air
air
pump
solenoid
valve
air
vent
to N_2
storage
dewar

Additional temperature regulation provided by a SCR (Silicon Controlled Rectifier) temperature controller was also used. The circuit used was similar to the one originally designed by McFee.[29] In fact, for a particular position of the liquid nitrogen level in the reservoir dewar, the temperature of the sample cell ordinarily reached its equilibrium temperature within a day and remained constant even without the help of the SCR temperature controller.

A copper-constantan thermocouple junction was epoxy cemented to the sample cell. The reference junction was kept at 0^{o} C in a dewar by a mixture of crushed ice and water. A potentiometer was used to measure the potential difference between thermocouple junctions. The temperature was obtained from a thermocouple temperature vs. potential calibration table.

During the experiment, the liquid methane sample was maintained at -177^{o}C and the solid sample at -187^{o}C. The temperature deviation was less than 1^{o}C.

The sample housing was well-insulated by a styrofoam box during the low temperature experiments.

2.6 Data Accumulation and Analysis

In almost all cases, at least ten and often twenty or more runs consisting generally of 1000 counts per point between 0 to 10 milliradians, and of 100 counts per point between 10 to 16 milliradians were taken on a sample. The

interval between the points was 0.907 milliradians except for some organic liquid samples where the interval between the points was 0.907/3 milliradians in the region between -4 to +4 milliradians. The average time for a run was usually about two days. A month or more was usually required to complete the investigation of one sample.

Each run was examined for any obvious irregularities which might be caused by electronic drifts or power failures in the building. If any irregularities were apparent, the whole run was discarded. After a complete set of data had been obtained, the total accumulated counts at each point was divided by the total time required for the accumulation. The data taken by Cu^{64} source were corrected for the exponential decay of source itself. Each angular distribution was plotted as counting rate vs. angle on semi-transparent graph paper. This was placed over a light box and folded to bring the points on either side of the distribution into as close agreement as possible thus determining the center of the distribution. In all cases, the angular distribution was symmetric within the experimental uncertainty.

To analyze the observed data, first we have to make a correction for the background distribution. The sources of background counts in the angular distributions will be outlined. The first was due to chance coincidences which contributed a flat background of about $\frac{1}{2}\%$ of the peak counting rate. This was determined by moving the movable detector 20 milliradians

off the 180-degree line so that coincidences from annihilations in the sample or any parts near the source would not be registered. Another measurement was also made by measuring the central counting rate with no sample tank inserted. This was approximately the same as the counting rate at 20 milliradians determined earlier. The background due to the window of the liquid sample cell has been neglected by the arrangement described in Section 2.3. Therefore only a correction for the background due to the very low number of chance coincidences was made.

Because of the finite angular resolution of the appratus, the background corrected angular distribution, $C'(\theta)$, is related to the true angular distribution, $C(\theta)$, by the following integral equation,

$$(2\text{-}1) \qquad C'(\theta_o) = \int_{-\infty}^{\infty} C(\theta)R(\theta_o-\theta)d\theta = \int_{-\infty}^{\infty} C(\theta_o-\theta)R(\theta)d\theta,$$

where $R(\theta)$ is the angular resolution function which has been calculated and discussed in detail in Appendix A.

In almost all solid samples studied, the observed angular distributions are quite broad, and since the samples are more dense, this results in a small positron penetration depth and a narrow resolution function. Therefore the resolution function can be treated as a delta function, i.e., $R(\theta_o-\theta) = \delta(\theta_o-\theta)$. Substitution of this into equation (2-1), yielded $C'(\theta_o) = C(\theta_o)$. Therefore no correction is needed for these broad distribution curves.

For the liquid samples, the angular distributions are

rather narrower. Therefore equation (2-1) must be solved for $C(\theta)$ to give the desired correction, and to do this, an iterative numerical technique was used. Each iteration generated an approximate solution $C_n(\theta_o)$, where n was the iteration number. This approximate solution was obtained from that of the preceding iteration by the relation:[30]

$$(2\text{-}2)\quad C_n(\theta_o) = C_{n-1}(\theta_o) + \left[C'(\theta_o) - \frac{\int_{-\infty}^{\infty} R(\theta_o-\theta) C_{n-1}(\theta) d\theta}{\int_{-\infty}^{\infty} R(\theta) d\theta} \right].$$

For the zeroth approximation, i.e., the initial estimate of $C(\theta_o)$, we used $C_0(\theta_o) = C'(\theta_o)$. The iteration was continued until some arbitrary degree of convergence was attained, i.e., $C_n(\theta_o) \doteq C_{n-1}(\theta_o)$. Usually this occurred within the first couple of iterations. The resulting correction to the angular distributions for liquid methane, hexane and decane are shown in Figure 2.8, 2.9, and 2.10 respectively.

Finally it is necessary to explain the physical meaning of the measured angular distribution $C(\theta)$. Following Stewart,[18] let us define $\varphi(\vec{p})$, the distribution of probability of finding a pair of photons with momentum $\vec{p}$ in $d\vec{p}$. Then the coincidence counting $C(\theta)$ obtained by the long slit type of apparatus is

$$C(p_z) = \int_{-\infty}^{\infty}\int_{-\infty}^{\infty} \varphi(\vec{p}) dp_x dp_y ,$$

where $p_z = mc\theta$. The Cartesian coordinates are defined as follows: The origin of system is at the mid-point of a line jointing the two detectors. The line is the x-axis.

The z-axis is parallel to the direction of motion of the movable detector, and the y-axis, of course, is vertical.

If $\varphi(\vec{p})$ is an isotropic function, it can be easily shown (see Section 3.3) that

$$\varphi(p) = \text{const.} \frac{1}{p_z} \cdot \frac{dC(p_z)}{dp_z} ,$$

and that the momentum distribution, N(p), is

$$N(p) = \text{const.}\ p_z \frac{dC(p_z)}{dp_z} .$$

In the following chapters the data will be presented in either C(p) vs. $\bar{p}$, or N(p) vs. p.

The slope of the angular distribution curve, dC/dp, was generally taken directly from the difference of adjacent measurements, viz.,

$$\left[\frac{dC(p)}{dp}\right]_{\text{at } p=(p_n+p_{n-1})/2} \frac{C(p_n) - C(p_{n-1})}{p_n - p_{n-1}} .$$

But in the higher momentum region where the statistics were poor because of the very low counting rate in this region, the slope was derived from a five-point least square fit of a parabola, viz.,

$$\left[\frac{dC(p)}{dp}\right]_{\text{at } p=p_n} = \left[2C(p_{n+2}) + C(p_{n+1}) - C(p_{n-1}) - 2C(p_{n-2})\right]/10.$$

FIGURE 2.8

Angular Distribution for Methane (CH_4)

The open circles indicate the experimental data for liquid methane (at -177°C) and the x's indicate the experimental data for solid methane (at -187°C). The dashed curve indicates the distribution for liquid methane corrected for finite angular resolution.

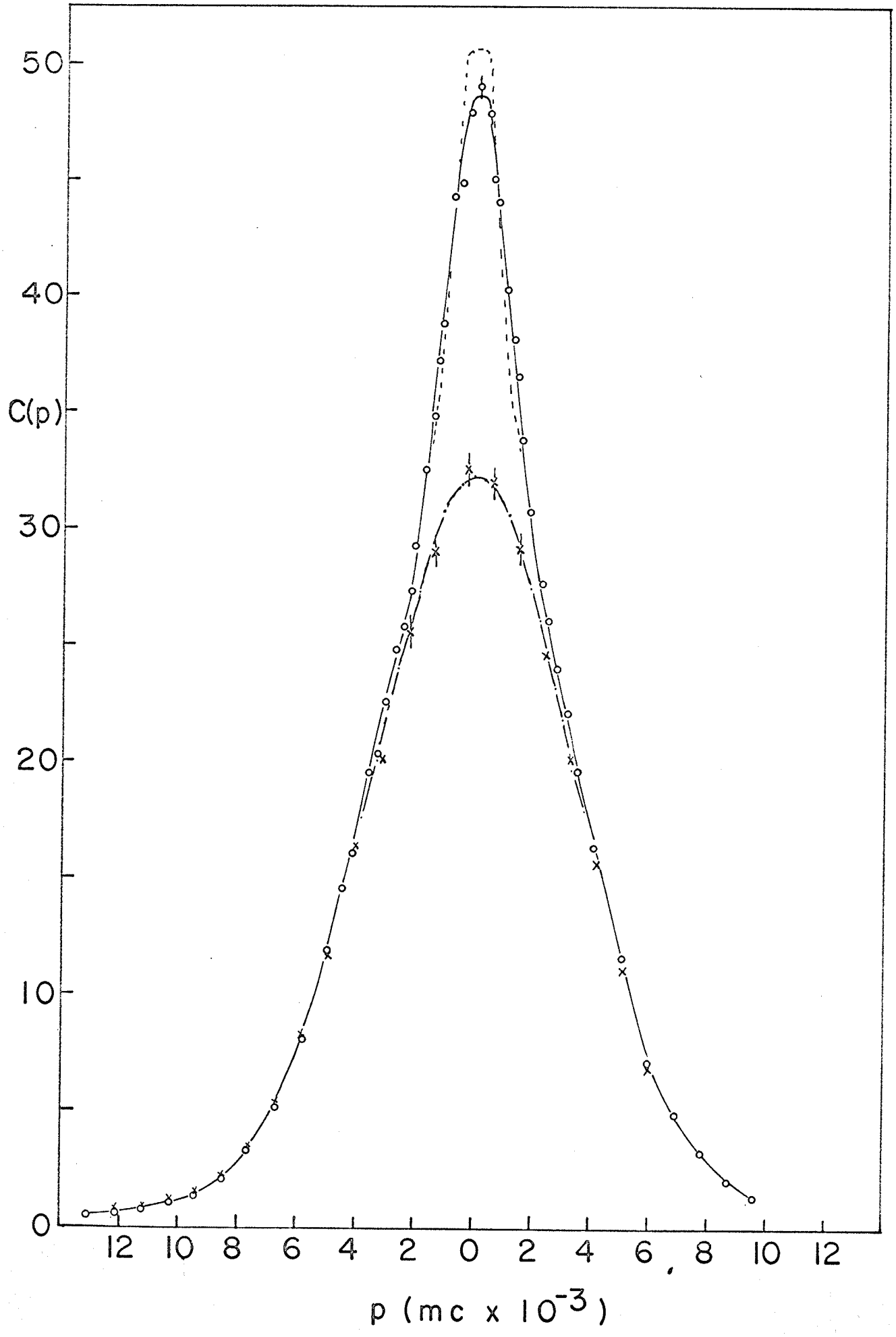
50
40
C(p)
30
20
10
0
12 10 8 6 4 2 0 2 4 6 8 10 12
p (mc x 10^-3)

FIGURE 2.9

Angular Distribution for Hexane (C_6H_{14})

The dashed curve indicates the distribution corrected for finite angular resolution.

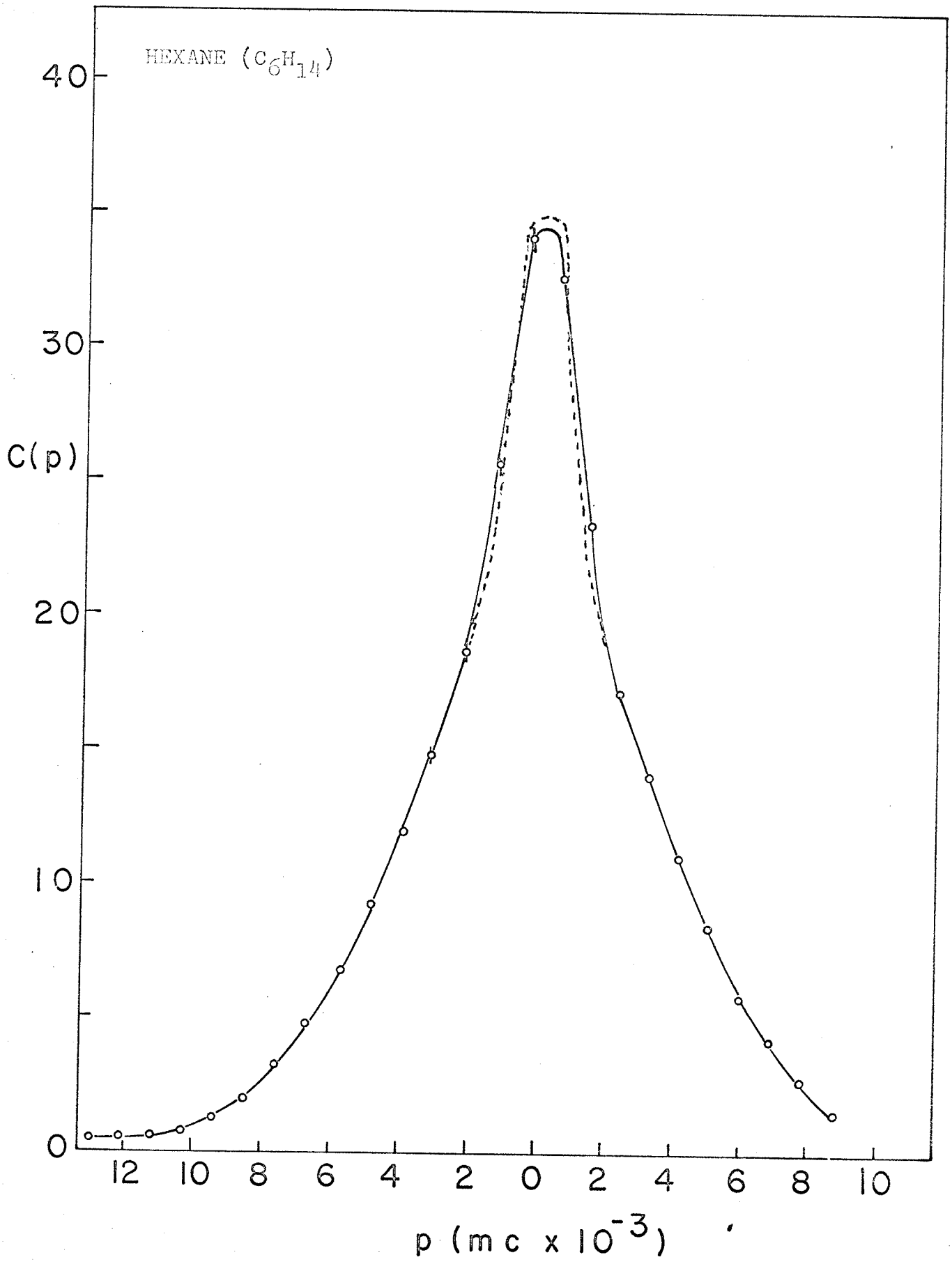
HEXANE (C_6H_{14})
40
30
20
10
0
C(p)
12
10
8
6
4
2
0
2
4
6
8
10
p (mc x 10^{-3})

FIGURE 2.10

Angular Distribution for Decane ($C_{10}H_{22}$)

The dashed curve indicates the distribution corrected for finite angular resolution.

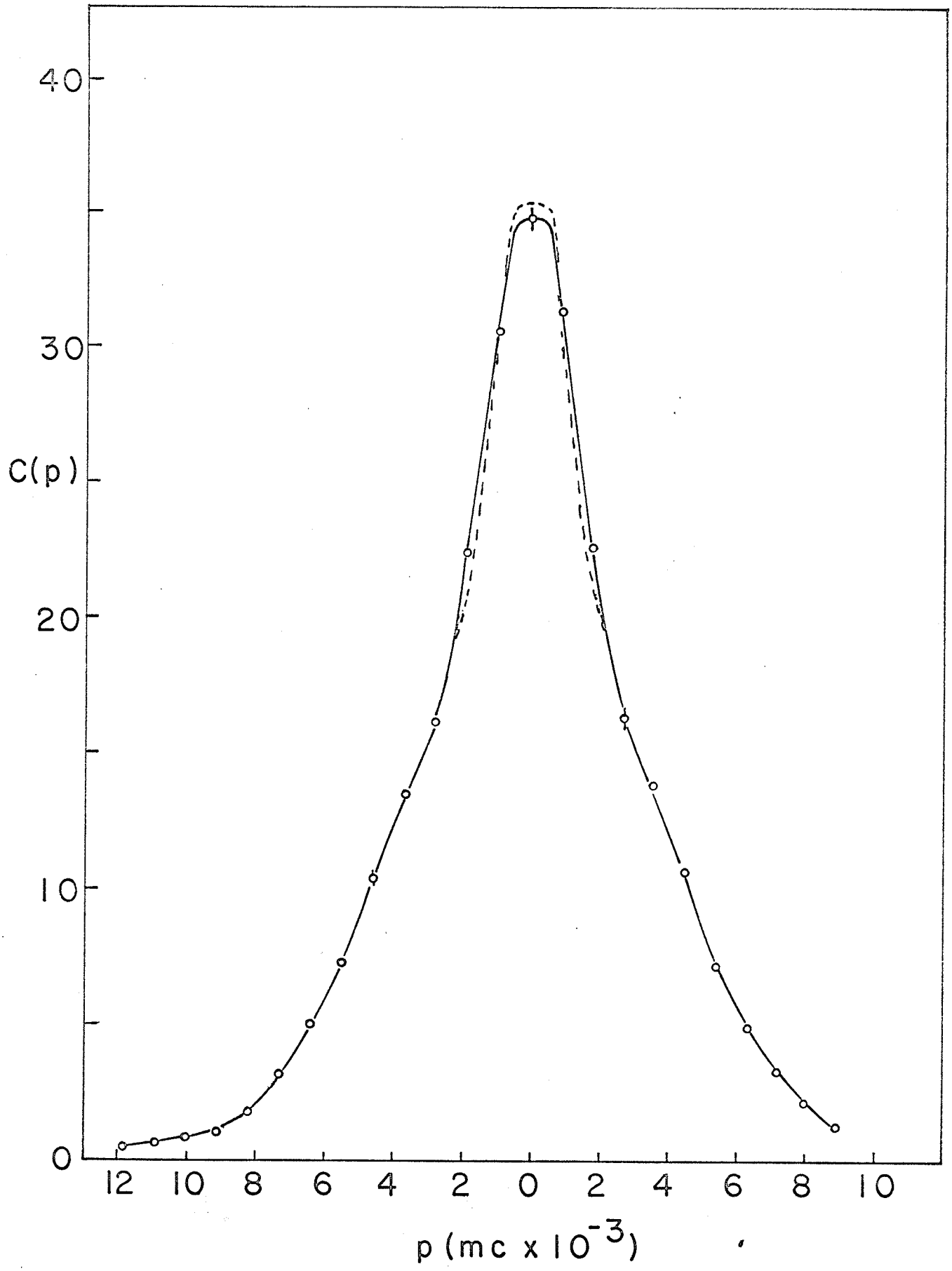
40
30
20
10
0
C(p)
12
10
8
6
4
2
0
2
4
6
8
10
p (mc x 10^-3)

Chapter 3

Positron Annihilation in Normal Hydrocarbon Systems. I. Electron Momentum Distributions

3.1 General

When a positron enters a condensed hydrocarbon compound it may annihilate with an electron in the C-H bond or in the C-C bond. From the measurement of the angular correlations of the annihilating photons, one is able to obtain information concerning the momentum distribution of electrons annihilating with positrons. Very little theoretical work has been done on momentum distributions either in atoms or molecules since the early 1940's. Most of our knowledge of momentum distributions for molecular systems comes from a series of papers given by Coulson and Duncanson.[31-37] The general method used to obtain the momentum wave function consists of transforming the space wave function to momentum coordinates according to the Dirac transformation theory. Coulson and Duncanson used the Slater type of hydrogen-like atomic wave functions to calculate the momentum distribution in simple molecular systems. Kerr et al[38] have used these results for the momentum distribution of the electrons in C-H and C-C bonds to calculate the electron momentum distribution in hexane and then they compared the calculate curve to the momentum distribution of the annihilating positron electron pairs observed from an angular correlation experiment. The agreement was good except in the high momentum region, where the theory predicts higher values than observed.

To examine the reasons for such a discrepancy, in the next section we recalculate the momentum distributions in C-C and C-H bonds by using the analytic SCF functions of atomic carbon orbitals calculated by Löwdin.[39] It will be shown that the use of these improved wave functions reduced the discrepancy between theory and experiment by a factor of 2.

3.2 Calculation of Electron Momentum Distributions

Before going into the detailed calculations of the momentum distributions of electrons in C-H bond and in C-C bond, we first calculate the momentum distribution of electrons in the hybrid atomic carbon orbitals.

A. The Momentum Distribution in the Hybrid Carbon Orbital

The hybrid orbitals of the carbon atom are described by the wave function

$$(3\text{-}1) \qquad \psi(C) = \frac{\psi_{2s}(C) + \sigma \psi_{2p}(C)}{\sqrt{1+\sigma^2}} \ ,$$

where $\psi_{2s}(C)$ and $\psi_{2p}(C)$ are the analytic SCF functions of 2s and 2p atomic orbitals and have the form

$$(3\text{-}2) \qquad \psi_{2s}(C) = \left\{ \sum_k A_k \exp(-a_k r) - r \sum_k B_k \exp(-b_k r) \right\} / \sqrt{4\pi} \ ,$$

$$(3\text{-}3) \qquad \psi_{2p}(C) = \left\{ r \sum_k C_k \exp(-c_k r) \right\} \frac{\sqrt{3}}{\sqrt{4\pi}} \cos\theta .$$

The coefficients A_k, B_k, C_k, ... etc. in equations (3-2) and (3-3) are given tn Table 3.1.

TABLE 3.1

k	1	2	3
A_k	5.9095		
a_k	3.9471		
B_k	2.5829	5.2230	4.5676
b_k	1.4784	2.8493	7.7990
C_k	0.87935	3.3336	2.1226
c_k	1.0789	2.1444	5.9216

And σ, in equation (3-1), is called the coefficient of mixing. For the tetrahedral bonding σ is equal to $\sqrt{3}$. In all our calculations we use atomic units with $e = m = \hbar = 1$, and $c = 137$.

According to the Dirac transformation, the momentum wave function for the hybrid carbon orbitals can be written as

$$(3\text{-}4) \qquad \chi_C(\vec{p}) = (2\pi)^{-3/2} \int \exp(-i\vec{p}\cdot\vec{r})\,\psi(C)\,d\vec{r};$$

if $N_C(p)dp$ is the probability that the momentum lies between p and p+dp, then we we have the momentum distribution function, $N_C(p)$, which is the average of $\chi_C(\vec{p})^*\chi_C(\vec{p})$ over all directions

in the momentum space, i.e.,

$$(3\text{-}5)\quad N_C(p)=\int_0^{\pi}\chi_C(\vec{p})^*\chi_C(\vec{p})\cdot 2\pi p^2\sin\Theta\, d\Theta \quad ,$$

in which we have assumed that the momentum distribution is isotropic. Here we define (r, θ, φ) and (p, Θ, Φ) as space coordinates and momentum coordinates respectively.

To solve the equation (3-4), it is convenient to expand $\exp(-i\vec{p}\cdot\vec{r})$ into normalized spherical harmonics referred to some arbitrary fixed set of axes, and apply the addition theorem, i.e.,

$$(3\text{-}6)\quad \exp(-i\vec{p}\cdot\vec{r})=\sum_{\ell=0}^{\infty}(2\ell+1)(-i)^{\ell}P_{\ell}(\cos\theta)P_{\ell}(\cos\Theta)j_{\ell}(pr),$$

where $j_\ell(pr)$ is a spherical Bessel function, and $P_\ell(\cos\theta)$ and $P_\ell(\cos\Theta)$ are Legendre's polynomials, then we substitute equations (3-6), (3-1), (3-2) and (3-3) into equation (3-4) and use orthogonality properties of the Legendre's polynomials, i.e.,

$$\int_{-1}^{1}P_{\ell}(x)\,P_{\ell'}(x)dx=\frac{2}{2\ell+1}\,\delta_{\ell\ell'} \quad ,$$

we get

$$(3\text{-}4')\quad \chi_C(\vec{p})=(2\pi)^{-3/2}\,(1+\sigma^2)^{-\frac{1}{2}}\left[2\sqrt{\pi}\int_0^{\infty}j_0(pr)R_{2s}(C)r^2dr\right.$$

$$\left.+\,i\,2\sqrt{3\pi}\,\sigma\cos\Theta\int_0^{\infty}j_1(pr)R_{2p}(C)r^2dr\right] ,$$

where $R_{2s}(C)$ and $R_{2p}(C)$ are 2s and 2p radial wave functions of carbon given in equations (3-2) and (3-3) respectively, and the spherical Bessel functions $j_o(pr)$ and $j_1(pr)$ are

$$j_o(pr) = \sin(pr)/(pr) ,$$

$$j_1(pr) = \sin(pr)/(pr)^2 - \cos(pr)/(pr).$$

The integrations in equation (3-4') can be easily worked out by a standard method (see Appendix B). The final result of $\chi_C(\vec{p})$ is

$$(3\text{-}4'') \quad \chi_C(\vec{p}) = \frac{2}{\pi\sqrt{1+\sigma^2}} \sum_k \left[A_k \frac{a_k}{(a_k^2 + p^2)^2} - B_k \frac{(3b_k^2 - p^2)}{(b_k^2 + p^2)^3} \right]$$

$$+ i \frac{\sqrt{6}\ \sigma}{\pi\sqrt{1+\sigma^2}} \cos\Theta \sum_k C_k \left[\frac{c_k(c_k^2 - 3p^2)}{p(c_k^2 + p^2)^3} - \frac{c_k}{p(c_k^2 + p^2)^2} \right].$$

Therefore, the momentum distribution function of equation (3-5) becomes

$$(3\text{-}5') \quad N_C(\vec{p}) = \frac{8p^2}{\pi(1+\sigma^2)} \left\{ \left| \sum_k \left[A_k \frac{a_k}{(a_k^2 + p^2)^2} - B_k \frac{(3b_k^2 - p^2)}{(b_k^2 + p^2)^3} \right] \right|^2 \right.$$

$$\left. + \sigma^2 \left| \sum_k C_k \left[\frac{c_k(c_k^2 - 3p^2)}{p(c_k^2 + p^2)^3} - \frac{c_k}{p(c_k^2 + p^2)^2} \right] \right|^2 \right\} .$$

B. The Momentum Distribution in the Hydrogen 1s Orbital

Similarly, the momentum distribution in the 1s hydrogen orbital, $N_H(p)$, can be easily worked out. The momentum wave function is

$$\chi_H(\vec{p}) = (2\pi)^{-3/2} \int \exp(-i\vec{p}\cdot\vec{r})\, \psi_{1s}(H)\, d\vec{r} \ ,$$

where $\psi_{1s}(H) = \frac{1}{\sqrt{\pi}} \exp(-r)$, is the 1s hydrogen wave function, and

$$(3\text{-}6) \quad N_H(p) = \int_0^{\pi} \chi_H(\vec{p})^* \chi_H(\vec{p}) \cdot 2\pi p^2 \sin\Theta \, d\Theta$$

$$= 4\pi p^2 \left| (2\pi)^{-3/2} \int_0^{\infty} \frac{1}{\sqrt{\pi}} \exp(-r) \frac{\sin(pr)}{pr} 4\pi r^2 dr \right|^2$$

$$= \frac{32\, p^2}{\pi(1+p^2)^4} \ .$$

C. The Momentum Distribution in the C-H Bond

We used the Heitler-London or valence bond (VB) wave function for the two electrons that are paired to form the C-H bond. This type of wave function is known to be a good approximation for the covalent bond, such as the C-H bond is supposed to be. If we number the electrons of the bond by 1 and 2, the wave function of the C-H bond, $\psi(C\text{-}H)$, is

$$(3\text{-}7)\quad \psi(C\text{-}H)= \frac{\psi(C:1)\psi(H:2) + \psi(C:2)\psi(H:1)}{\sqrt{2(1+S_{CH}^2)}}$$

where $S_{CH}= \int \psi(C:1)\psi(H:1)dv_1$, is an overlap integral.

To calculate the momentum distribution, N(C-H), from equation (3-7), using a method similar to that introduced by Coulson, we first transform electron 1 into momentum coordinates, leaving electron 2 in space coordinates, i.e.,

$$\chi(\vec{p}_1,\vec{r}_2)= (2\pi)^{-3/2} \int \exp(-i\vec{p}_1\cdot\vec{r}_1)\psi(C\text{-}H)d\vec{r}_1$$

$$= (2\pi)^{-3/2} \left[2(1+S_{CH}^2)\right]^{-\frac{1}{2}}\left\{\int \exp(-i\vec{p}_1\cdot\vec{r}_1)\psi(C:1)\psi(H:2)d\vec{r}_1\right.$$

$$\left. +\int \exp\left[-i\vec{p}_1\cdot(\vec{r}_H+\vec{R}_{CH})\right]\psi(C:2)\psi(H:1)d\vec{r}_1\right\}$$

$$= \left[2(1+S_{CH}^2)\right]^{-\frac{1}{2}}\left\{\chi_C(\vec{p}_1)\psi(H:2) + \exp(-i\vec{p}_1\cdot\vec{R}_{CH})\psi(C:2)\chi_H(\vec{p}_1)\right\},$$

where R_{CH} is the length of the C-H bond, and then we average $\chi(\vec{p}_1,\vec{r}_2)^*\chi(\vec{p}_1,\vec{r}_2)$ over all positions of electron 2, i.e.,

$$\chi(\vec{p}_1)^*\chi(\vec{p}_1)=\int\chi(\vec{p}_1,\vec{r}_2)^*\chi(\vec{p}_1,\vec{r}_2)d\vec{r}_2$$

$$= \left[\chi_C(\vec{p}_1)^*\chi_C(\vec{p}_1) + \chi_H(\vec{p}_1)^*\chi_H(\vec{p}_1) + S_{CH}\,\chi_C(\vec{p}_1)\chi_H(\vec{p}_1)^*\exp(-i\vec{p}_1\cdot\vec{R}_{CH})\right.$$

$$\left. +S_{CH}\,\chi_C(\vec{p}_1)^*\chi_H(\vec{p}_1)\exp(i\vec{p}_1\cdot\vec{R}_{CH})\right] / \left[2(1+S_{CH}^2)\right] .$$

This gives us the momentum space density of electron 1.

Of course, the momentum space density of electron 2 is the same as for electron 1. Therefore the momentum distribution for the C-H bond is

$$(3\text{-}8) \qquad N(C\text{-}H) = \int_0^{\pi} \chi(\vec{p})^* \chi(\vec{p}) \cdot 2\pi p^2 \cdot \sin\Theta \, d\Theta$$

$$= \left[N_C(p) + N_H(p) + 2S_{CH} \, N_{ch}(p) \right] / \left[2(1 + S_{CH}^2) \right],$$

where $N_C(p)$ and $N_H(p)$ are given in equations (3-5') and (3-6), respectively, and

$$N_{ch}(p) = \frac{16\,p}{\pi R_{CH} \sqrt{1+6^2}\,(1+p^2)^2} \left\{ \sum_k \left[A_k \frac{a_k}{(a_k^2+p^2)^2} - B_k \frac{(3b_k^2-p^2)}{(b_k^2+p^2)^3} \right] \sin(pR_{CH}) \right.$$

$$\left. + \sqrt{3}\,6 \sum_k C_k \left[\frac{c_k(c_k^2-3p^2)}{p(c_k^2+p^2)^3} - \frac{c_k}{p(c_k^2+p^2)^2} \right] \cdot \left[\cos(pR_{CH}) - \frac{\sin(pR_{CH})}{pR_{CH}} \right] \right\},$$

in which the value of R_{CH} is taken to be 2.0 a.u. The overlap intergral, S_{CH}, can be evaluated by a standard method (Appendix C).

D. The Momentum Distribution in the C-C bond

The calculation of the momentum distribution in the C-C bond, N(C-C), is similar to that for N(C-H). The C-C bond is described by the wave function

$$(3\text{-}9)\quad \psi(C\text{-}C) = \frac{\psi_a(C:1)\,\psi_b(C:2) + \psi_a(C:2)\,\psi_b(C:1)}{\sqrt{2(1+S_{ab}^2)}}$$

where $S_{ab}=\int\psi_a(C:1)\,\psi_b(C:1)dv_1$, is an overlap integral, and $\psi_a(C)$ and $\psi_b(C)$ are the wave functions for the two carbon atoms in the C-C bond.

The calculation of the Fourier transformation from equation (3-9) follows similar lines to that for N(C-H). First we transform number 1 electron into the momentum space, i.e.,

$$\chi(\vec{p}_1,\vec{r}_2) = (2\pi)^{-3/2}\int\exp(-i\vec{p}_1\cdot\vec{r}_1)\,\psi(C\text{-}C)d\vec{r}_1$$

$$= (2\pi)^{-3/2}\left[2(1+S_{ab}^2)\right]^{-\frac{1}{2}}\left\{\int\exp(-i\vec{p}_1\cdot\vec{r}_{1a})\psi_a(C:1)\psi_b(C:2)d\vec{r}_{1a}\right.$$

$$\left.+\int\exp\left[-i\vec{p}_1\cdot(\vec{r}_{1b}+\vec{R}_{CC})\right]\psi_a(C:2)\psi_b(C:1)d\vec{r}_{1b}\right\}$$

$$= \left[2(1+S_{ab}^2)\right]^{-\frac{1}{2}}\left\{\chi_C(\vec{p}_1)\psi_b(C:2) + \exp(-i\vec{p}_1\cdot\vec{R}_{CC})\psi_a(C:2)\chi_C(\vec{p}_1)\right\},$$

where R_{CC} is the length of the C-C bond, and then we average $\chi(\vec{p}_1,\vec{r}_2)^*\chi(\vec{p}_1,\vec{r}_2)$ over all positions of electron 2, i.e.,

$$\chi(\vec{p}_1)^*\chi(\vec{p}_1) = \int\chi(\vec{p}_1,\vec{r}_2)^*\chi(\vec{p}_1,\vec{r}_2)dv_2$$

$$= \chi_C(\vec{p}_1)^*\chi_C(\vec{p}_1)\left[1+S_{ab}\cos(p_1R_{CC}\cos\Theta)\right]/(1+S_{ab}^2).$$

Then we have the momentum distribution in the C-C bond,

$$(3\text{-}10)\qquad N(C\text{-}C)=\int \chi(\vec{p})^{*}\chi(\vec{p})\cdot 2\pi p^{2}\sin\Theta\, d\Theta$$

$$=\left[N_{C}(p)+S_{ab}\,N_{ab}(p)\right]/(1+S_{ab}^{2})\ ,$$

where $N_C(p)$ is given in equation (3-5'), and

$$N_{ab}(p)=\frac{8p^{2}}{\pi(1+\sigma^{2})}\left\{\left|\sum_{k}\left[A_{k}\frac{a_{k}}{(a_{k}^{2}+p^{2})^{2}}-B_{k}\frac{(3b_{k}^{2}-p^{2})}{(b_{k}^{2}+p^{2})^{3}}\right]\right|^{2}\cdot\frac{\sin(pR_{CC})}{pR_{CC}}\right.$$

$$+3\sigma^{2}\left|\sum_{k}C_{k}\left[\frac{c_{k}}{(c_{k}^{2}\ p^{2})^{2}}-\frac{c_{k}(c_{k}^{2}-3p^{2})}{p(c_{k}^{2}\ p^{2})^{3}}\right]\right|^{2}\cdot\left[\frac{\sin(pR_{CC})}{pR_{CC}}\right.$$

$$\left.\left.+\frac{2\cos(pR_{CC})}{(pR_{CC})^{2}}-\frac{2\sin(pR_{CC})}{(pR_{CC})^{3}}\right]\right\},$$

in which R_{CC} is taken to be 2.9 a.u. N(C-C) and N(C-H) were computed on IBM 360-65, and plotted in Figure 3.1.

3.3 Application to Positron Annihilation in Methane, Hexane, and Decane

The probability that an electron with wave function $\psi(\vec{r})$ will annihilate with a thermalized positron with wave function $\psi_{+}(\vec{r})$ and yield a photon pair with center of mass

momentum $\vec{p}$ is proportional to

$$(3\text{-}11) \qquad \varphi(\vec{p}) = \left| \int \psi(\vec{r})\, \psi_{+}(\vec{r}) \cdot \exp(-i\vec{p}\cdot\vec{r})\, d\vec{r} \right|^2$$

where the integration is over the entire sample. In the usual parallel slit apparatus, as described in Chapter 2, all photon pairs with a particular component of center-of-mass momentum $\vec{p}$ are measured, and the counting rate is proportional to

$$(3\text{-}12) \qquad C(p_z) = \int_{-\infty}^{\infty}\int_{-\infty}^{\infty} \varphi(\vec{p})\, dp_x dp_y$$

$$= \int_0^{\infty} \varphi(\vec{p})\, 2\pi P\, dP \qquad (P = \sqrt{p_x^2 + p_y^2}).$$

If we put $P^2 + p_z^2 = p^2$ and transform the variable to p, we get

$$(3\text{-}12') \qquad C(p_z) = 2\pi \int_{p_z}^{\infty} \varphi(\vec{p})\, p\, dp$$

$$= \tfrac{1}{2} \int_{p_z}^{\infty} \frac{N(p)}{p}\, dp$$

where $N(p) = \int_0^{\pi} \varphi(\vec{p})\, 2\pi p^2 \cdot \sin\Theta\, d\Theta$, is the momentum distribution function assuming $\varphi(\vec{p})$ is isotropic, which is true only for liquid and polycrystalline solid samples.

Now we can see the relation between the observed counting rate, $C(p_z)$, and the momentum distribution function,

$N(p_z)$, by differentiating the above equation, finally we get

$$(3\text{-}13) \qquad N(p_z) = -\text{constant} \cdot p_z \frac{dC(p_z)}{dp_z} \quad .$$

If we assume that the positron wave function is a plane wave with small momentum, then $\psi_+(\vec{r})$ is nearly constant everywhere in the space. Therefore $\rho(\vec{p})$ in equation (3-11) is now equivalent to the electron momentum density, and N(p) is equal to the electron momentum distribution function.

Now we are able to construct the total momentum distribution for methane, hexane, and decane from the results of Section 3.2, and compare these with the experimental results obtained from positron annihilation data.

Since a methane molecule consists of four tetrahedral C-H bonds, the momentum distribution, N(Methane), is just equal to N(C-H) in equation(3-8).

The momentum distributions for hexane and decane can be obtained by considering that only electrons from C-H and C-C bonds annihilate with the positrons and that annihilation is equally probable for an electron from either of these bonds. We will neglect the contribution due to carbon 1s electrons since the overlapping of wave functions of these core electrons with that of positrons is very small. The ratios of the number of electrons in C-H and C-C bonds for hexane and decane are 28/10 and 44/18 respectively, therefore,

$$N(\text{Hexane}) = \frac{1}{38}\left[28\ N(C\text{-}H) + 10\ N(C\text{-}C)\right],$$

$$N(\text{Decane}) = \frac{1}{62}\left[44\ N(C\text{-}H) + 18\ N(C\text{-}C)\right].$$

The computed and experimental momentum distributions for methane, hexane, and decane are shown in Figures 3.2, 3.3, and 3.4 respectively. The calculated N(C-H) of Duncanson and Coulson[35] is also shown in Figure 3.2 for comparison.

3.4 Discussion

We assume that, prior to annihilating, the positron acquires an energy of ~0.1 ev. Calculations have been made to estimate the thermalization time of positrons in metals.[40,41] But no rigorous calculation has been made to predict the thermalization time in non-metal or liquids. An experimental attempt to examine the question[42] was inconclusive. The calculations and experiments described in this Chapter are based on the assumption that the energy of the positron is near thermal and that all the momentum assigned to the annihilating pair comes from the electron. This is consistent with the general overall agreement between the calculated N(p) curves and the experimental curves presented in this Chapter.

The experimental curves for N(p) consist of a low momentum part and a high momentum component. The low

momentum component which is primarily due to the annihilation of singlet positronium can be fitted to a gaussian. It was seen in Chapter 1 that the percentage of singlet positronium formed is $I_2/3$ where I_2, the amount of triplet positronium formed, is obtained from the time spectra measurements. Thus, if the low momentum component in the momentum distribution does arise from the annihilation of singlet positronium, its intensity, which we shall call I_L, should be equal to $I_2/3$. It has been shown[38] that for several organic liquids the I_L obtained from the momentum distributions are consistent with the $I_2/3$ obtained from lifetime measurement. This supports the view that the low momentum component is due to the self annihilation of singlet positronium. The high momentum component arises then from the annihilation of electrons bound to the molecule with free positrons and the positrons of triplet positronium.

The calculated curves fit well with experimental curves except in the higher momentum region. If the higher values predicted by the calculation represent a real effect in this region, then several points need discussing.

First, if thermalization of the positron had not occourred by the time the electron and positron annihilated, then one would expect the experimental curve to lie above the calculated curves in those figures in the high momentum region. This is not the case and supports the view that positron had a low momentum contribution to make to the pair.

Secondly, the positron wave function used in the calculations in this chapter is a plane wave which takes on the value of a constant for small positron momentum. This could be sensibly modified to include the interaction of positron and the atomic nucleus by reducing the positron wave function in the regions of space near the nucleus. This would correspond to a reduction in magnitude of the product of the positron and electron wave functions for high electron momentum. This kind of modification will be discussed in the next chapter.

FIGURE 3.1

Calculated Electron Momentum Distributions

For C-H and C-C Bonds

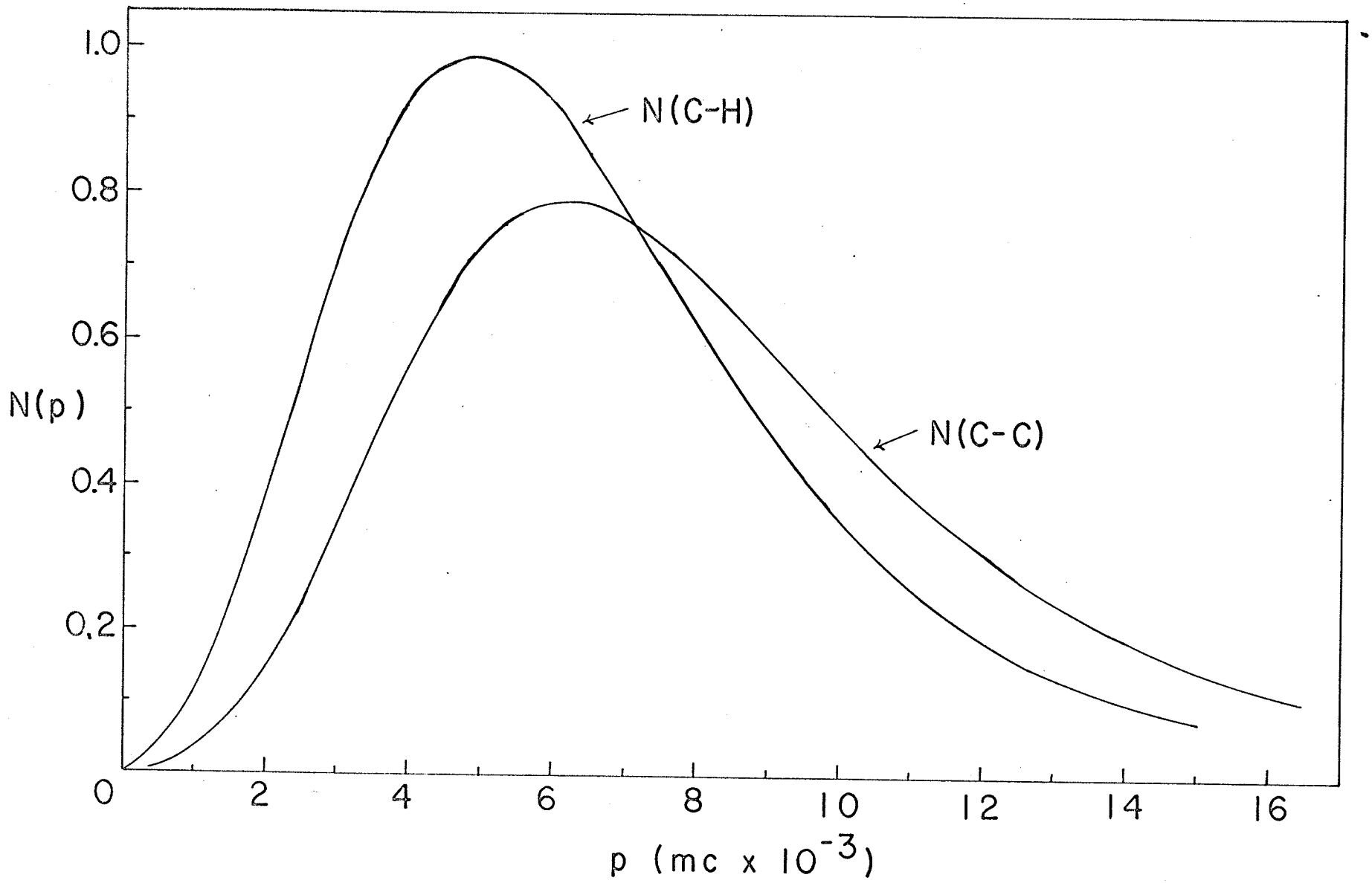
1.0
0.8
0.6
0.4
0.2
0
N(p)
N(C-H)
N(C-C)
2
4
6
8
10
12
14
16
p (mc x 10^-3)

FIGURE 3.2

The Momentum Distribution for Methane

 -----The experimental points for liquid methane ($-177^{\circ}C$)

 ----- " " solid methane ($-187^{\circ}C$)

A ------- The theoretical curve (with $\psi_+(r) = 1$)

B -------The calculated result of Duncanson and Coulson.

$N(P_s)$----A Gaussian to fit the low momentum component of the liquid methane.

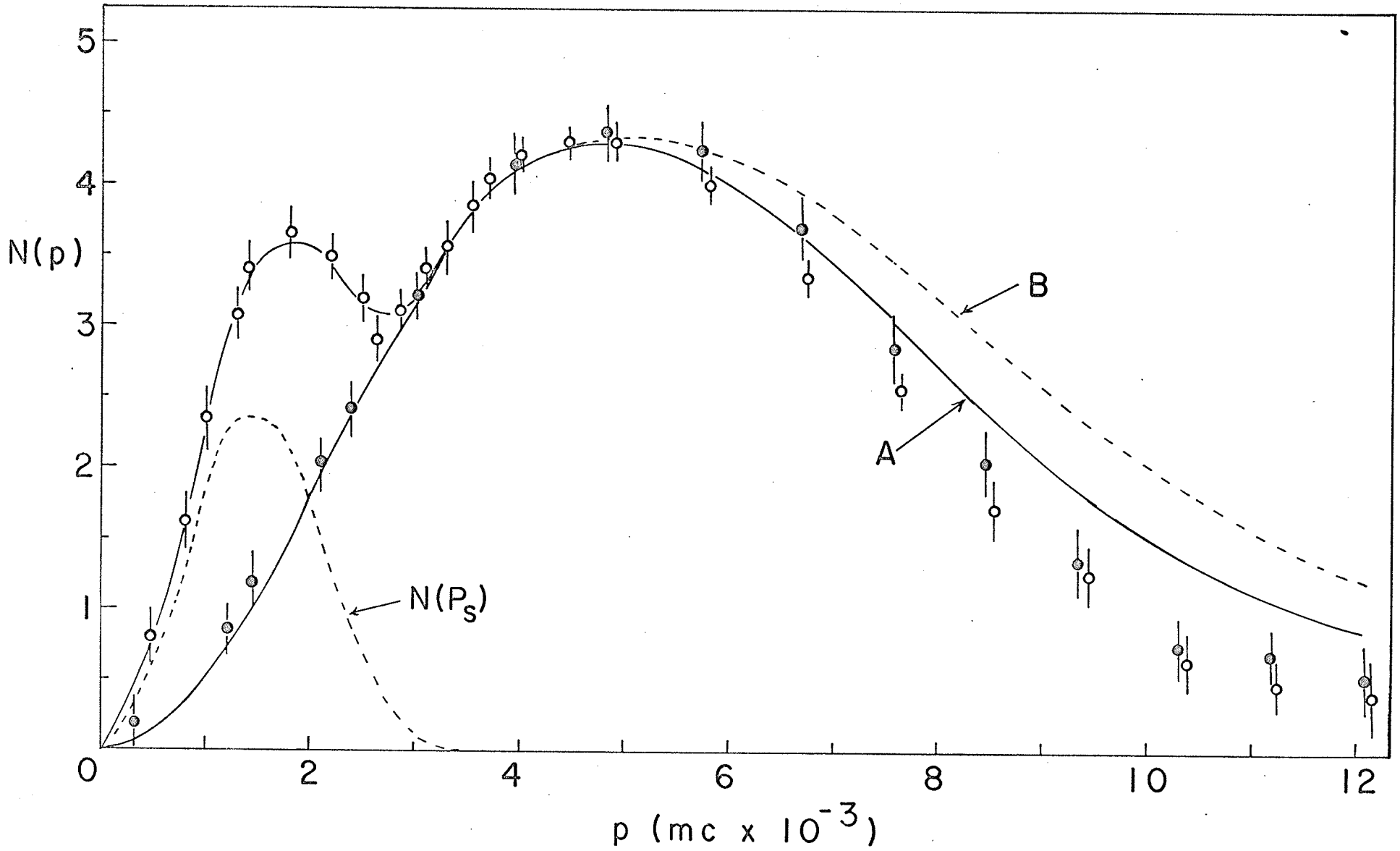
N(p)
5
4
3
2
1
0
2
4
6
8
10
12
p (mc x 10^-3)
B
A
N(P_S)

FIGURE 3.3

The Momentum Distribution for Hexane

The open circles are the experimental points, and the solid line indicates the theoretical curve which is the combination of curves A, B and C.

A ---- $N(P_s)$ (Gaussian).

B ---- $\frac{28}{38}$ N(C-H)

C ---- $\frac{10}{38}$ N(C-C)

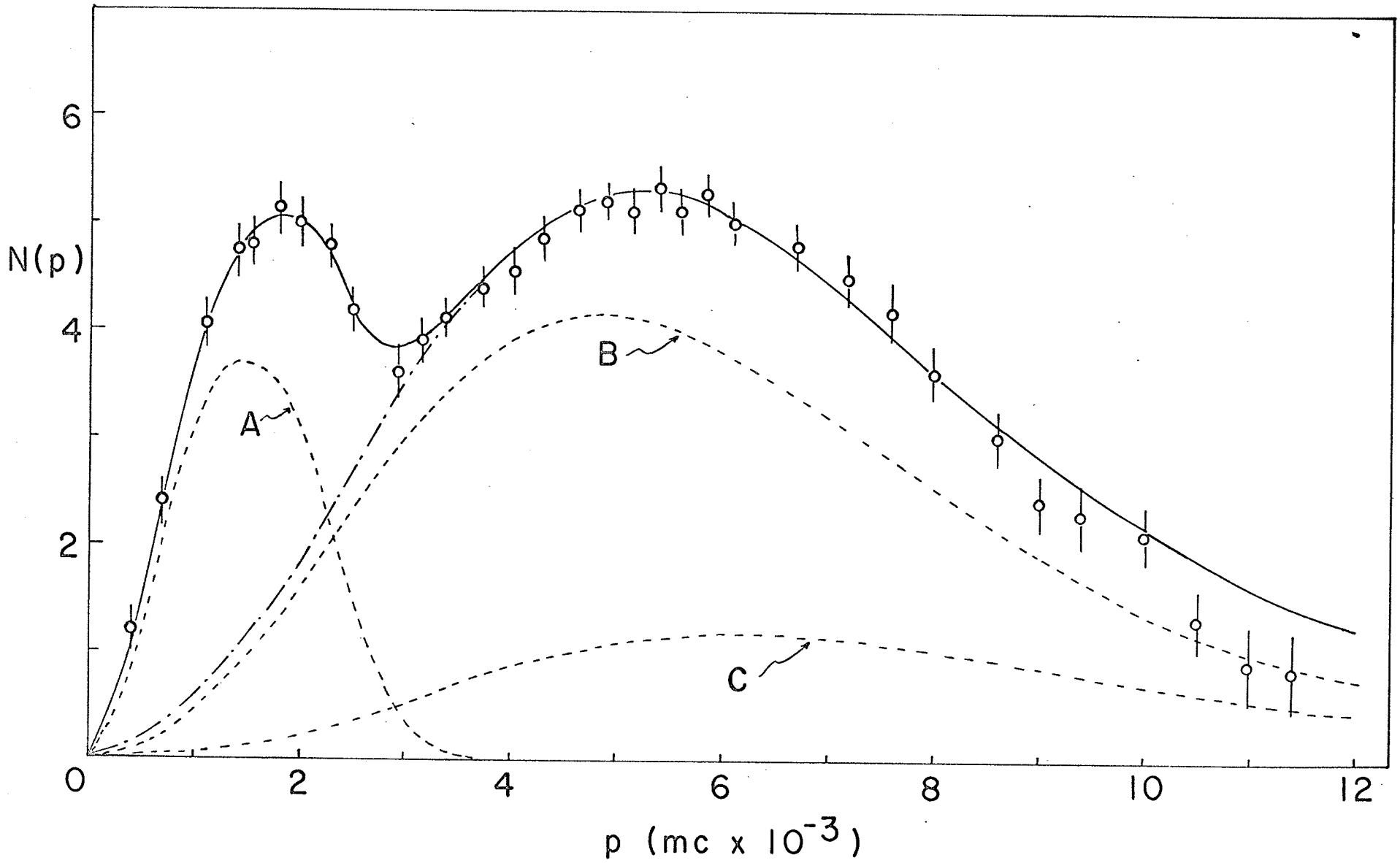
N(p)
6
4
2
0
2
4
6
8
10
12
A
B
C
p (mc x 10^-3)

FIGURE 3.4

The Momentum Distribution for Decane

The open circles are the experimental points, and the solid line indicates the theoretical curve which is the combination of curves A, B and C.

A ---- $N(P_S)$ (Gaussian).

B ---- $\frac{22}{31} N(C\text{-}H)$.

C ---- $\frac{9}{31} N(C\text{-}C)$.

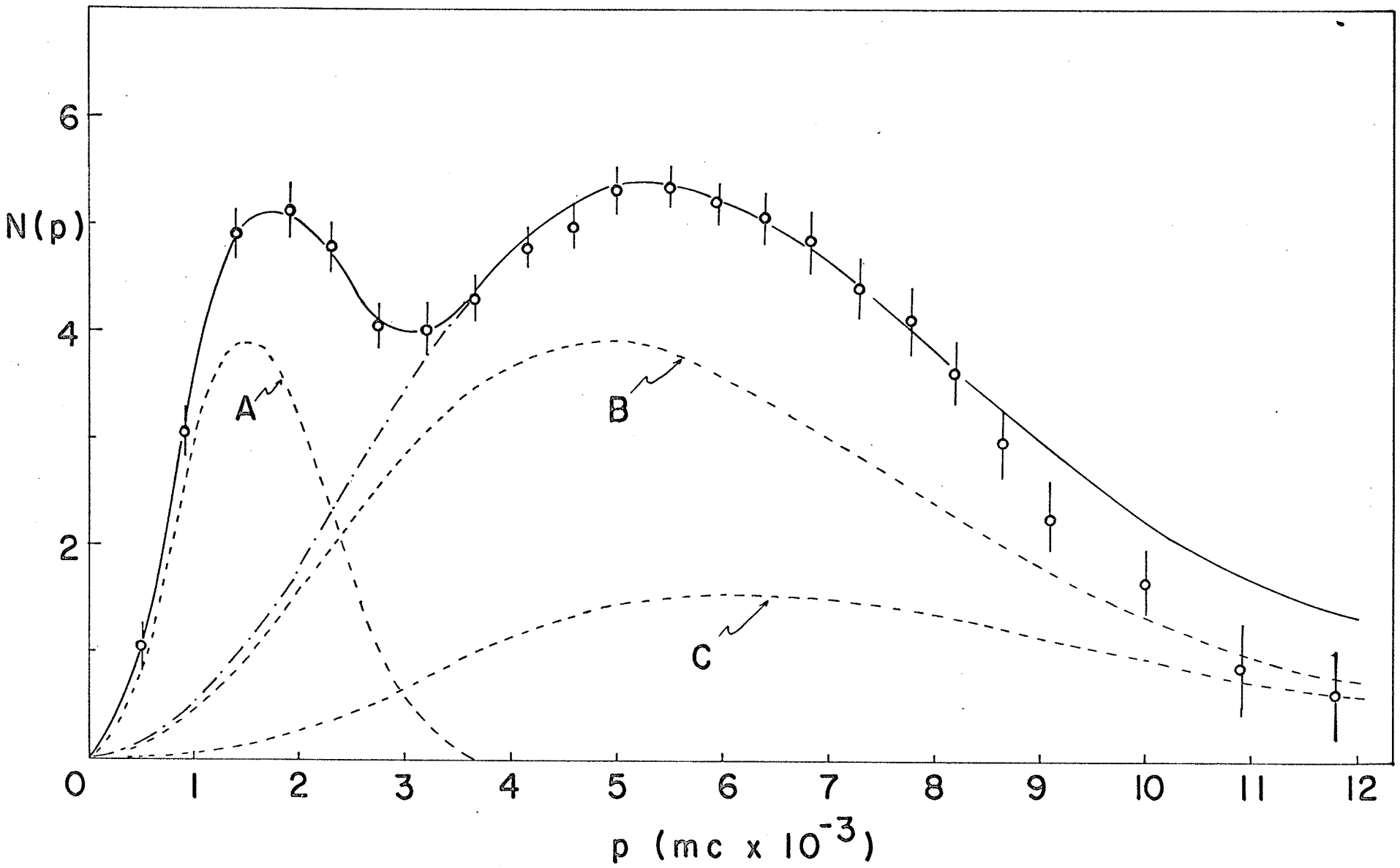
N(p)
6
4
2
0
1
2
3
4
5
6
7
8
9
10
11
12
A
B
C
p (mc x 10^-3)

Chapter 4

Positron Annihilation in Normal Hydrocarbon Systems. II. One-parameter Analytic Positron Wave Function

4.1 Form of Positron Wave Function

In Chapter 3, we have discussed the discrepancy between theoretical and experimental curves in the higher momentum region and stated that it was probably due to the use of a constant positron wave function in the calculations. In an attempt to explain the discrepancy, we introduce a one-parameter positron wave function of the form

$$(4\text{-}1) \quad \psi_+(r) = 1 - \exp(-m_i r) \ ,$$

where m_i is a parameter corresponding to the i^{th} atom, and the origin of r is at the center of the i^{th} atom. Since the SCF electron wave functions are linear combinations of exponentials, this analytic form for $\psi_+(r)$ is convenient for momentum distribution calculations. When m_i is large, e.g., ~ 10, $\psi_+(r) \simeq 1$. This is the case of a plane wave type with small positron momentum. $\psi_+(r)$ also satisfies the following conditions:

$$\psi_+(r) = 0 \quad \text{when } r \to 0;$$

and $$\psi_+(r) = 1, \quad \psi_+(r)' = 0 \quad \text{when } r \to \infty.$$

4.2 Calculations of Momentum Distributions of Annihilating Positron Electron Pairs

From equation (3-11), the momentum wave function for an annihilating positron-electron pair has the form

$$(4\text{-}2) \qquad \chi(\vec{p}) = (2\pi)^{-3/2} \int \exp(-i\vec{p}\cdot\vec{r})\, \psi_-(\vec{r})\, \psi_+(\vec{r})\, d\vec{r}$$

where $\psi_-(\vec{r})$ and $\psi_+(\vec{r})$ are the electron and the positron wave functions respectively. Substituting equation (4-1) into the above equation, we get

$$(4\text{-}2') \qquad \chi(\vec{p}) = \chi'(\vec{p}) - \chi''(\vec{p}),$$

where

$$(4\text{-}3) \qquad \chi'(\vec{p}) = (2\pi)^{-3/2} \int \exp(-i\vec{p}\cdot\vec{r})\, \psi_-(\vec{r})\, d\vec{r}, \qquad \text{and}$$

$$(4\text{-}4) \qquad \chi''(\vec{p}) = (2\pi)^{-3/2} \int \exp(-i\vec{p}\cdot\vec{r})\, \psi_-(\vec{r}) \exp(-m_i r)\, d\vec{r}.$$

The momentum distribution function for an annihilating positron-electron pair then becomes

$$(4\text{-}5) \qquad N(p) = \int_0^{\pi} \chi(\vec{p})^* \chi(\vec{p}) \cdot 2\pi p^2 \sin\Theta \, d\Theta$$

$$= \int_0^{\pi} \left[\chi'(\vec{p}) - \chi''(\vec{p})\right]^* \left[\chi'(\vec{p}) - \chi''(\vec{p})\right] 2\pi p^2 \sin\Theta \, d\Theta .$$

Now the momentum distribution function in the hybrid carbon orbitals is

$$(4\text{-}6)\qquad N_C(p)=\int_0^{\pi}\left[\chi'_C(\vec{p})-\chi''_C(\vec{p})\right]^*\left[\chi'_C(\vec{p})-\chi''_C(\vec{p})\right]2\pi p^2\sin\Theta\, d\Theta,$$

where $\chi'_C(\vec{p})$ is given in equation (3-4"), i.e.,

$$\chi'_C(\vec{p})=\frac{\sqrt{2}}{\pi\sqrt{1+\sigma^2}}\sum_k\left[A_k\frac{a_k}{(a_k^2+p^2)^2}-B_k\frac{(3b_k^2-p^2)}{(b_k^2+p^2)^3}\right]$$

$$+i\frac{\sqrt{6}}{\pi\sqrt{1+\sigma^2}}\cos\Theta\sum_k C_k\left[\frac{c_k(c_k^2-3p^2)}{p(c_k^2+p^2)^3}-\frac{c_k}{p(c_k^2+p^2)^2}\right]$$

and

$$\chi''_C(\vec{p})=\frac{2}{\pi\sqrt{1+\sigma^2}}\sum_k\left\{A_k\frac{a_k+m_c}{\left[(a_k+m_c)^2+p^2\right]^2}-B_k\frac{3(b_k+m_c)^2-p^2}{\left[(b_k+m_c)^2+p^2\right]^3}\right\}$$

$$+i\frac{\sqrt{6}\,\sigma}{\pi\sqrt{1+\sigma^2}}\sum_k C_k\left\{\frac{(c_k+m_c)\left[(c_k+m_c)^2-3p^2\right]}{p\left[(c_k+m_c)^2+p^2\right]^3}-\frac{c_k+m_c}{p\left[(c_k+m_c)^2+p^2\right]^2}\right\}\cos\Theta,$$

and the coefficents A_k, B_k, C_k,...etc. are given in Table 3.1. After the integration in equation (4-6), we get

$$(4\text{-}6')\qquad N_C(p)=\frac{8p^2}{\pi(1+\sigma^2)}\left\{\sum_k\left[A_k\frac{a_k}{(a_k^2+p^2)^2}-B_k\frac{3b_k^2-p^2}{(b_k^2+p^2)^3}\right]\right.$$

$$- \sum_k \left[A_k \frac{a_k + m_c}{\left[(a_k+m_c)^2 + p^2\right]^2} - B_k \frac{3(b_k+m_c)^2 - p^2}{\left[(b_k+m_c)^2+p^2\right]^3} \right] \Bigg\}$$

$$+ \frac{8p^2}{\pi(1+\sigma^2)} \Bigg\{ \sum_k C_k \left[\frac{c_k(c_k^2-3p^2)}{p(c_k^2+p^2)^3} - \frac{c_k}{p(c_k^2+p^2)^2} \right]$$

$$- \sum_k C_k \left[\frac{(c_k+m_c)\left[(c_k+m_c)^2-3p^2\right]}{p\left[(c_k+m_c)^2+p^2\right]^3} - \frac{c_k+m_c}{p\left[(c_k+m_c)^2+p^2\right]^2} \right] \Bigg\} .$$

Similarly, the momentum distribution in the hydrogen 1s orbital becomes

$$(4\text{-}7) \qquad N_H(p) = \int_o^{\pi} \left[\chi'_H(\vec{p}) - \chi''_H(\vec{p})\right]^* \left[\chi'_H(\vec{p}) - \chi''_H(\vec{p})\right] 2\pi p^2 \cdot \sin\Theta \, d\Theta$$

$$= 4\pi p^2 \left[\chi'_H(\vec{p}) - \chi''_H(\vec{p})\right]^2$$

$$= \frac{32p^2}{\pi} \left\{ \frac{1}{(1+p^2)^2} - \frac{1+m_h}{\left[(1+m_h)^2+p^2\right]^2} \right\}^2 .$$

From equation (3-8), the momentum distribution in the C-H bond, N(C-H), can be written as

$$(4\text{-}8) \qquad N(C\text{-}H) = \frac{1}{2(1+S_{CH}^2)} \left[N_C(p) + N_H(p) + 2S_{CH} N_{ch}(p) \right] ,$$

now $N_C(p)$ and $N_H(p)$ are given in equation (4-6') and (4-7) respectively, and

$$N_{ch}(p) = \int_o^{\pi} \left[\chi_C(\vec{p})\chi_H(\vec{p})^* \exp(-i\vec{p}\cdot\vec{R}_{CH}) + \chi_C(\vec{p})^*\chi_H(\vec{p})\exp(i\vec{p}\cdot\vec{R}_{CH})\right] 2\pi p^2 \sin\Theta\, d\Theta$$

$$= \frac{16p}{\pi R_{CH}(1+\sigma^2)^{\frac{1}{2}}} \left[\frac{1}{(1+p^2)^2} - \frac{1+m_h}{\left[(1+m_h)^2+p^2\right]^2}\right]$$

$$\times \left\{\left[\sum_k \left(A_k \frac{a_k}{(a_k^2+p^2)^2} - B_k \frac{(3b_k^2-p^2)}{(b_k^2+p^2)^3}\right)\right.\right.$$

$$\left. - \sum_k \left(A_k \frac{(a_k+m_c)}{\left[(a_k+m_c)^2+p^2\right]^2} - B_k \frac{3(b_k+m_c)^2-p^2}{\left[(b_k+m_c)^2+p^2\right]^3}\right)\right] \sin(pR_{CH})$$

$$+\sqrt{3}\,\sigma \left[\sum_k C_k \left(\frac{c_k(c_k^2-3p^2)}{p(c_k^2+p^2)^3} - \frac{c_k}{p(c_k^2+p^2)^2}\right)\right.$$

$$\left. - \sum_k C_k \left(\frac{(c_k+m_c)\left[(c_k+m_c)^2-3p^2\right]}{p\left[(c_k+m_c)^2+p^2\right]^3} - \frac{c_k+m_c}{p\left[(c_k+m_c)^2+p^2\right]^2}\right)\right]$$

$$\times \left[\cos(pR_{CH}) - \frac{\sin(pR_{CH})}{pR_{CH}}\right]\Bigg\}.$$

Similarly, from equation (3-10), the momentum distribution in the C-C bond can be written as

$$(4\text{-}9) \qquad N(C\text{-}C) = \frac{1}{1+S_{ab}^2}\left[N_C(p) + S_{ab}N_{ab}(p)\right]$$

where $N_C(p)$ is now given in equation (4-6'), and

$$N_{ab}(p) = \int_0^{\pi} \chi_C(p)^* \chi_C(p) \cos(pR_{CC}\cos\Theta)\, 2\pi p^2 \sin\Theta\, d\Theta$$

$$= \frac{8p^2}{\pi(1+\sigma^2)}\left\{\left|\sum_k\left[A_k \frac{a_k}{(a_k^2+p^2)^2} - B_k \frac{(3b_k^2-p^2)}{(b_k^2+p^2)^3}\right]\right.\right.$$

$$\left.\left. - \sum_k\left[A_k \frac{a_k+m_c}{[(a_k+m_c)^2+p^2]^2} - B_k \frac{3(b_k+m_c)^2-p^2}{[(b_k+m_c)^2+p^2]^3}\right]\right|^2 \cdot \frac{\sin(pR_{CC})}{pR_{CC}}\right.$$

$$+3\sigma^2\left|\sum_k C_k\left[\frac{c_k}{p(c_k^2+p^2)^2} - \frac{c_k(c_k^2-3p^2)}{p(c_k^2+p^2)^3}\right]\right.$$

$$\left. - \sum_k C_k\left[\frac{c_k+m_c}{p[(c_k+m_c)^2+p^2]^2} - \frac{(c_k+m_c)[(c_k+m_c)^2-3p^2]}{p[(c_k+m_c)^2+p^2]^3}\right]\right|^2$$

$$\left. \times \left[\frac{\sin(pR_{CC})}{pR_{CC}} + \frac{2\cos(pR_{CC})}{(pR_{CC})^2} - \frac{2\sin(pR_{CC})}{(pR_{CC})^3}\right]\right\}.$$

Momentum distributions N(C-H) and N(C-C) were computed for different values of m_h and m_c, the parameter in the positron wave functions corresponding to the hydrogen atom and the carbon atom.

4.3 Results and Discussion

Figure 4.1 shows the calculated and experimental results for the methane molecule, with $m_h = m_c = 1.4$. (The calculated curves with $m_h = 1.3 \pm 0.3$ and $m_c = 1.4 \pm 0.3$, all fit with experimental data to within the experimental uncertainty.) Similar results for hexane and decane are shown in Figures 4.2 and 4.3.

In all cases, the calculated N(p) curves are in good agreement with the experimental curves. The discrepancy presented in the last Chapter now has been removed by using such a simple-minded positron wave function. This suggests that in detailed analyses of momentum distributions one must consider the Coulomb interaction of the positron with the effective nuclear charge.

FIGURE 4.1

The Momentum Distribution for Methane

The solid line indicates the calculated curve using the one-parameter analytic positron wave function, with parameters $m_h = m_c = 1.4$.

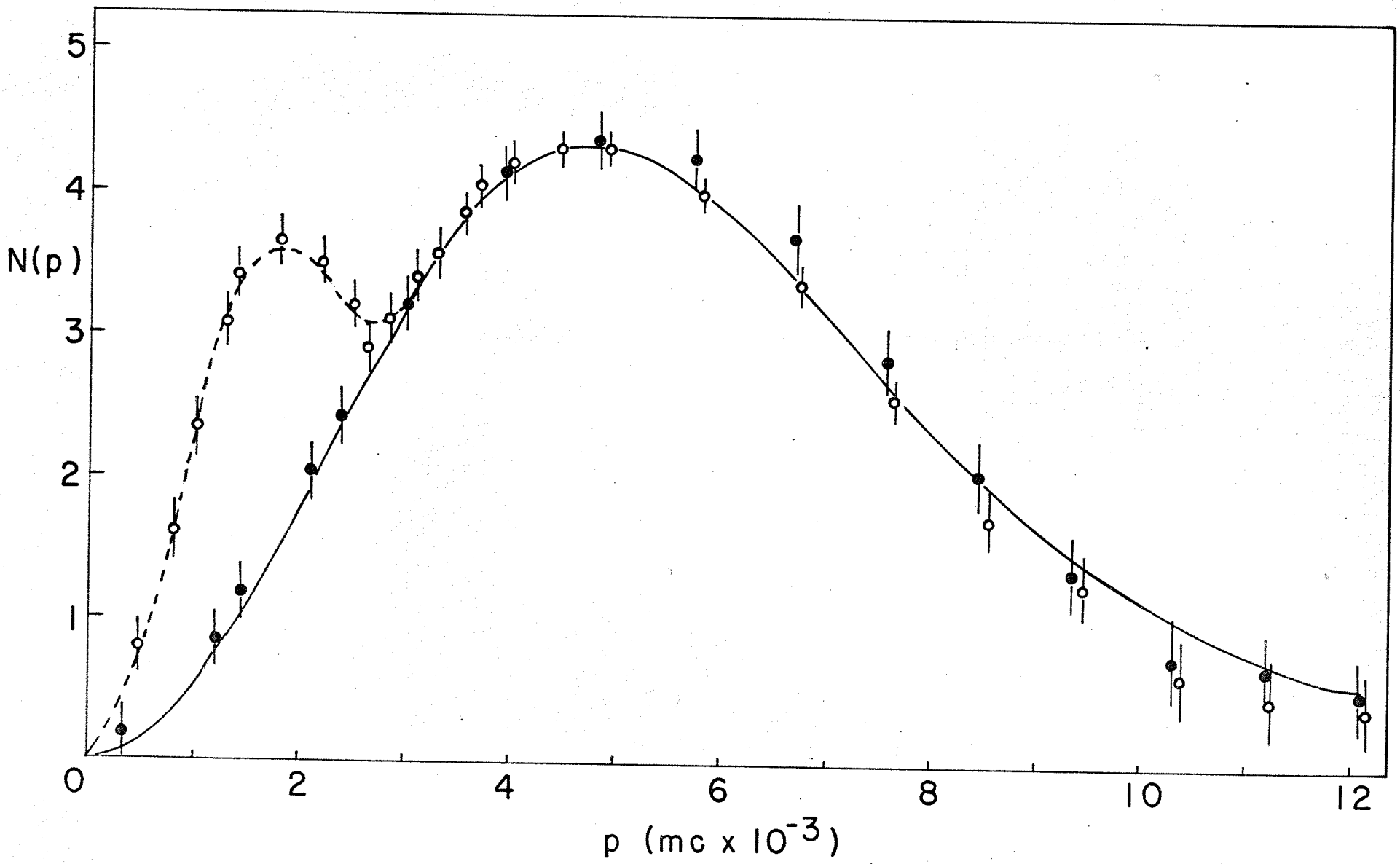
N(p)
5
4
3
2
1
0
2
4
6
8
10
12
p (mc x 10^-3)

FIGURE 4.2

The Momentum Distribution for Hexane

The solid line indicates the calculated curve with $m_h = m_c = 1.4$.

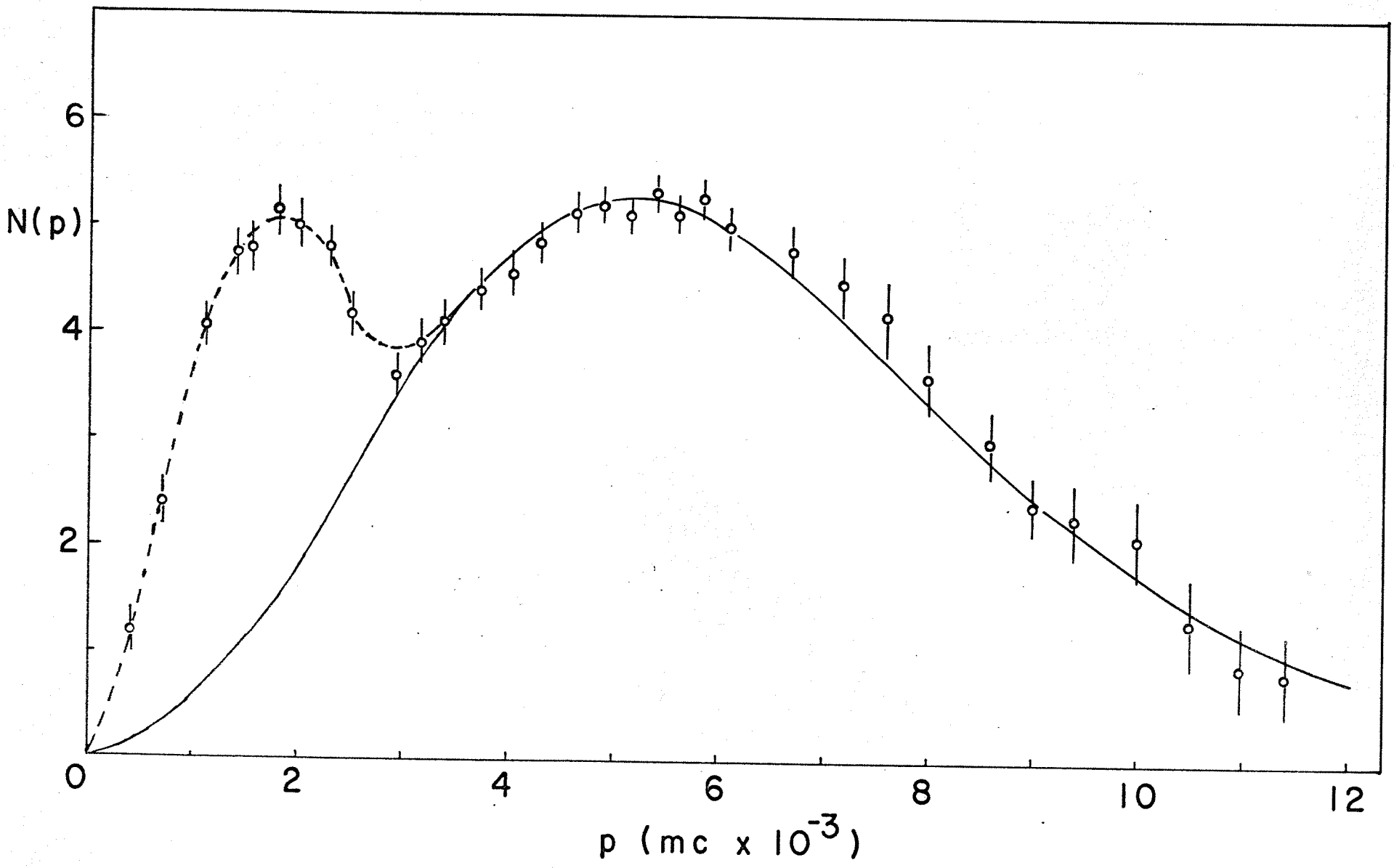
N(p)
6
4
2
0
2
4
6
8
10
12
p (mc x 10^-3)

FIGURE 4.3

The Momentum Distribution for Decane

The solid line indicates the calculated curve with $m_h = m_c = 1.4$.

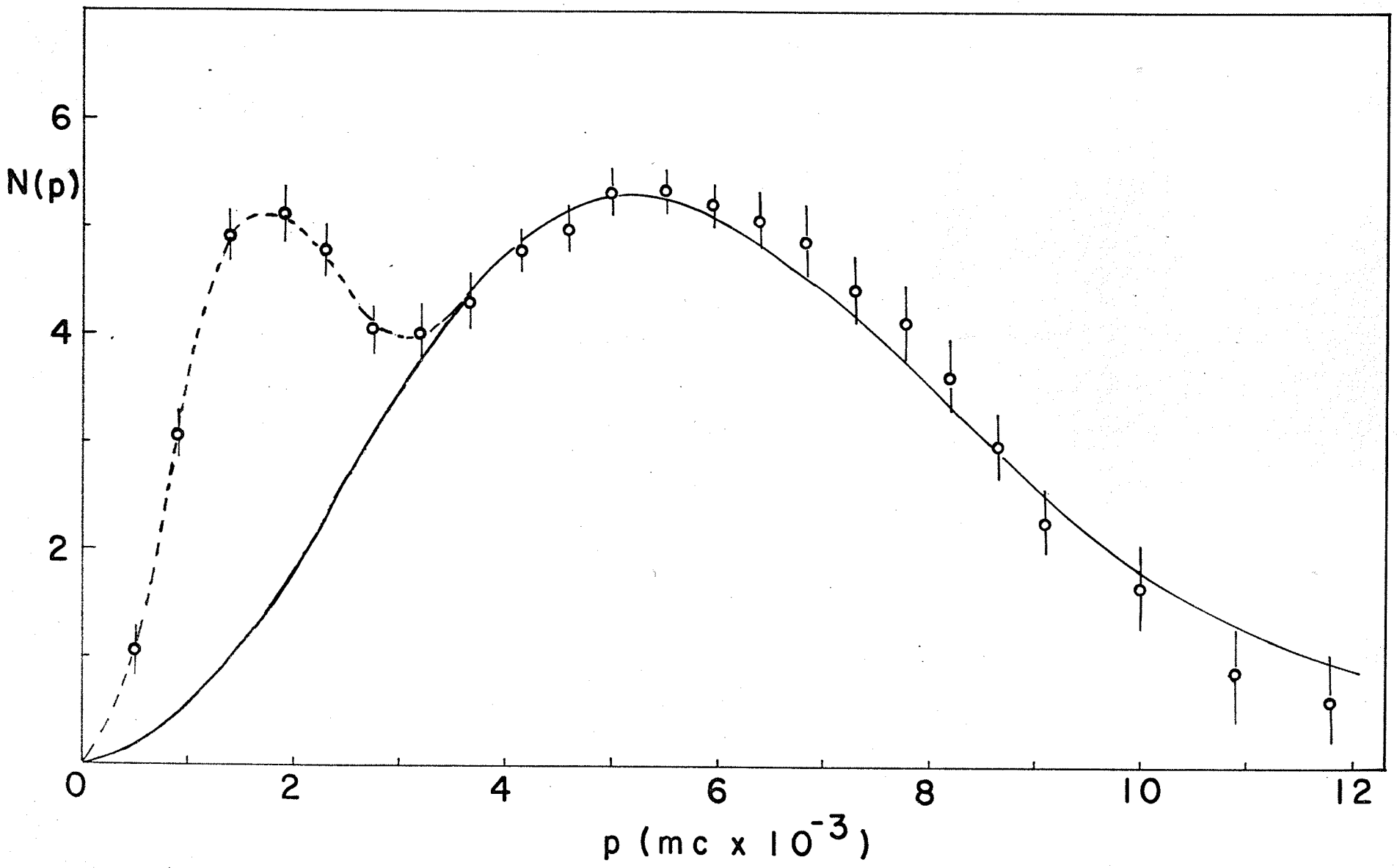
N(p)
6
4
2
0
2
4
6
8
10
12
p (mc x 10^-3)

Chapter 5

Positron Annihilation in Normal Hydrocarbon Systems. III. Positron Wave Function Obtained From Schrödinger Equation

5.1 Calculations of Positron Wave Functions

In Chapter 4 we introduced a simple form for the positron wave function and showed how this form leads to reasonable results. We will now show how a more realistic positron wave function may be obtained as a solution to the ground state radial Schrödinger equation.

Since electron wave functions for the molecule have been constructed from combinations of atomic orbitals, we will calculate the positron wave functions corresponding to the individual atomic potentials. The electron-positron wave function product for the molecule will then be combinations of products for the individual atoms.

Recently, the thermal motion of positrons in metals have been observed by Stewart et el.[50,51] However, the effect of thermal momentum of the positron on the experimental data would be small. We will neglect the thermal momentum of the positron in this calculation. The positron-electron correlation is also ignored.

Now we will first consider the interaction between a positron and a carbon atom. The positron wave function, $\psi_+(r)$, is the ground state solution of the Schrödinger equation, i.e.,

$$(5\text{-}1) \qquad -\tfrac{1}{2}\nabla^2\psi_+(r) + V_c(r)\psi_+(r) = E\psi_+(r),$$

in which the potential $V_c(r)$ is taken to be that of a neutral carbon atom calculated by Herman and Skillman[52] (but with a positive sign). $V_c(r)$ is shown in Figure 5.1. The eigenvalue E is chosen to satisfy the boundary condition that the slope of the wave function vanish on the boundary surface of the atom, i.e.,

$$\psi_+(r)' = 0 \quad \text{at } r = r_c ,$$

in which r_c is taken to be the average radius of the carbon atom, i.e., $r_c = \langle\psi(C)|r|\psi(C)\rangle = 1.54$ a.u. The wave function for $r > r_c$ is taken to be unity. Thus $\psi_+(r_c) = 1$ is another boundary condition for equation (5-1).

If we set $R_+(r) = r\psi_+(r)$, then equation (5-1) becomes a second order differential equation with first derivative missing, i.e.,

$$(5\text{-}2) \qquad R_+(r)'' + 2\left[E - V_c(r)\right]R_+(r) = 0.$$

This equation was solved numerically by a familiar method.[53] The result is shown in Figure 5.1.

Now we will consider the potential of hydrogen atom seen by the positron. This potential has a form

$$(5\text{-}3) \qquad V_h(r) = \frac{1}{r} - \frac{1}{r}\int_0^r |\psi(H)|^2 \cdot 4\pi r^2 dr,$$

FIGURE 5.1

The Potential of the Carbon Atom and the Corresponding Positron Wave Function

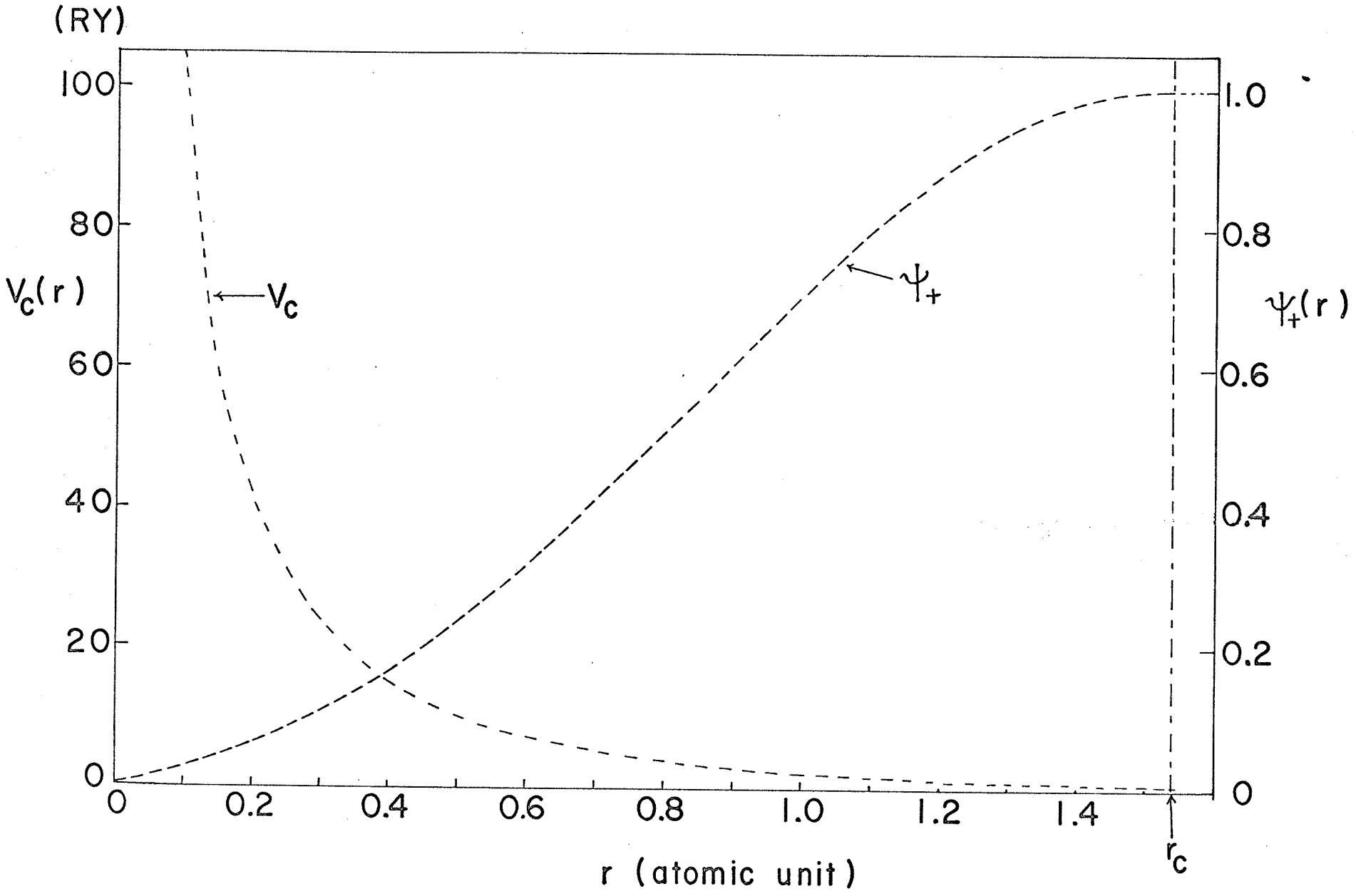
(RY)
100
80
60
40
20
0
$V_c(r)$
V_c
ψ_+
$\psi_+(r)$
1.0
0.8
0.6
0.4
0.2
0
0
0.2
0.4
0.6
0.8
1.0
1.2
1.4
r_c
r (atomic unit)

FIGURE 5.2

The Potential of the Hydrogen Atom and the Corresponding Positron Wave Function

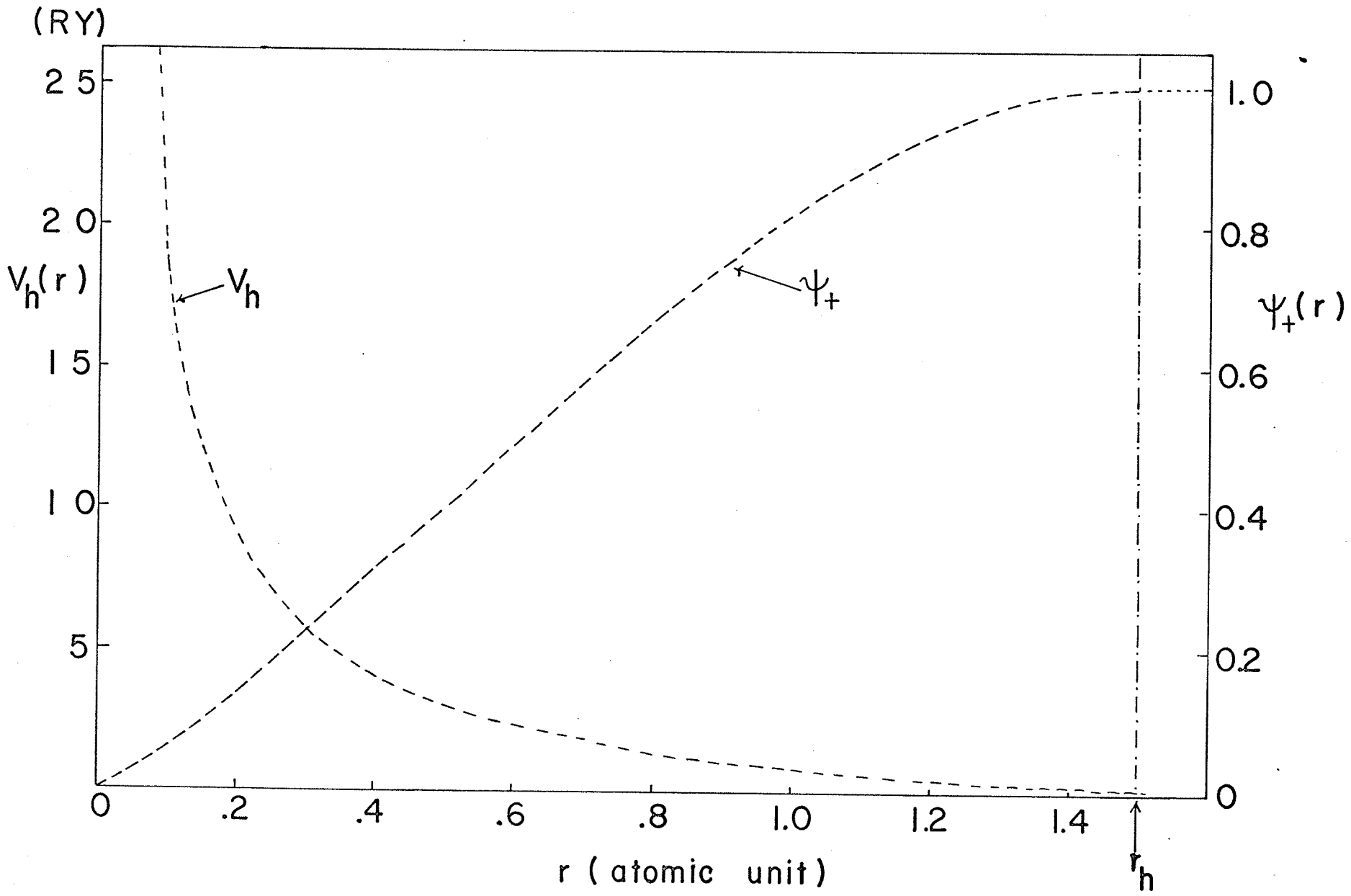
(RY)
25
20
15
10
5
$V_h(r)$
V_h
ψ_+
$\psi_+(r)$
1.0
0.8
0.6
0.4
0.2
0
0
.2
.4
.6
.8
1.0
1.2
1.4
r (atomic unit)
r_h

where the first term is the coulomb repulsion of the nucleus, and the second term is due to the charge distribution of the 1s electron. Now $\psi_{1s}(H) = \pi^{-\frac{1}{2}} \exp(-r)$, and equation (5-3) is then

$$V_h(r) = \frac{1}{r} - \frac{4}{r}\int_0^r r^2 \exp(-2r)dr$$

$$= (2r + 2 + 1/r)\exp(-2r),$$ which is shown in Figure 5.2, so that equation (5-2) becomes

$$(5\text{-}4) \qquad R_+(r)'' + 2\left[E - V_h(r)\right]R_+(r) = 0$$

or $$R_+(r)'' + 2\left[E - (2r + 2 + 1/r)\exp(-2r)\right]R_+(r) = 0.$$

Again E is chosen to fit the boundary condition $\left[R_+(r)/r\right]' = 0$ at $r = r_h$, the average radius of hydrogen, i.e., $r_h = \langle\psi(H)|r|\psi(H)\rangle = 1.50$ a.u. This numerical positron wave function is also shown in Figure 5.2. IBM Fortran IV computer programs are included in Appendix D.

5.2 Calculations of Momentum Distributions of Annihilating Positron Electron Pairs

A. The Momentum Distribution in the Hybrid Carbon Orbital

The electron wave function for the hybrid carbon orbital is given in equation (3-1), i.e.,

$$\psi(C) = \frac{\psi_{2s}(C) + \sigma\psi_{2p}(C)}{\sqrt{1+\sigma^2}} \quad .$$

The momentum wave function for an annihilating pair is then,

$$\chi_C(\vec{p}) = (2\pi)^{-3/2} \int \exp(-i\vec{p}\cdot\vec{r})\psi(C)\psi_+(r)d\vec{r}$$

$$= \frac{1}{(2\pi)^{3/2}\sqrt{1+\sigma^2}} \left\{ \int \exp(-i\vec{p}\cdot\vec{r})\psi_{2s}(C)\psi_+(r)d\vec{r} \right.$$

$$\left. + \sigma \int \exp(-\vec{p}\cdot\vec{r})\psi_{2p}(C)\psi_+(r)d\vec{r} \right\} \quad .$$

Following the same calculation of equation (3-4'), we get

$$(5\text{-}5) \quad \chi_C(\vec{p}) = (2\pi)^{-3/2}(1+\sigma^2)^{-\frac{1}{2}} \left\{ (4\pi)^{\frac{1}{2}} \int_0^\infty j_0(pr)R_{2s}(C)\psi_+(r)r^2dr \right.$$

$$\left. - i\sigma\cos\Theta \cdot 2(3\pi)^{\frac{1}{2}} \int_0^\infty j_1(pr)R_{2p}(C)\psi_+(r)r^2dr \right\} \quad .$$

where $R_{2s}(C)$ and $R_{2p}(C)$ are 2s and 2p radial wave functions of carbon. $j_0(pr)$ and $j_1(pr)$ are spherical Bessel functions.

Then the momentum distribution function $N_C(p)$ is

$$(5\text{-}6) \quad N_C(p) = \int_0^\pi \chi_C(\vec{p})^* \chi_C(\vec{p}) 2\pi p^2 \sin\Theta \, d\Theta$$

$$= \frac{2p^2}{\pi(1+\sigma^2)} \left\{ X_1(p)^2 + \sigma^2 X_2(p)^2 \right\}$$

where

$$(5\text{-}7) \qquad X_1(p) = \int_0^\infty j_0(pr) R_{2s}(C) \psi_+(r) r^2 dr,$$

$$(5\text{-}8) \qquad X_2(p) = \int_0^\infty j_1(pr) R_{2p}(C) \psi_+(r) r^2 dr.$$

B. The Momentum Distribution in the Hydrogen 1s Orbital

Similarly, the momentum distribution in the hydrogen 1s orbital becomes

$$(5\text{-}9) \qquad N_H(p) = \int_0^\pi \chi_H(\vec{p})^* \chi_H(\vec{p}) 2\pi p^2 \sin\Theta \, d\Theta$$

$$= 4\pi p^2 \left| \chi_H(\vec{p}) \right|^2 ,$$

where

$$(5\text{-}10) \qquad \chi_H(\vec{p}) = (2\pi)^{-3/2} \int \exp(-i\vec{p}\cdot\vec{r}) \psi(H) \psi_+(r) d\vec{r}$$

$$= \frac{\sqrt{2}}{\pi} \int_0^\infty j_0(pr) \exp(-r) \psi_+(r) r^2 dr \ .$$

C. The Momentum Distribution in the C-H Bond

To calculate the momentum distribution of the photon pairs due to positrons annihilating with electrons in the C-H bond, we first transform the Fourier component of the positron wave function overlapping with number 1 electron

as we did in Chapter 3, i.e.,

$$\chi(\vec{p}_1,\vec{r}_2)= (2\pi)^{-3/2} \int \exp(-i\vec{p}_1\cdot\vec{r}_1)\psi(C\text{-}H)\,\psi_+(r_1)d\vec{r}_1,$$

then we average $\chi(\vec{p}_1,\vec{r}_2)^*\chi(\vec{p}_1,\vec{r}_2)$ over all positions of the number 2 electron, i.e.,

$$\chi(\vec{p}_1)^*\chi(\vec{p}_1)=\int\chi(\vec{p}_1,\vec{r}_2)^*\chi(\vec{p}_1,\vec{r}_2)dv_2 \ .$$

Then adopting the result in Section 3.2C, the momentum distribution, N(C-H), is

$$(5\text{-}11)\qquad N(C\text{-}H)=\int_o^\pi \chi(\vec{p})^*\chi(\vec{p})2\pi p^2\sin\Theta\, d\Theta$$

$$= \frac{1}{2(1+S_{CH}^2)}\left\{N_C(p)+N_H(p)+2S_{CH}N_{ch}(p)\right\}$$

where $N_C(p)$ and $N_H(p)$ are now given in equations (5-6) and (5-9) respectively, and

$$N_{ch}(p)=\int_o^\pi \chi_H(p)\frac{1}{\sqrt{2}\,\pi\sqrt{1+6^2}}\,X_1(p)\cos(pR_{CH}\cos\Theta)2\pi p^2\sin\Theta\, d\Theta$$

$$+\int_o^\pi \chi_H(p)\frac{3}{\sqrt{2}\,\pi\sqrt{1+6^2}}\cos\Theta\, X_2(p)\sin(pR_{CH}\cos\Theta)2\pi p^2\sin\Theta\, d\Theta$$

$$=\frac{2\sqrt{2}\ p}{R_{CH}\sqrt{1+6^2}}\,\chi_H(p)\left\{X_1(p)\sin(pR_{CH})+\sqrt{3}\,6\,X_2(p)\left[\frac{\sin(pR_{CH})}{pR_{CH}}-\cos(pR_{CH})\right]\right\}$$

in which $X_1(p)$, $X_2(p)$ and $\chi_H(p)$ are given in equations (5-7), (5-8) and (5-10) respectively.

D. The Momentum Distribution in the C-C Bond

Similarly, adopting the result in Section 3.2D, the momentum distribution of annihilating pairs in the C-C bond is

$$(5\text{-}12)\quad N(C\text{-}C) = \int_0^{\pi} \chi(\vec{p})^* \chi(\vec{p})\, 2\pi p^2 \sin\Theta \, d\Theta$$

where $\chi(\vec{p})^*\chi(\vec{p}) = \chi_C(\vec{p})^*\chi_C(\vec{p})\left[1 + S_{ab}\cos(pR_{CC}\cos\Theta)\right]$,

and $\chi_C(\vec{p}) = (2\pi)^{-3/2} \int \exp(-i\vec{p}\cdot\vec{r})\psi(C)\psi_+(r)d\vec{r}$.

Then equation (5-12) becomes

$$(5\text{-}12')\quad N(C\text{-}C) = \frac{1}{1 + S_{ab}^2}\left\{N_C(p) + S_{ab}\, N_{ab}(p)\right\}$$

where $N_C(p)$ is given in equation (5-6), and

$$N_{ab}(p) = \frac{2p^2}{(1+\sigma^2)}\left\{X_1(p)^2 \sin(pR_{CC})/(pR_{CC}) + 3\sigma^2 X_2(p)^2 \times\left[\sin(pR_{CC})/(pR_{CC}) + 2\cos(pR_{CC})/(pR_{CC})^2 - 2\sin(pR_{CC})/(pR_{CC})^3\right]\right\},$$

in which $X_1(p)$ and $X_2(p)$ are given in equations (5-7) and (5-8) respectively.

5.3 Results and Conclusion

Since the calculated positron wave functions are numerical values, the momentum distributions N(C-H) and N(C-C) were evaluated numerically by computer and plotted in Figures 5.3 and 5.4 respectively. Results for methane, hexane, and decane are shown in Figures 5.5, 5.6, and 5.7 respectively. In all cases, the calculated curves are in a good agreement with the experimental data.

From the several different theoretical approaches and their respective interpretations made in Chapters 3, 4, and 5, we can conclude that the peak of the higher momentum component of the experimental data is the direct measurement of the most probable momentum of covalent electrons in the hydrocarbons, and that in the detailed analysis of the observed momentum distribution, the effect of the positron wave function can not be ignored.

FIGURE 5.3

The Calculated Momentum Distribution N(C-H)

The dashed curve is the calculated N(C-H) with $\psi_+(r) = 1$.

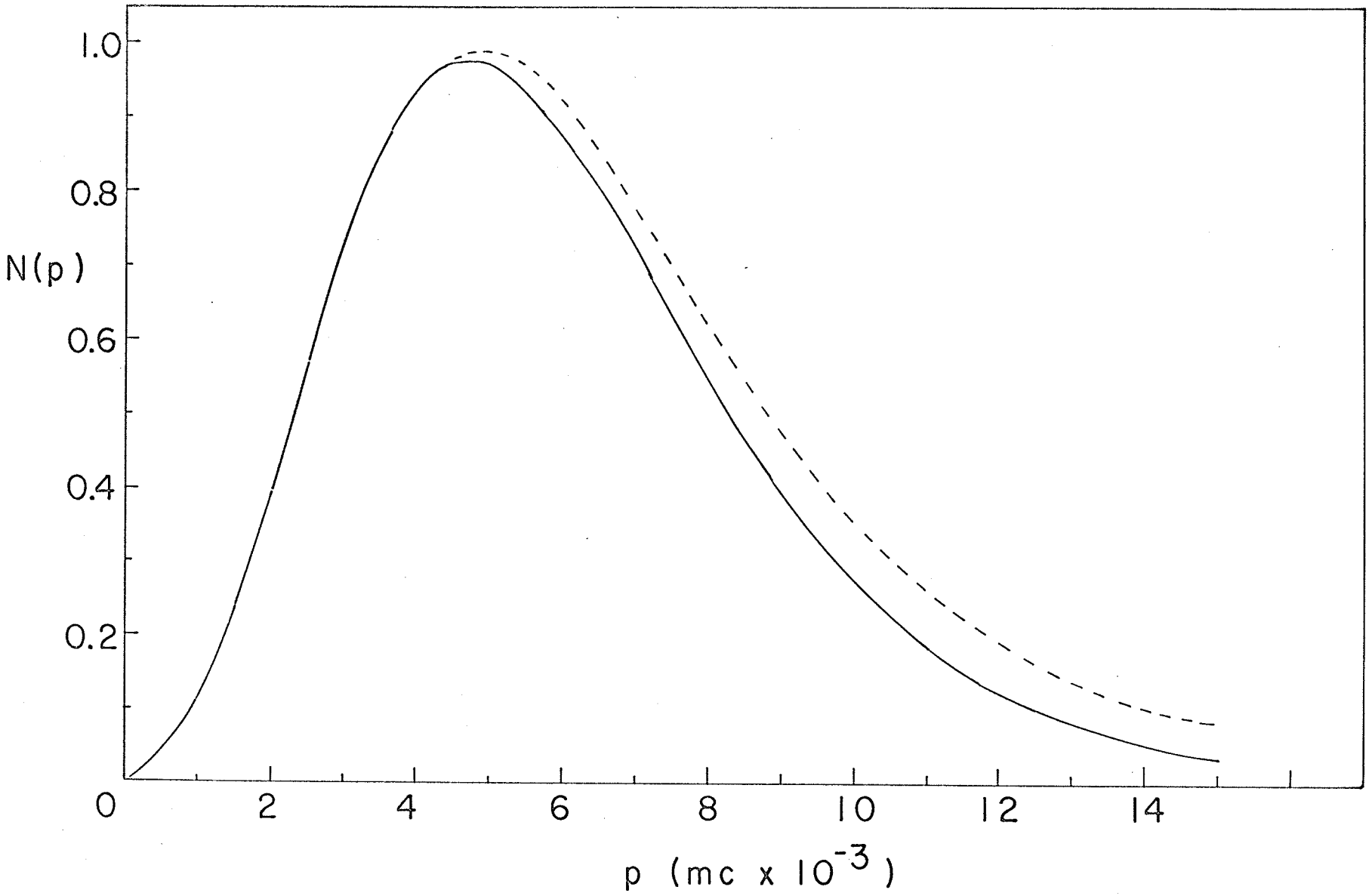
1.0
0.8
N(p)
0.6
0.4
0.2
0
2
4
6
8
10
12
14
p (mc x 10^-3)

FIGURE 5.4

The Calculated Momentum Distribution N(C-C)

The dashed curve is the calculated N(C-C) with $\psi_t(r) = 1$.

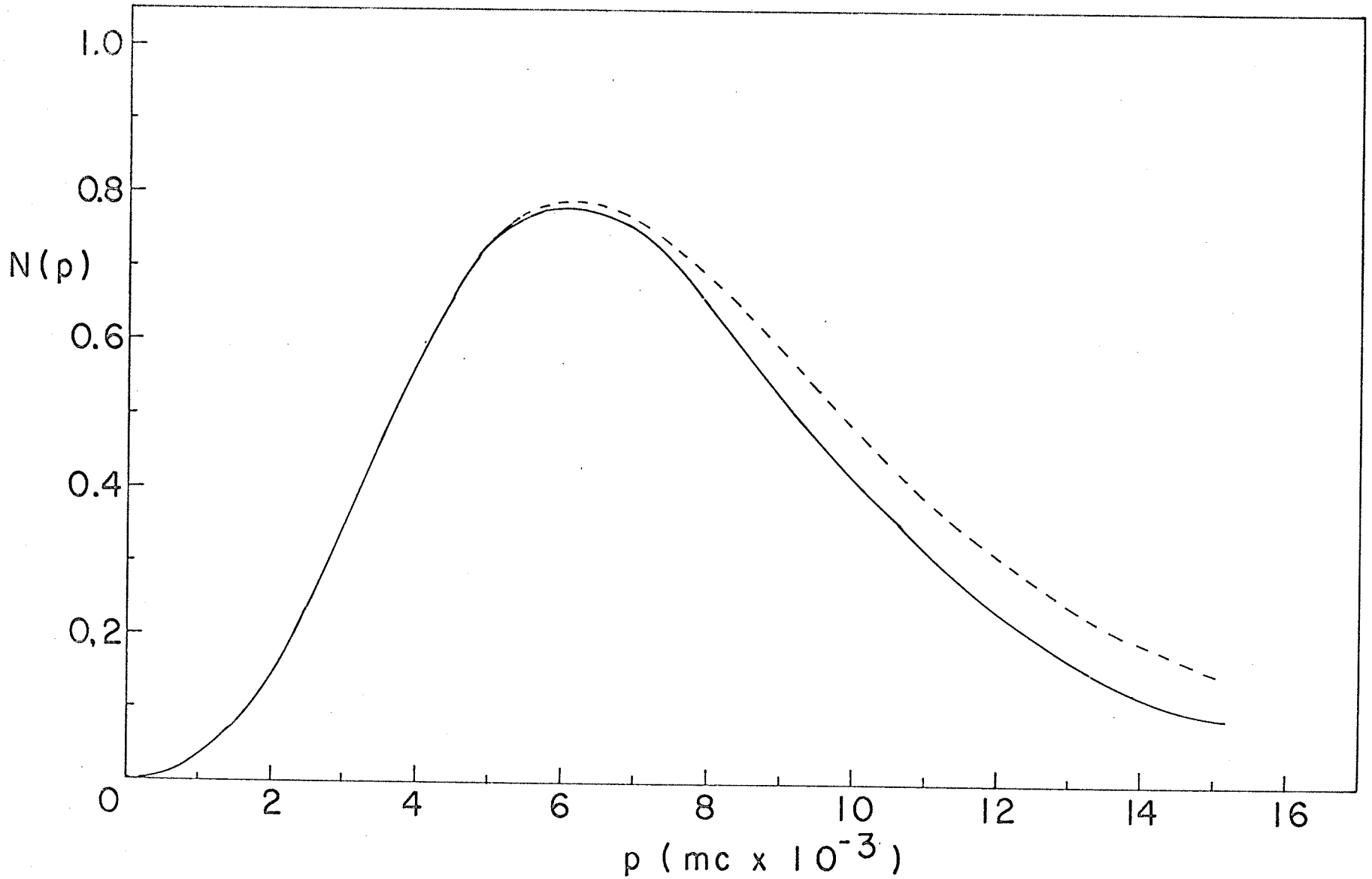
1.0
0.8
N(p)
0.6
0.4
0,2
0
2
4
6
8
10
12
14
16
p (mc x 10^-3)

FIGURE 5.5

The Momentum Distribution for Methane

The solid line indicates the result of present calculation, and the dashed line is the calculated result with $\Psi_{+}(r) = 1$.

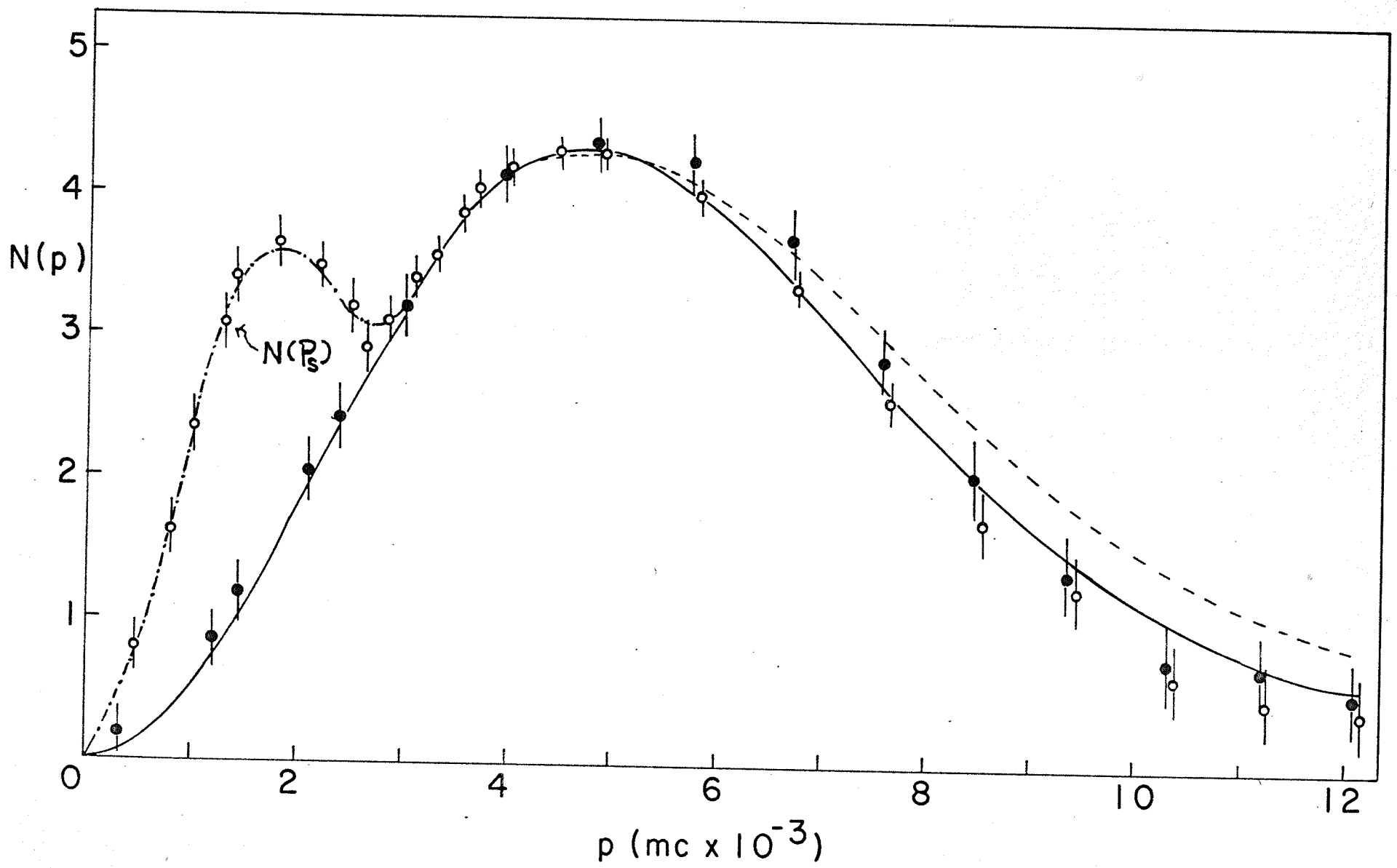
N(p)
N(Ps)
0
1
2
3
4
5
2
4
6
8
10
12
p (mc x 10^-3)

FIGURE 5.6

The Momentum Distribution for Hexane

The solid line indicates the result of present calculation for hexane, and curve A is the calculated result with $\psi_+(r) = 1$.

Curves B and C are N(C-H) and N(C-C) respectively (present calculation).

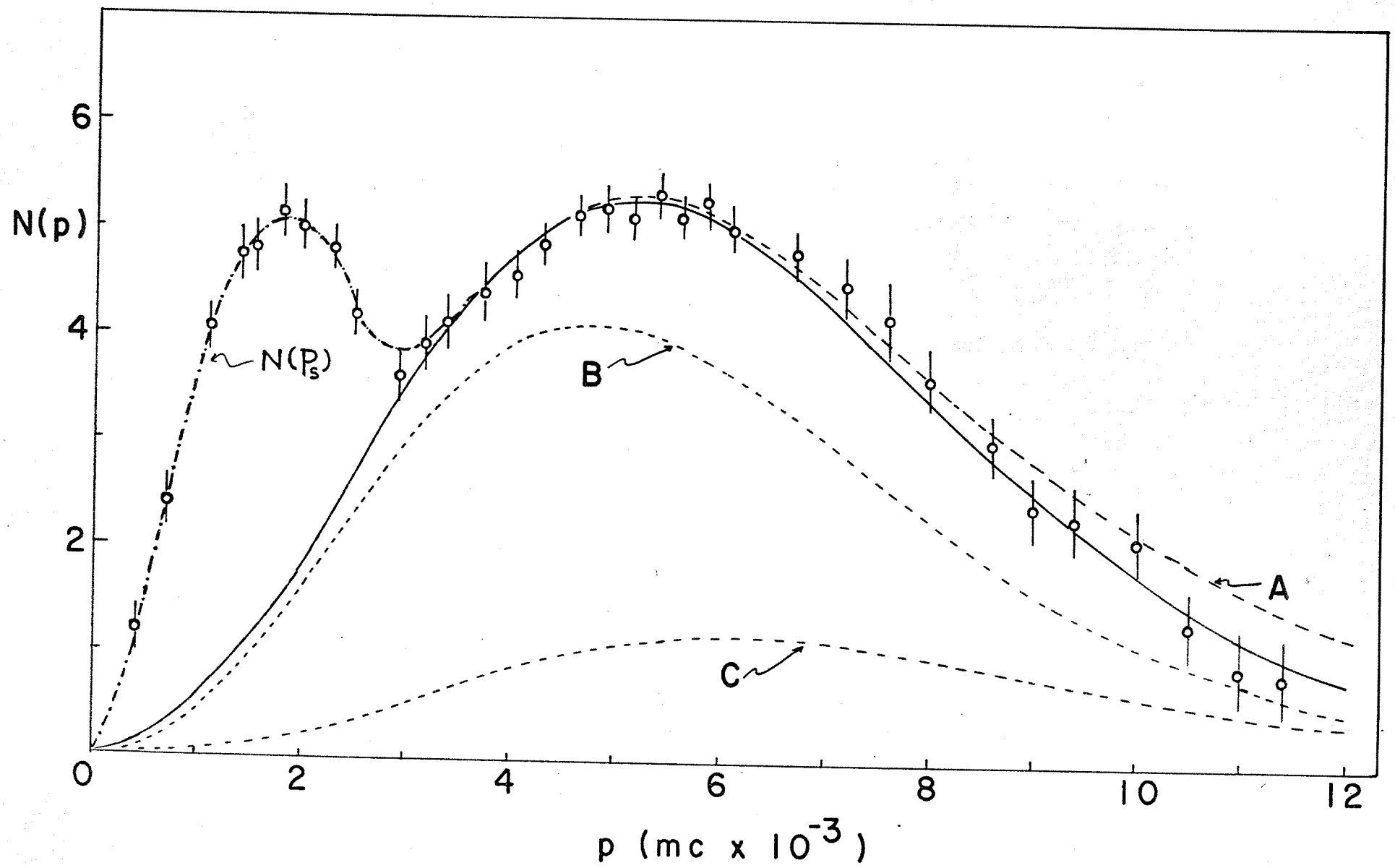
N(p)
6
4
2
0
2
4
6
8
10
12
p (mc x 10^-3)
N(p_s)
B
A
C

FIGURE 5.7

The Momentum Distribution for Decane

The solid line indicates the result of present calculation for decane, and curve A is the calculated result with $\psi_t(r) = 1$.

Curves B and C are N(C-H) and N(C-C) respectively (present calculation).

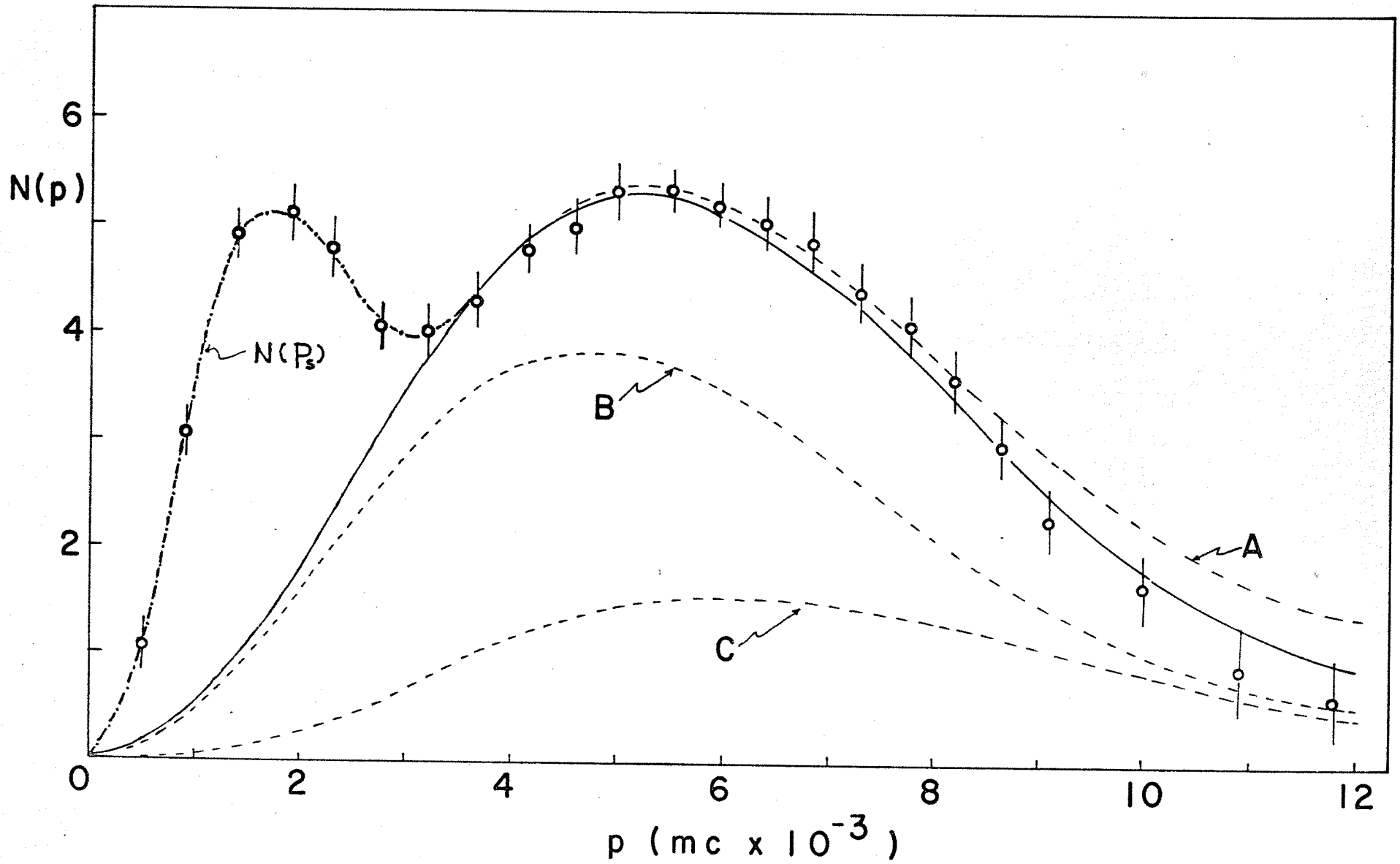
N(p)
6
4
2
0
2
4
6
8
10
12
p (mc x 10^-3)
N(Ps)
B
A
C

Chapter 6

Positron Annihilation in Alnico and $(La_{.7}Pb_{.3})MnO_3$

6.1 General

Positrons entering a metal are essentially thermalized in a time short compared with their average lifetime.[40,50] The momentum of an annihilating positron electron pair is therefore chiefly the momentum of the electron. The measurement of this momentum is easily done by observing the angle between the annihilation gamma rays. The positron samples mainly the most loosely bound electrons in the solid and also some of the core electrons. The problem of predicting the positron electron annihilation possibilities for systems containing serveral different types of atoms has been undertaken in this work. Samples under investigation were Alnico and $(La_{.7}Pb_{.3})MnO_3$ crystals.

6.2 Results and Discussion

The experimental results for Alnico and $(La_{.7}Pb_{.3})MnO_3$ are shown in Figure 6.2 and 6.3 respectively. Because of the complicated and not well-understood potential energy in the Hamiltonian, it is very difficult to make a reasonable quantitative calculation of wave functions for electrons as well as for positrons in these materials. Therefore, only qualitative interpretations and semi-quantitative calculations will be made in this Chapter.

A. Alnico

To understand the results for Alnico, it is helpful to show the results for copper which have been studied extensively by several authors.[43,44,45] Figure 6.1 shows present measurements for copper which are in agreement with those of previous arthors. The experimental curve noted by the closed circles has been fitted with a parabola, corresponding to free electrons, at the low momentum region as indicated by dotted curve A. The dotted curve B has been calculated on the basis of annihilation of 3d Cu electrons with a positron,[44] having a form of

$$C(p) = (1 + \zeta^2 + \tfrac{1}{2}\zeta^4)\exp(-\zeta^2),$$

where $\zeta = \frac{a}{\sqrt{7}}p$ and "a" is the 3d core radius. The intersection of curves A and B then gives us a measure of the Fermi level for Cu which from these experiments is 7.1 ev.

Now considering the case of Alnico I (12% Al, 20% Ni, 5% Co, 63% Fe), the contribution of Aluminum to the angular correlation curve is mainly due to the conduction electrons, since the probability of the core electrons of Al annihilating with a positron is small even if compared with the d electrons in Fe, Ni and Co. Moreover, the conduction electrons of Al in Alnico are not truly "free" electrons since they are coupled with Fe, Ni and Co. As seen from Figure 6.2, the parabolic portion of the angular correlation curve continues only up to 3.5 milliradians whereas in the case of pure Al there is a

good fit of inverted parabola to the experimental curve up to the cutoff at the angle corresponding to the Fermi momentum.[43]

Fe, Ni and Co also contribute conduction electrons to the Alnico as well as Al. All "conduction electrons"(better called outermost electrons) will behave the same way as far as the positron is concerned. These electrons all behave like 4s-electrons and the total angular correlation curve can be considered to be composed of two parts: a contribution by all the electrons in the 4s band and a contribution due the 3d band in Fe, Ni and Co (we are neglecting small contributions due to the core electrons). Since the 3d wave functions of Fe, Ni and Co are much alike we merely used one 3d wave function to calculate the overlap with the positron wave function. When the contribution due to the 3d electrons (curve A, in Figure 6.2) are subtracted from the experimental curve (Figure 6.2,dotted curve) the rest of the curve fits well to one calculated from 4s hydrogen-like wave function, curve B. If we extend the inverted parabola, curve C in Figure 6.2, to meet the d-electron distribution as we did in copper, then the cutoff point is at 5.9 milliradians (corresponding to 8.8 ev.). This we call the free Fermi energy for Alnico, if there is such a thing for this alloy. The calculated Fermi energy of Al based on the electron gas model assuming 3 conduction electrons per atom is 11.5 ev and the Fermi energies for Fe, Ni and Co based on .7 conduction electron per atom are in the range of 5 to 6 ev. When these four kinds of atoms

are mixed and reach equilibrium the Fermi levels will be the same and in the region between 5 to 11.5 ev. This is consistent with our value of 8.8 ev from positron data.

B. $(La_{.7}Pb_{.3})MnO_3$

The ionic crystals $LaMnO_3$ and $PbMnO_3$ are antiferromagnetic semi-conductors. Mixed crystals of $LaMnO_3$-$PbMnO_3$ containing up to 30% of $PbMnO_3$ are ferromagnetic with pervoskite structure and exhibit a conductivity of 10^2 ohm^{-1}-cm^{-1} at this concentration. The properties of ferromagnetism and conductivity in $(La_{.7}Pb_{.3})MnO_3$ are accounted for by the "double exchange process"[46].

Experiments on the alkali halides have indicated that the 2-photon angular correlations are almost independant of the positive ions[47], that is, they are only dependant on the negative ions. Theoretically then this is interpreted to mean that in an ionic crystal the positron wave function is concentrated about the negative ions and therefore the positrons are most likely to annihilate with the outermost electrons of the negative ions. In the $(La_{.7}Pb_{.3})MnO_3$ crystals the positive ions La^{+++}, Pb^{++}, Mn^{+++} and Mn^{++++} are expected to make little or no contribution to the angular correlations. Most of the positrons are concentrated at the site of the O^{--} ions and annihilate with the 2s- and 2p-like electrons of the O^{--} ions.

The experimental angular correlation curves is shown in Figure 6.3. They can be fitted quite well to the function[44]

$$C(p) = c_1(1+\xi^2)\exp(-\xi^2) + c_2\exp(-\xi^2)$$

where $\xi = \frac{a}{\sqrt{5}}p$ and "a" is the O^{--} radius which has been taken as 1.4 Å and p is the momentum of the annihilating pair. The first term, $c_1(1+\xi^2)\exp(-\xi^2)$, is plotted as curve A in Figure 6.3 and corresponds to the 2p electrons while the second terms, $c_2\exp(-\xi^2)$ corresponds to the 2s electrons annihilating with the positrons.

The sum of curves A and B fits the experimental curve except at the higher momentum region where the calculated curve drops faster than the experimental one. This discrepancy might be removed by considering annihilations with the 3d electrons of the transition elements or with core electrons of the oxygen or some combination of these possibilities. Unfortunately the discrepancy is so small that no clear cut picture can be presented.

We can however say that positron annihilation with the 3d electrons which is responsible for the ferromagnetic properties is not significant. An experiment was performed on the perovskite crystal in which angular correlation curves were run with the magnetization vector first in the direction of the positron beam entering the sample and then opposite to the direction. Similar experiments[23,24] on Fe and Ni showed a considerable polarization effect while for the

perovskite crystal considered here the angular distributions were independant of the orientation of the crystal in the magnetic field. This leads us to conclude that there are virtually no positrons annihilating with the magnetic 3d electrons in $(La_{.7}Pb_{.3})MnO_3$.

FIGURE 6.1

The Angular Distribution for Cu

A ---- inverted parabola

B ---- 3d electrons

p_F---- Fermi momentum

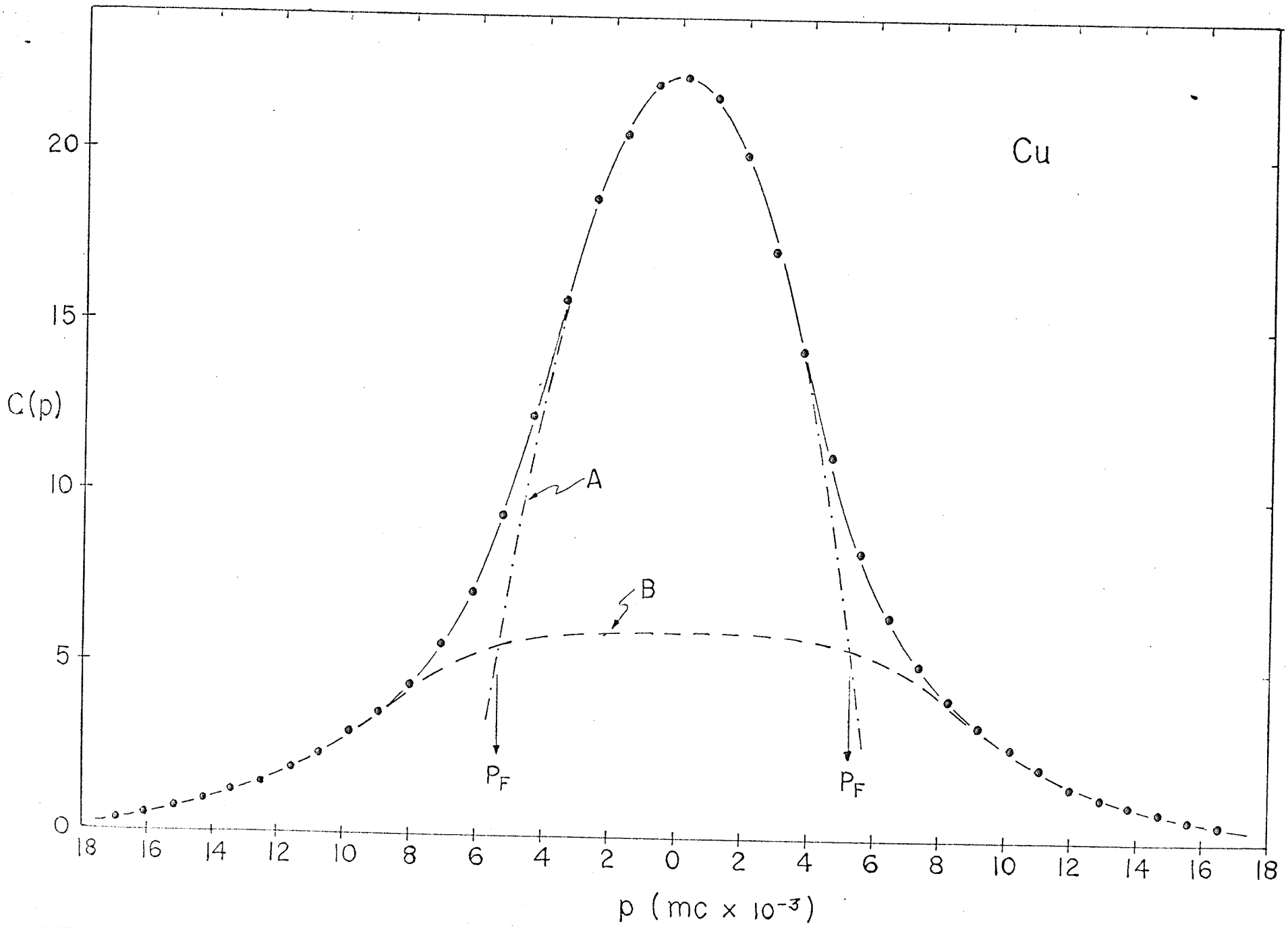
Cu
C(p)
20
15
10
5
0
A
B
P_F
P_F
18 16 14 12 10 8 6 4 2 0 2 4 6 8 10 12 14 16 18
p (mc x 10^{-3})

FIGURE 6.2

The Angular Distribution for Alnico

A ---- 3d electrons

B ---- 4s electrons

C ---- inverted parabola

D ---- intersection of curves A and C

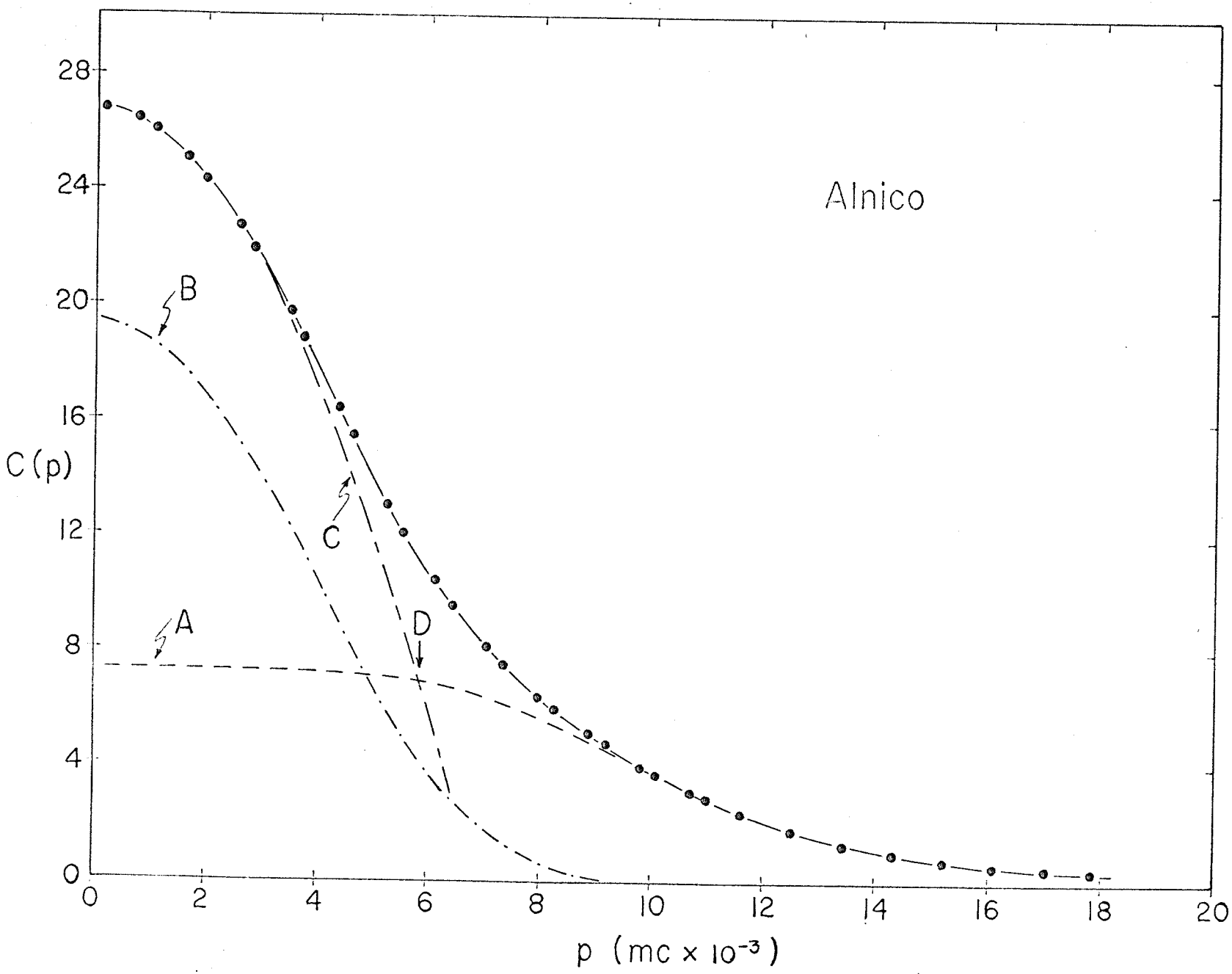
Alnico
A
B
C
D
C(p)
p (mc x 10⁻³)
0
4
8
12
16
20
24
28
0
2
4
6
8
10
12
14
16
18
20

FIGURE 6.3

The Angular Distribution for $(La_{.7}Pb_{.3})MnO_3$

A ---- 2p electrons

B ---- 2s electrons

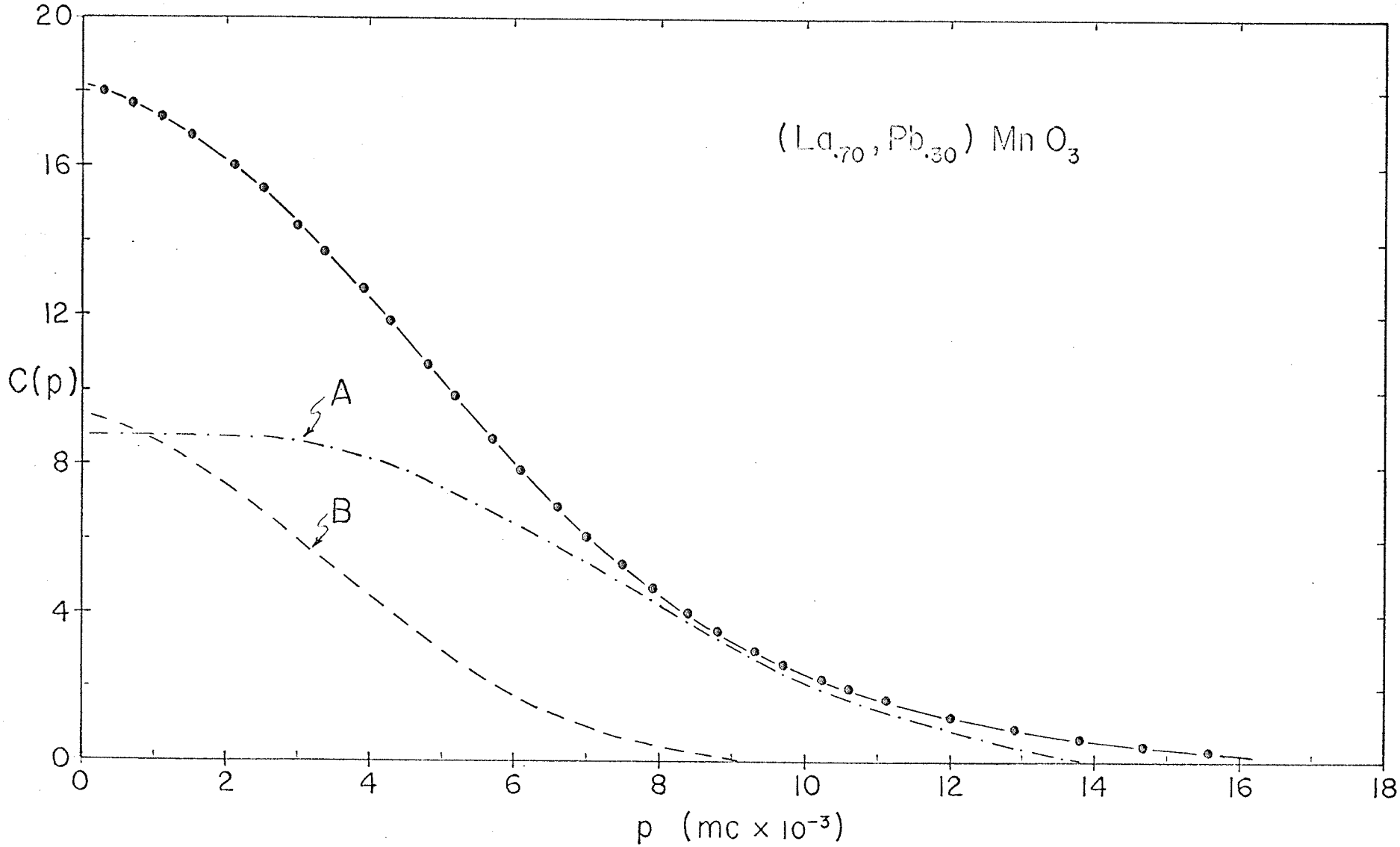
20
16
12
8
4
0
C(p)
A
B
0
2
4
6
8
10
12
14
16
18
p (mc × 10⁻³)
(La.70, Pb.30) Mn O3

Appendix A

The Angular Resolution Function

In the following analysis, the origin of the Cartesian coordinate system is at the mid-point of a line jointing the two detectors. This line is the x-axis. The z-axis is parallel to the direction of motion of the movable detector.

We shall consider the resolution function in the z direction assuming that the detectors extend to infinity in the y direction (vertical).

For two sets ofslits of width s (i.e.,s_z) at a distance L on either side of an infinitely thin source, the geometrical resolution function is easily seen to by an isosceles triangle with a base width of 2s. The "sourse" refers to the portion of the sample in which the positrons annihilate. A single isosceles triangle of unit height centered at z_o is given by

$$(A\text{-}1) \qquad f(z,z_o) = \begin{cases} 1 - \left|\dfrac{z - z_o}{z}\right|, & \text{for } |z - z_o| < s \\ 0, & \text{for } |z - z_o| > s. \end{cases}$$

We will first assume that the sources of annihilation radiation are uniformly distributed through a thickness d

defined by the width of the fine collimating slit of the sample housing (see Section 2.1A), so that all triangles are given equal weight. Then the total resolution function is given by

$$(A\text{-}2) \quad R(z)= \int_{-d}^{d} f(z,z_o)dz_o= \int_{-d}^{d} \left(1 - \left|\frac{z - z_o}{s}\right|\right) dz_o \ .$$

The evaluation of the above integration is dependent on the values of s and d. For $s-d < d < s$, which is the case in our experiments, the integration in equation (A-2) can be easily performed in three steps, viz.,

$$R_1(z)= \int_{-d}^{z+s} \left[1 - \frac{z_o - z}{s}\right] dz_o = \frac{(s + d + z)^2}{2s}, \quad \text{for } -(d+s) \leq z \leq -d.$$

$$R_2(z)= \int_{-d}^{z} \left[1 - \frac{z - z_o}{s}\right] dz_o + \int_{z}^{z+s} \left[1 - \frac{z_o - z}{s}\right] dz_o$$

$$= \frac{2s^2 - (s - d - z)^2}{2s}, \qquad \text{for } -d \leq z \leq d-s.$$

$$R_3(z) = \int_{-d}^{z} \left[1 - \frac{z - z_o}{s}\right] dz_o + \int_{z}^{d} \left[1 - \frac{z_o - z}{s}\right] dz_o$$

$$= 2d \cdot \left(1 - \frac{d}{2s} - \frac{z^2}{2sd}\right) , \qquad \text{for } d-s \leq z \leq s-d.$$

Actually, the assumption of a uniformly distributed source is unrealistic. The intensity of the source is a function of the penetration depth of positrons. On the basis of experimental data, Gubernator and Flammersfeld[48] have proposed an empirical relationship between the positron range R^+ and its initial energy E^+, viz.,

$$(A\text{-}3) \qquad E^+ = 29.7 \cdot (Z/A) \cdot (R^+)^{.60} \qquad (E^+ \text{ in kev. and } R^+ \text{ in mg/cm}^2).$$

The positron spectrum for Na^{22} has a maximum energy of .54 Mev. Because of the energy losses in passing through the windows of the source and the sample cell, it is estimated that positrons will have maximum energies about .4 Mev. when they enter the effective sample region defined by the fine collimating slit of the sample housing. Substitution of this value for $E^+ = 400$ kev into the above equation, yields the maximum range R_m^+, i.e.,

$$R_m^+ = \left[\frac{400}{29.6} \cdot (A/Z)\right]^{5/3} \qquad \text{mg/cm}^2.$$

For example, in the case of liquid methane, the least dense meterial studied, $R_m^+ = 167$ mg/cm^2, corresponding to depth of .40 cm.

The transmission curve for a continuous positron spectrum is very nearly exponential (but hits a definite zero at R_m^+).[49] Thus the intensity of positrons at depth z is approximately

$$I = \exp(-\mu z)$$

where the absorption coefficient $\mu = 4.5/R_m^+$ which is chosen to bring $I = 0.01$ for $z = R_m^+$. This empirical relationship between u and R_m fits well to the experimental data of positrons penetrating C, Al, Cu, Sn and Pb.[49]

Returning to the problem of the angular resolution function, the triangular resolution functions must be weighted by the factor of $\exp[-u(d-z_o)/2]$ as z_o varies from -d to d. Therefore, the total resolution function is

$$(A\text{-}4) \qquad R(z) = \int_{-d}^{d} f(z, z_o) e^{k(d-z_o)} dz_o$$

$$= \int_{-d}^{d} \left[1 - \left|\frac{z - z_o}{s}\right|\right] e^{k(d-z_o)} dz_o$$

where $k = -\mu/2 = -4.5/2R_m^+$.

For the case of $s-d \leq d \leq s$, the integration must be performed in five steps in the following way.

$$R_1(z) = \int_{-d}^{z+s} \left[1 - \frac{z_o - z}{s}\right] e^{k(d-z_o)} dz_o$$

$$= \left[e^{-k(z+s-d)} - (1-zk-sk-dk)e^{2kd}\right]/k^2 s, \quad \text{for} \quad -(d+s) \leq z \leq -d.$$

$$R_2(z) = \int_{-d}^{z} \left(1 - \frac{z - z_o}{s}\right) e^{k(d-z_o)} dz_o + \int_{z}^{z+s} \left(1 - \frac{z_o - z}{s}\right) e^{k(d-z_o)} dz_o$$

$$= \left[e^{-k(z+s-d)} - 2e^{k(d-z)} + (sk-zk-dk+1)e^{2kd}\right]/k^2 s,$$

for $-d \leq z \leq d-s$.

$$R_3(z) = \int_{-d}^{z} \left(1 - \frac{z - z_o}{s}\right) e^{k(d-z_o)} dz_o + \int_{z}^{d} \left(1 - \frac{z_o - z}{s}\right) e^{k(d-z_o)} dz_o$$

$$= \left[(dk+1-sk+zk) - 2e^{k(d-z)} + (sk-zk-dk+1)e^{2dk}\right]/k^2 s,$$

for $d-s \leq z \leq s-d$.

$$R_4(z) = \int_{z-s}^{z} \left(1 - \frac{z - z_o}{s}\right) e^{k(d-z_o)} dz_o + \int_{z}^{d} \left(1 - \frac{z_o - z}{s}\right) e^{k(d-z_o)} dz_o$$

$$= \left[(dk+1-sk-zk) + e^{k(d-z+s)} - 2e^{k(d-z)}\right]/k^2 s,$$

for $s-d \leq z \leq d$

$$R_5(z) = \int_{z-s}^{d} \left(1 - \frac{z - z_o}{s}\right) e^{k(d-z_o)} dz_o$$

$$= \left[e^{k(d-z+s)} - (sk-zk+dk+1)\right]/k^2 s, \quad \text{for} \quad d \leq z \leq d+s.$$

The results of equations (A-2) and (A-4) for liquid methane sample have been plotted as $R(\theta)$ vs. θ, where $\theta = z/L$ in milliradians, in Figure A.1 using $s = d = .60$ milliradians. For comparison, both curves are normalized to the same height at the peaks. The position of the peaks have been chosen as the zero position of θ.

FIGURE A.1

The Angular Resolution Function

A----- uniformly distributed source

B ---- exponential distributed source

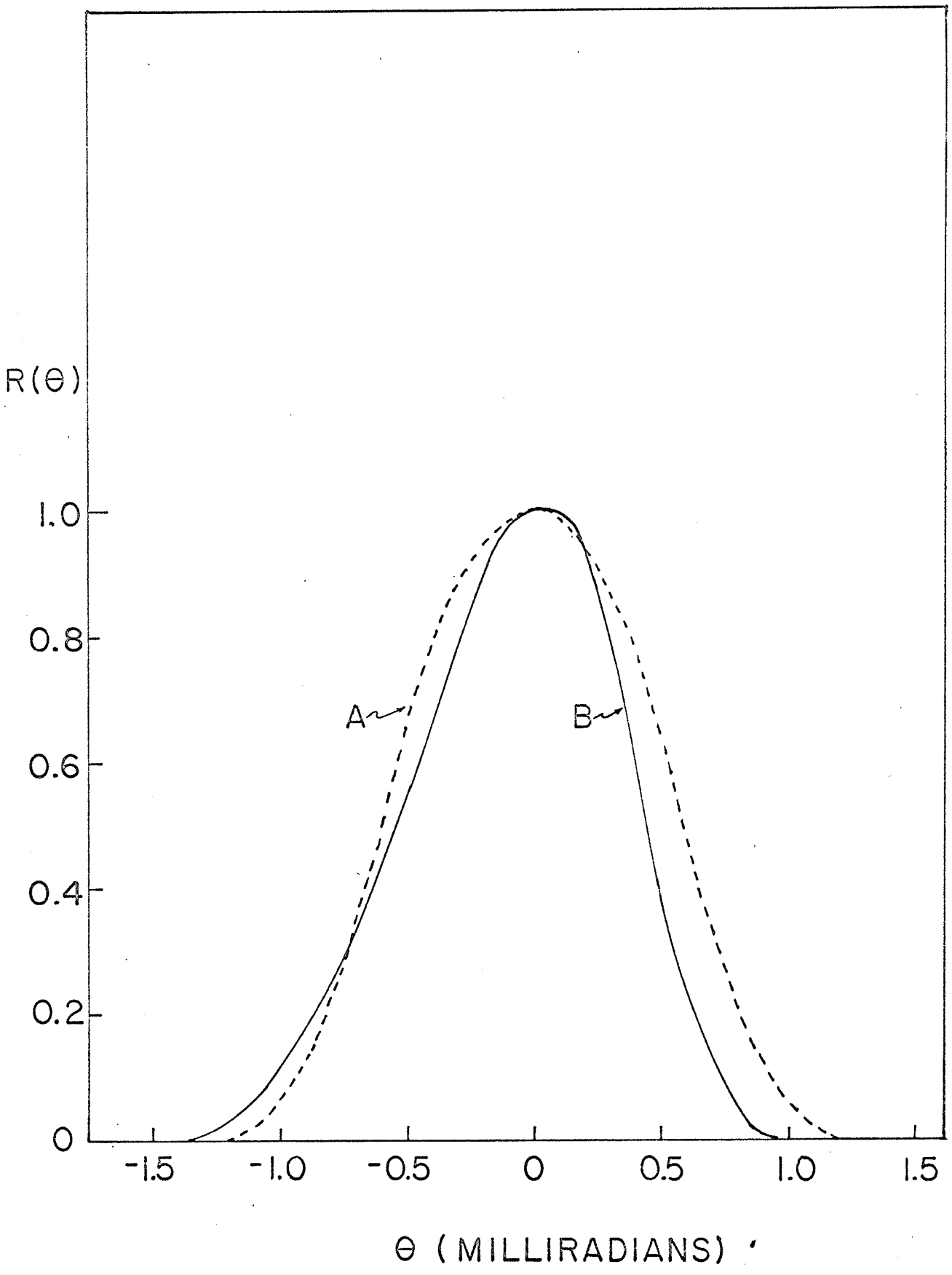
R(θ)
1.0
0.8
0.6
0.4
0.2
0
A
B
-1.5
-1.0
-0.5
0
0.5
1.0
1.5
θ (MILLIRADIANS)

Appendix B

Some Useful Integrals

The following integrations are useful for the calculation of the momentum wave functions in Chapters 3 and 4.

(B-1) $$\int_0^\infty x^n\, e^{-(a-ik)x} dx$$

$$= e^{-(a-ik)x}\left[\frac{1}{D-(a-ik)}\right]x^n\Big|_0^\infty \qquad \text{(where D is the differential operator, d/dx)}$$

$$= \frac{e^{-(a-ik)x}}{-(a-ik)}\left[\frac{1}{1-D/(a-ik)}\right]x^n\Big|_0^\infty$$

$$= -\frac{e^{-(a-ik)x}}{(a-ik)}\left[1+\frac{D}{(a-ik)}+\frac{D^2}{(a-ik)^2}+\cdots+\frac{D^n}{(a-ik)^n}\right]x^n\Big|_0^\infty$$

$$= -\frac{e^{-(a-ik)x}}{(a-ik)}\left[x^n+\frac{nx^{n-1}}{(a-ik)}+\frac{n(n-1)x^{n-2}}{(a-ik)^2}+\cdots+\frac{n!}{(a-ik)^n}\right]\Big|_0^\infty$$

$$= \frac{n!\,(a+ik)^{n+1}}{(a^2+k^2)^{n+1}}\ .$$

(B-2) $$I_n = \int_0^\infty x^n\, e^{-ax}\sin(kx)dx = Im\left\{\int_0^\infty x^n\, e^{-(a-ik)x}\, dx\right\}$$

$$= \mathrm{Im}\left\{\frac{n!(a+ik)^{n+1}}{(a^2+k^2)^{n+1}}\right\}.$$

For $n=1, 2, 3,$ and 4, I_n are given as follows:

$$I_1 = \frac{2ak}{(a^2+k^2)^2}$$

$$I_2 = \frac{2(3a^2k-k^3)}{(a^2+k^2)^3}$$

$$I_3 = \frac{6(4a^3k-4ak^3)}{(a^2+k^2)^4}$$

$$I_4 = \frac{24(5a^4k-10a^2k^3+k^5)}{(a^2+k^2)^5} .$$

(B-3) $$R_n = \int_0^\infty x^n e^{-ax}\cos(kx)dx = \mathrm{Re}\left\{\int_0^\infty x^n e^{-(a-ik)x}\,dx\right\}$$

$$= \mathrm{Re}\left\{\frac{n!(a+ik)^{n+1}}{(a^2+k^2)^{n+1}}\right\}.$$

For $n=1, 2, 3,$ and 4, R_n are given as follows:

$$R_1 = \frac{a^2-k^2}{(a^2+k^2)^2}$$

$$R_2 = \frac{2(a^3-3ak^2)}{(a^2+k^2)^3}$$

$$R_3 = \frac{6(a^4-6a^2k^2+k^4)}{(a^2+k^2)^4}$$

$$R_4 = \frac{12(a^5-10a^3k^2+5ak^4)}{(a^2+k^2)^5} .$$

Appendix C

Evaluation of Overlap Integrals

Since the overlap integral involves two-center integration, it is convenient to use prolate spheroidal coordinates, (λ, μ, ϕ), defined by

$$\lambda = \frac{(r_a + r_b)}{R} , \qquad (1 \leq \lambda \leq \infty)$$

$$\mu = \frac{(r_a - r_b)}{R} , \qquad (-1 \leq \mu \leq 1)$$

$$\phi = \phi , \qquad (0 \leq \phi \leq 2\pi),$$

here we regard (r_a, θ_a, ϕ) as spherical polar coordinates which then satisfy the relations,

$$r_a = \frac{R}{2}(\lambda + \mu), \qquad r_b = \frac{R}{2}(\lambda - \mu),$$

$$\cos\theta_a = \frac{\lambda\mu + 1}{\lambda + \mu} , \qquad \cos\theta_b = \frac{\lambda\mu - 1}{\lambda - \mu},$$

$$\sin^2\theta_a = \frac{(\lambda^2-1)(1-\mu^2)}{(\lambda+\mu)^2} , \qquad \sin^2\theta_b = \frac{(\lambda^2-1)(1-\mu^2)}{(\lambda-\mu)^2},$$

and hence,

$r_a + r_b = R\lambda$,

$r_a - r_b = R\mu$,

$r_a r_b = (R/2)^2(\lambda^2 - \mu^2)$,

and volume element $dv = (R/2)^3(\lambda^2-\mu^2)d\lambda d\mu d\phi$.

I. Evaluation of S_{ab} Overlap Integral:

In equation (3-9), S_{ab} was defined as

(C-1) $$S_{ab} = \int \psi_a(C)\psi_b(C)dv$$

where $\psi_a(C)$ and $\psi_b(C)$ are wave functions corresponding to the two carbon atoms centered at A and B respectively, and have the form

$$\psi_a(C) = \frac{\psi_{2s}(C_a) + \sigma\psi_{2p}(C_a)}{\sqrt{1+\sigma^2}},$$

$$\psi_b(C) = \frac{\psi_{2s}(C_b) + \sigma\psi_{2p}(C_b)}{\sqrt{1+\sigma^2}},$$

where σ is the mixing coefficient.

Substituting the above equations into equation (C-1), we get

$$(C\text{-}2)\quad S_{ab}=\Big\{\int \psi_{2s}(C_a)\psi_{2s}(C_b)dv + \sigma^2\int \psi_{2p}(C_a)\psi_{2p}(C_b)dv + \sigma\int\left[\psi_{2s}(C_a)\psi_{2p}(C_b) + \psi_{2p}(C_a)\psi_{2s}(C_b)\right]dv\Big\}/(1+\sigma^2)$$

$$= \frac{1}{1+\sigma^2}\left[I_1+\sigma^2 I_2 + \sigma I_3\right] .$$

For simplifying the calculation, we will use the ordinary Slater's orbital wave functions for $\psi_{2s}(C)$ and $\psi_{2p}(C)$, i.e.,

$$\psi_{2s}(C)=\sqrt{\frac{k^5}{3\pi}}\, re^{-kr},$$

$$\psi_{2p}(C)=\sqrt{\frac{k^5}{\pi}}\, re^{-kr}\cos\theta,$$

where $k=1.625$ in a.u.

Now we will evaluate integrals I_1, I_2 and I_3 in equation (C-2).

$$(C\text{-}3) \qquad I_1 = \int \psi_{2s}(C_a)\,\psi_{2s}(C_b)\,dv$$

$$= \frac{k^5}{3\pi} \int r_a r_b e^{-k(r_a + r_b)}\, dv$$

$$= \frac{k^5}{3\pi} \int_1^\infty \int_{-1}^1 \int_0^{2\pi} (R/2)^2(\lambda^2-\mu^2)e^{-kR\lambda} \cdot (R/2)^3(\lambda^2-\mu^2)\,d\lambda\,d\mu\,d\phi$$

$$= \frac{2}{3}(kR/2)^5 \int_1^\infty d\lambda \int_{-1}^1 d\mu\; e^{-kR\lambda}\,(\lambda^2-\mu^2)^2$$

$$= \frac{4}{3}(\alpha/2)^5 \left[A_4(1,\alpha) - \frac{2}{3}A_2(1,\alpha) + \frac{1}{5}A_0(1,\alpha)\right],$$

where $\alpha = kR$, R is the distance between two carbon atoms which is taken to be 2.9 a.u., and

$$A_n(1,\alpha) = \int_1^\infty e^{-\alpha\lambda}\lambda^n\, d\lambda$$

$$= \frac{e^{-\alpha}}{\alpha}\left[1 + \frac{n}{\alpha} + \frac{n(n-1)}{\alpha^2} + \cdots\cdots + \frac{n!}{\alpha^n}\right]$$

(see Appendix B)

(C-4) $$I_2 = \int \psi_{2p}(C_a)\psi_{2p}(C_b)dv$$

$$= \frac{k^5}{\pi} \int r_a r_b e^{-k(r_a + r_b)} \cos\theta_a \cos\theta_b dv$$

$$= \frac{k^5}{\pi} \int_1^\infty \int_{-1}^1 \int_0^{2\pi} (R/2)^2(\lambda^2-\mu^2)d^{-kR\lambda} \cdot \frac{(\lambda\mu+1)(\lambda\mu-1)}{\lambda^2 - \mu^2}$$

$$\times (R/2)^3(\lambda^2-\mu^2)d\lambda d\mu d\phi$$

$$= 2(kR/2)^5 \int_1^\infty d\lambda \int_{-1}^1 d\mu \; e^{-kR\lambda} (\lambda\mu+1)(\lambda\mu-1)(\lambda^2-\mu^2)$$

$$= \frac{\alpha^5}{24} \left[A_4(1,\alpha) - \frac{18}{5} A_2(1,\alpha) + A_0(1,\alpha) \right] .$$

(C-5) $$I_3 = \int \left[\psi_{2s}(C_a)\psi_{2p}(C_b) + \psi_{2p}(C_a)\psi_{2s}(C_b) \right] dv$$

$$= \frac{k^5}{\pi\sqrt{3}} \int r_a r_b e^{-k(r_a + r_b)} (\cos\theta_a + \cos\theta_b) dv$$

$$= \frac{k^5}{\pi\sqrt{3}} \int_1^{\infty}\int_{-1}^{1}\int_0^{2\pi} (R/2)^2(\lambda^2-\mu^2)e^{-kR\lambda}\cdot\frac{2(\lambda^2-1)}{\lambda^2-\mu^2}(R/2)^3(\lambda^2-\mu^2)\,d\lambda\,d\mu\,d\phi$$

$$= \frac{4}{\sqrt{3}}(kR/2)^5\int_1^{\infty} d\lambda\, e^{-kR\lambda}\int_{-1}^{1} d\mu\left[(\lambda^2-1)\lambda^2\mu - (\lambda^2-1)\mu^3\right]$$

$$= 0.$$

Now for $k = 1.625$, $R = 2.91$, $\alpha = kR = 4.73$, and

$A_0(1,\alpha) = 0.001867$,

$A_2(1,\alpha) = 0.002823$,

$A_4(1,\alpha) = 0.004954$,

we get $I_1 = 0.339$ and $I_2 = 0.328$, and therefore

$$S_{ab} = (0.339 - 0.328\,\sigma^2)/(1+\sigma^2).$$

II. Evaluation of S_{CH} Overlap Integral:

The integral S_{CH} defined in equation (3-7) is given as

$$S_{CH} = \int \psi(C)\psi(H)\,dv$$

here again the atomic carbon wave function $\psi(C)$ is given as

$$\psi(C) = \frac{\psi_{2s}(C) + \sigma \psi_{2p}(C)}{\sqrt{1+\sigma^2}} \quad ,$$

and $\psi(H)$ is the hydrogen wave function, i.e.,

$$\psi(H) = \frac{1}{\sqrt{\pi}} e^{-r_h} \quad .$$

Then

$$(C\text{-}6) \quad S_{CH} = \frac{1}{\sqrt{1+\sigma^2}} \left\{ \int \psi_{2s}(C)\psi(H)dv + \sigma \int \psi_{2p}(C)\psi(H)dv \right\}$$

$$= \frac{1}{\sqrt{1+\sigma^2}} \left\{ B_1 + \sigma B_2 \right\},$$

and

$$B_1 = \int \psi_{2s}(C)\psi(H)dv = \frac{1}{\pi} (k^5/3)^{\frac{1}{2}} \int r_c e^{-kr_c} e^{-r_h} dv$$

$$= \frac{1}{\pi} (k^5/3)^{\frac{1}{2}} \int_1^{\infty} d\lambda \, e^{-R(k+1)\lambda/2} \int_{-1}^{1} d\mu \, e^{-R(k-1)\mu/2} (R/2)^4$$

$$\times 2\pi(\lambda+\mu)(\lambda^2-\mu^2)$$

$$= \frac{R^3}{4}(k^5/3)^{\frac{1}{2}} \int_1^{\infty} d\lambda\, e^{-R(k+1)\lambda/2}\ (a\lambda^3 + b\lambda^2 - c\lambda^2 + d)/(k-1)$$

$$= \frac{R^3}{4(k-1)}(k^5/3)^{\frac{1}{2}} \left[aA_3(1,\alpha) + bA_2(1,\alpha) - cA_1(1,\alpha) + dA_0(1,\alpha)\right]$$

where $\alpha = R(k+1)/2$, $\beta = R(k-1)/2$, and

$a = e^{\beta} - e^{-\beta}$

$b = e^{\beta}(1/\beta - 1) - e^{-\beta}(1 + 1/\beta)$

$c = e^{\beta}(1 - 2/\beta + 2/\beta^2) - e^{-\beta}(1 + 2/\beta + 2/\beta^2)$

$d = e^{\beta}(1 - 3/\beta + 6/\beta^2 - 6/\beta^3) + e^{-\beta}(1 + 3/\beta + 6/\beta^2 + 6/\beta^3)$;

$$B_2 = \int \psi_{2p}(C)\psi(H)dv = \frac{\sqrt{k^5}}{\pi}\int r_c \cos\theta_c\ e^{-kr_c}\ e^{-r_h}\ dv$$

$$= \frac{\sqrt{k^5}}{\pi}\int_1^{\infty}\int_{-1}^{1}\int_0^{2\pi}(R/2)^4\ e^{-kR(\lambda+\mu)/2}\ e^{-R(\lambda-\mu)/2}\ (\lambda\mu+1)(\lambda^2-\mu^2)d\lambda d\mu d\phi$$

$$= \frac{2}{\beta}\sqrt{k^5}(R/2)^4\left[bA_3(1,\alpha) + aA_2(1,\alpha) + dA_1(1,\alpha) - cA_0(1,\alpha)\right].$$

Now for $k = 1.625$ and $R = 2.0$ (the length of the C-H bond), we have $\alpha = 2.625$, $\beta = 0.625$,

$a = 1.32$, $b = -0.284$, $c = 0.398$, $d = 0.51$, and

$A_3(1,\alpha) = 0.09238$, $A_2(1,\alpha) = 0.05667$,

$A_1(1,\alpha) = 0.03813$, $A_0(1,\alpha) = 0.02762$.

Substituting the above values into B_1 and B_2, we get

$$S_{CH} = \frac{1}{\sqrt{1+6^2}}(0.612 + 0.307\,6).$$

Appendix D

Fortran IV Computer Programs

I. Positron Wave Function

```
C       CALCULATION OF POSITRON WAVE FUNCTION FROM EQ.(5-2).
C
C       THE NUMERICAL INTEGRATION PROCESS IS GIVEN IN REF.53.
C
C       THE INTEGRATION INTERVAL IS 0.05 A.U.
C
C     ..................................................
C
C
      DIMENSION V(99),X(99),E(999),Y(99),YY(99),D2Y(99),
     1D2YY(99),F(99),U(99)
      READ (1,15) (U(N), N = 1,32)
   15 FORMAT (10,F8.0)
C
C       THE INPUT DATA U IS THE SELF-CONSISTEN POTENTIAL
C       FROM REF.52, IN THE FORM OF U(R) = R·V(R)/(2Z).
C
      X(1)= 0.0
      DO 11 N= 2,32
      VV=FLOAT(N)
      X(N)=0.05*(VV-1.)
      V(N)=12.*U(N)/X(N)
   11 CONTINUE
C
C       THE SYMBOL F DENOTES THE POSITRON WAVE FUNCTION,
C       E IS THE EIGENVALUE, AND Y IS R+ IN EQ.(5-2).
C
      DO 10 I=1,999
      A=FLOAT(I)
      E(I)=A*0.005
      Y(1)=0.0
      Y(2)=0.00010
      F(1)=0.0
      F(2)=Y(2)/X(2)
      YY(1)=0.0
      YY(2)=-2.*(E(I)-V(2))*Y(2)
      DO 30 M=2,31
      J=M-1
      L=M+1
      D2YY(M)=0.
   50 D2Y(M)=0.0025*(YY(M)+D2YY(M)/12.)
      Y(L)=2.*Y(M)-Y(J)+D2Y(M)
```

```
      YY(L)=-2.*(E(I)-V(L))*Y(L)
      AA=YY(L)-2.*YY(M)+YY(J)
      D=ABS(D2YY(M)-AA)-0.0005
      IF(D)60,60,40
   40 D2YY(M)=AA
      GO TO 50
   60 F(L)=Y(L)/X(L)
   30 CONTINUE
      G=F(32)-F(31)-0.0001
      IF(G)99,99,10
   99 WRITE (3,90) E(I)
   90 FORMAT (12H EIGENVALUE=, F10.5)
      GO TO 100
   10 CONTINUE
C
C       NORMALIZATION OF THE WAVE FUNCTION.
C
  100 DO 20 MM=2,32
   20 F(MM)=F(MM)/F(32)
      WRITE (3,70)
   70 FORMAT (1H /5(21H      X          F(X)   ))
      WRITE (3,80) (X(N),F(N), N=1,32)
   80 FORMAT (1H /5(1H ,F9.4, F11,5))
      WRITE (3,222)
  222 FORMAT (1H /5(21H    X          V(X)   ))
      WRITE (3,111) (X(N),V(N),N=2,32)
  111 FORMAT (1H /5(1H ,F9.4, F11.5))
      END
```

II. Momentum Distributions

```
C       CALCULATIONS OF THE MOMENTUM DISTRIBUTIONS OF ANNIHILATING
C       POSITRON ELECTRON PAIRS IN C-H AND C-C BONDS.(CHAPTER 5).
C
C     ..................................................
C
      DIMENSION W(555),PM(555),F1(555),F2(555),WW(555),FH(555),
     1TNCC(555),TNCH(555)
C
C       THE INPUT DATA W IS THE POSITRON WAVE FUNCTION FOR
C       THE CARBON ATOM, AND WW IS FOR HYDROGEN .
C
C     ..........................................
C
      READ (1,10) (W(N),N=1,32)
      READ (1,10) (WW(N),N=1.30)
   10 FORMAT (10F8.0)
C
C       SAB IS THE CARBON-CARBON OVERLAP INTEGRAL.
C
C       SCH IS THE CARBON-HYDROGEN OVERLAP INTEGRAL.
C
C       RCC IS THE LENGTH OF C-C BOND.
C
C       RCH IS THE LENGTH OF C-H BOND.
C
C
      SAB=(0.339-0.328*3.)/4.
      SCH (0.612+0.307*SQRT(3.))/2.
      RCC=2.91
      RCH=2.00
      DO 15 N=33,401
   15 W(N)=1.0
      DO 16 NN=31,401
   16 WW(NN)=1.1
      DO 20 M=1,301
      U=FLOAT(M)
      PM(M)=U*0.1
      P=PM(M)*0.13700
      DO 30 I=1,401
      V FLOAT(I)
      R=(V-1.0)*0.05
C
C       RHS IS THE HYDROGEN 1S ORBITAL WAVE FUNCTION.
C
C       R2S IS THE CARBON 2S ORBITAL WAVE FUNCTION.
C
C       R2p IS THE CARBON 2P ORBITAL WAVE FUNCTION.
C
      RHS=EXP(-R)
      R2S=5.90950/EXP(3.94710*R)-R*(2.58290/EXP(1.47840*R)
     1+5.2230/EXP(2.84930*R)+4.56760/EXP(7.79900*R))
```

```
      R2P=R*(0.87935/EXP(1.07890*R)+3.33360/EXP(2.14440*R)+
     12.12260/EXP(5.92160*R))
      F1(I)=R*R2S*W(I)*SIN(P*R)/P
      F2(I)=R2P*W(I)*(SIN(P*R)-P*R*COS(P*R))/(P*R)
      FH(I)=R*RHS*WW(I)*SIN(P*R)/P
   30 CONTINUE
C
CC       THE INTEGRATION INTERVAL IS 0.05 A.U.
C
      CALL QUADR(F1,401,0.05,S,IER)
      X1=S
      X1=ABS(X1)
      XX1=X1*X1
      CALL QUADR(F2,401,0.05,S,IER)
      X2=S
      X2=ABS(X2)
      XX2=X2*X2
      CALL QUADR(FH,401,0.05,S,IER)
      XH=S* 1.4142/3.1416
      XH=ABS(XH)
      TNH=XH*XH*4.*3.1416*P*P
      TNC=2.*P*P*(XX1+3.*XX2)/(3.1416*4.)
      ZZ=2.*1.4142*P*XH(X1*SIN(P*RCH)-3.*X2*(COS(P*RCH)
     1-SIN(P*RCH)/(P*RCH)))/(2.*RCH)
      YY=SIN(P*RCC)/(P*RCC)+2.*COS(P*RCC)/(P*RCC)**2-
     12.*SIN(P*RCC)/(P*RCC)**3
C
C
CC       TNCH IS THE MOMENTUM DISTRIBUTION IN THE C-H BOND.
C
CC       TNCC IS THE MOMENTUM DISTRIBUTION IN THE C-C BOND.
C
      TNCH(M)=(TNC+TNH+ 2.*SCH*ZZ)/(2.*(1.+SCH**2))
      TNCC(M)=(TNC+SAB*2.*P*P*(XX1*SIN(P*RCC)/(4.*3.1416*P*RCC)
     1+3.*3.*XX2*YY/(4.*3.1416)))/(1.+SAB**2)
   20 CONTINUE
      WRITE (3,60)
   60 FORMAT (1H /3(37H    P(MRAD)        N(C-C)        N(C-H)))
      WRITE (3,70) (PM(M),TNCC(M),TNCH(M),M=1,301)
   70 FORMAT (1H /3(1H ,F9.4,2E14.5))
      END
```

```
C      SUBROUTINE QUADR
C
C      PURPOSE
C        INTEGRATES A GIVEN TABULATED FUNCTION AT A SET OF
C        SPACED POINTS.
C
C      USAGE
C        CALL QUADR(Z,N,H,S,IER)
C
C      DESCRIPTION OF PARAMETERS
C        Z    -A VECTOR OF LENGTH N CONTAINING THE VALUES OF
C              THE FUNCTION TO BE INTEGRATED
C        N    -THE NUMBER OF FUNCTION VALUES TO BE INTEGRATED
C        H    -THE RESULTANT VALUE OF THE COMPUTED INTEGRAL
C        IER  -RESULTANT ERROR CODE WHERE
C              IER=0   NO ERROR
C              IER=1   N LESS THAN 2
C              IER=2   H=0
C      METHOD
C        NUMERICAL QUADRATURE IS PERFORMED USING A 5 POINT
C        FORMULA UNTIL FEWER THAN 5 POINTS REMAIN. A 4,3,OR
C        2 POINT FORMULA IS THEN USED TO COMPLETE THE INTEGRATION.
C
C      .....................................................
      SUBROUTINE QUADR(Z,N,H,S,IER)
      DIMENSION Z(1)
      S=.0
      IF(N-1)32,32,33
   32 IER=1
      RETURN
   33 IF(H)34,35,34
   35 IER=2
      RETURN
   34 IF(N-5)40,38,38
C
C        CALCULATED USING 5 POINT FORMULA
C
   38 DO 39 I=5,N,4
   39 S=S+7.*Z(I-4)+32.*Z(I-3)+12.*Z(I-2)+32.*Z(I-1)+7.*Z(I)
      S=S*2./45.
   40 J=N-(N/4)*4+1
      GO TO (45,50,47,48),J
C
C        CALCULATE USING 4 POINT FORMULA
C
   45 S=S+.375*(Z(N-3)+3.*Z(N-2)+3.*Z(N-1)+Z(N))
      GO TO 50
C
C        CALCULATE USING 2 POINT FORMULA
C
```

```
   47 S=S+(Z(N-1)+Z(N))/2.
      GO TO 50
C
C        CALCULATE USING 3 POINT FORMULA
C
   48 S=S+(Z(N-2)+4.*Z(N-1)+Z(N))/3.
   50 S=S*H
      IER=0
      RETURN
      END
```

REFERENCES

1. C. D. Anderson, Phys. Rev. 41, 405(1932).
2. P. A. M. Dirac, Proc. Cambridge Phil. Soc.26, 361(1930).
3. H. A. Bethe, Proc. Roy. Soc. (London) A150, 129(1935).
4. A. Ore and J. L. Powell, Phys. Rev. 75, 1696(1949).
5. A. P. Mills and S. Berko, Phys. Rev. Letters 18, 420(1967).
6. C. N. Yang, Phys. Rev. 77, 242(1950)
7. S. Mohorovicic, Astron. Nachr. 253, 94(1934).
8. A. E. Ruark, Phys. Rev. 68, 278(1945).
9. M. Deutch, Phys. Rev. 82, 455(1951).
10. M. Deutch, Phys. Rev. 83, 866(1951).
11. A. Ore, University of Bergen, Arbok No.9 (1949).
12. R. E. Green and R. E. Bell, Can. J. Phys. 35, 398(1957).
13. V. B. Berestetskii and L.O. Landau, J. Exp. Theoret. Phys. (U.S.S.R.) 19, 673, 1130 (1949).
14. A. Ore, University of Bergen, Arbok No.12 (1949).
15. S. DeBenedetti and H. J. Riching, Phys. Rev.85, 377(1952).
16. R. E. Bell and R. L. Graham, Phys. Rev.90, 644(1953).
17. P. R. Wallace, "Solid State Physics" Vol.10, (Academic Press, N.Y. 1960).
18. A. T. Stewart and L. O. Roellig, "Positron Annihilation" Proceeding of the Conference Held at Wayne State Univ. on July 27-29, 1965. (Academic Press, N.Y. 1967).
19. J. M. Ziman, "Principles of the Theory of Solids" Chapter 9 (Cambridge Univ. Press, 1964).

20. J. L. Rodda and M. G. Phys. Rev. 131, 255(1963).

21. D. R. Gustufson and A. R. Mackintosh, J. Phys. Chem. Solids 25, 389(1964).

22. S. S. Hanna and R. S. Preston, Phys. Rev. 106, 1363(1957).

23. P. E. Mijnarends and L. Hambro, Phys. Letters 10, 272(1964).

24. S. Berko and J. Zuckerman, Phys. Rev. Letters 13, 339(1964).

25. C. G. Shull and Y. Yamada, J. Phys. Soc. Japan 17, Suppl. B-III, i(1962).

26. S. Berko, R. E. Kelley, and J. S. Plaskett, Phys. Rev. 106, 824(1957).

27. D. P. Kerr, Ph.D. Thesis, Univ. of Manitoba (1964).

28. R. L. deZafra, Physics Dept. Technical Report No.108, Univ. of Manyland (1958).

29. R. B. McFee, Rev. Sci. Inst. 23, 52(1952).

30. D.E. Wortman and J.G. Cramer, Nucl. Inst. and Method 26, 257(1964). Gunnan Backstron, Arkiv for Fysik 11,361(1956).

31. C. A. Coulson, Proc. Cambridge Phil. Soc. 37,55(1941).

32. C. A. Coulson and W. E. Duncanson, Proc. Cambridge Phil. Soc. 37, 67(1941).

33. C. A Coulson, Proc. Cambridge Phil. Soc. 37, 74(1941).

34. W. E. Duncanson, Proc. Cambridge Phil Soc. 37, 397(1941).

35. W. E. Duncanson and C. A. Coulson, Proc. Cambridge Phil. Soc. 37, 406(1941).

36. C. A. Coulson, Proc. Cambridge Phil. Soc. 38, 100(1942).

37. W. E. Duncanson, Proc. Cambridge Phil. Soc. 39, 180(1943).

38. D. P. Kerr, S. Y. Chuang, and B. G. Hogg, Mol. Phys. 10, 13(1965).

39. P. O. Lowdin, Phys. Rev. 90, 120(1953).

40. G. E. Lee-Whiting, Phys. Rev. 97, 1557(1955).

41. J. P. Carbotte and H. L. Arora, Can. J. Phys. 45, 387(1967).

42. L. Madansky and F. Rasetti, Phys. Rev. 79, 397(1950).

43. S. Berko and J. S. Plaskett, Phys. Rev. 112, 1877(1958).

44. R. A. Ferrell, Rev. Mod. Phys. 28, 308(1956).

45. A. T. Stewart, Can. J. Phys. 35, 168(1957).

46. C. Zener, Phys. Rev. 82, 403(1951).

47. A. T. Stewart and N. K. Pope, Phys. Rev. 120, 2033(1960).

48. K. Gubernator and A. Flammersfeld, Z. Physik. 156, 179(1959).

49. P. S. Takhar, Phys. Letters 23, 219(1966).

50. S. M. Kim, A. T. Stewart, and J. P. Carbotte, Phys. Rev. Letters 18, 385(1967).

51. A. T. Stewart and J. B. Shand, Phys. Rev. Letters 16, 261(1966).

52. F. Herman and S. Skillman, "Atomic Strcture Calculation" (Prentice-Hall, Inc. Englewood Cliffs, New Jersey, 1963).

53. D. R. Hartree, "Numerical Analysis" (Clarendon Press, Oxford, 1958), Chapter 7, Section 2.